

University of New Mexico

UNM Digital Repository

Civil Engineering ETDs

Engineering ETDs

Summer 7-27-2021

Effect of Degradation Environment and Relative Humidity on Fracture of Cement

Patience L. Raby

University of New Mexico

Follow this and additional works at: https://digitalrepository.unm.edu/ce_etds



Part of the [Civil and Environmental Engineering Commons](#)

Recommended Citation

Raby, Patience L.. "Effect of Degradation Environment and Relative Humidity on Fracture of Cement." (2021). https://digitalrepository.unm.edu/ce_etds/288

This Thesis is brought to you for free and open access by the Engineering ETDs at UNM Digital Repository. It has been accepted for inclusion in Civil Engineering ETDs by an authorized administrator of UNM Digital Repository. For more information, please contact disc@unm.edu.

Patience Raby

Candidate

Civil Engineering

Department

This thesis is approved, and it is acceptable in quality and form for publication:

Approved by the Thesis Committee:

Dr. Mahmoud Reda Taha, Chairperson

Dr. John Stormont

Dr. Jessica Rimsza

**EFFECT OF DEGRADATION ENVIRONMENT AND
RELATIVE HUMIDITY ON FRACTURE OF CEMENT**

by

PATIENCE RABY

**B.S., CIVIL ENGINEERING, UNIVERSITY OF NEW
MEXICO, 2020**

THESIS

Submitted in Partial Fulfillment of the
Requirements for the Degree of

**Master of Science
Civil Engineering**

The University of New Mexico
Albuquerque, New Mexico

December, 2021

ACKNOWLEDGEMENTS

I thank my advisor, Dr. Mahmoud Taha, for guiding me through these studies and providing me with this opportunity to challenge myself and further my education. I would also like to thank Dr. Jessica Rimsza of Sandia National Laboratory for her support and encouragement as I have progressed. A special thanks to Sandia National Laboratory for funding this research. I would like to thank Dr. John Stormont for serving as part of my committee and supporting my studies. I also thank the Department of Civil, Construction and Environmental Engineering.

A special thank you to the close colleagues who have aided me in countless ways – whether a second opinion, an extra hand, or encouragement. I am especially grateful for Dominic Dunlap for always being in my corner and his consistent support over the years. I also thank my family for their confidence in me.

EFFECT OF DEGRADATION ENVIRONMENT AND RELATIVE HUMIDITY ON FRACTURE OF CEMENT

by

PATIENCE RABY

B.S., CIVIL ENGINEERING, UNIVERSITY OF NEW MEXICO, 2020

M.S., CIVIL ENGINEERING, UNIVERSITY OF NEW MEXICO, 2021

ABSTRACT

Concrete serves in all forms of humidity conditions (arid climates to submerged conditions) and can be exposed to many different forms of degradation. To better understand the effects that degradation and humidity have on concrete as a composite, the effects on cement alone must first be better understood. This research aims to examine the significance of degradation (calcium leaching or sulfate attack), in addition to relative humidity, on cracking and fracture behavior of cement. Flexure and fracture tests were performed on cement exposed to varying periods of each form of degradation as well as various humidities. Samples were exposed to degradation for varying periods of time (1-week, 12-weeks and 24-weeks) before being exposed to humidity and tested. Testing was performed after overnight exposure to relative humidities of 16%RH, 50%RH, and 99%RH. The experimental observations shed light on the significance of the interaction of degradation and humidity on cracking and fracture behavior of cement.

TABLE OF CONTENTS

ABSTRACT.....	iv
TABLE OF CONTENTS.....	v
LIST OF FIGURES.....	vii
LIST OF TABLES.....	x
1. INTRODUCTION.....	1
1.1. Background and Motivation.....	1
1.2. Scope of Work.....	1
1.3. Outline of Work.....	2
2. LITERATURE REVIEW.....	4
2.1. Cement Degradation Review.....	4
2.1.1. Degradation modes.....	6
2.1.2. Cement damage quantification methods.....	13
2.1.2.1. Damage theory.....	13
2.1.2.2. Macroscopic methods.....	16
2.1.2.3. Microscopic methods.....	17
2.1.3. Cement degradation discussion.....	24
2.2. Fracture Mechanics.....	26
2.2.1. Quasi-brittle fracture mechanics (QBFM) analysis: Elastic crack modulus method.....	27
3. MATERIALS AND METHODS.....	30
3.1. Sample Preparation.....	31
3.2. Degradation.....	34

3.3. Humidity Exposure.....	36
3.4. Fracture Toughness Test.....	38
3.4.1. Test setup.....	39
3.4.2. Loading procedure.....	40
3.5. Leached Depth Quantification.....	43
3.6. Analysis.....	43
3.6.1. Fracture model.....	44
3.6.2. Damage quantification.....	48
4. RESULTS AND DISCUSSION.....	49
4.1. Fracture Toughness Tests.....	49
4.2. Leached Depth.....	67
4.3. Damage.....	76
5. CONCLUSION.....	78
6. REFERENCES.....	81
7. APPENDICES.....	87
Appendix A – Matlab Code.....	87
Appendix B – Mathcad Code.....	99
Appendix C – Cement Degradation Reference Information.....	101

LIST OF FIGURES

Figure 1. Breakdown of materials used in making cement degradation specimens by studies reviewed	5
Figure 2. Schematic representation of the four primary forms of cement degradation.....	6
Figure 3. Schematic illustration showing damage on micro and macro scales.....	15
Figure 4. Schematic representation of four identifiable degradation zones in a cement paste specimen exposed to carbonation	20
Figure 5. Schematic representation of the level of min. and max. levels of cement damage as reported in literature review	26
Figure 6. Closed-loop approach for QBFM effective crack modulus.....	29
Figure 7. Testing dimensions for fracture and flexure tests.....	31
Figure 8. Diagram of steps to attain notch in fracture samples.....	32
Figure 9. Schematic of the covering on degradation samples.....	32
Figure 10. Degradation bath setup.....	35
Figure 11. 50%RH chamber setup.....	36
Figure 12. Results from preliminary relative humidity exposure test.....	37
Figure 13. Schematic of the testing setup used to calculate the counterweight positioning	38
Figure 14. Sample ready for testing, showing test equipment.....	40
Figure 15. Median load-displacement curves for the 1-week, neat flexure tests.....	50
Figure 16. Median load-displacement curves for the 12-week, neat flexure tests.....	51

Figure 17. Median load-displacement curves for the 12-week, sulfate attack flexure tests.....	51
Figure 18. Median load-displacement curves for the 12-week, calcium leached flexure tests.....	52
Figure 19. Median load-displacement curves for the 24-week, neat flexure tests.....	52
Figure 20. Median load-displacement curves for the 24-week, sulfate attack flexure tests.....	53
Figure 21. Median load-CMOD curves for the 1-week, neat fracture tests.....	54
Figure 22. Median load-CMOD curves for the 12-week, neat fracture tests.....	54
Figure 23. Median load-CMOD curves for the 12-week, sulfate attack fracture tests.....	55
Figure 24. Median load-CMOD curves for the 12-week, calcium leached fracture tests.....	55
Figure 25. Median load-CMOD curves for the 24-week, neat fracture tests.....	56
Figure 26. Median load-CMOD curves for the 24-week, sulfate attack fracture tests.....	56
Figure 27. Summary data for E for 12-week exposure.....	57
Figure 28. Summary data for MoR for 12-week exposure.....	58
Figure 29. Summary data for G_F for 12-week exposure.....	58
Figure 30. Summary data for E for 24-week exposure.....	59
Figure 31. Summary data for MoR for 24-week exposure.....	59
Figure 32. Summary data for G_F for 24-week exposure.....	60
Figure 33. Summary data for E for neat tests at different exposure times.....	60

Figure 34. Summary data for MoR for neat tests at different exposure times.....	61
Figure 35. Summary data for G_F for neat tests at different exposure times.....	61
Figure 36. Summary data for E for sulfate attack at different exposure times.....	62
Figure 37. Summary data for MoR for sulfate attack at different exposure times.....	62
Figure 38. Summary data for G_F for sulfate attack at different exposure times.....	63
Figure 39. Images of fluorescence tests.....	68
Figure 40. Typical TGA results at edge for 12-week neat sample.....	70
Figure 41. Typical TGA results at mid-depth for 12-week neat sample.....	70
Figure 42. Typical TGA results at center for 12-week neat sample.....	71
Figure 43. Typical TGA results at edge for 12-week sulfate attack sample.....	72
Figure 44. Typical TGA results at mid-depth for 12-week sulfate attack sample.....	72
Figure 45. Typical TGA results at center for 12-week sulfate attack sample.....	73
Figure 46. Typical TGA results at edge for 12-week calcium leached sample.....	74
Figure 47. Typical TGA results at mid-depth for 12-week calcium leached sample.....	75
Figure 48. Typical TGA results at center for 12-week calcium leached sample.....	75
Figure 49. Observed density changes as the samples degrade.....	76
Figure 50. Image of calcium leached sample after 20-weeks exposure.....	77

LIST OF TABLES

Table 1. Damage metrics applied to references.....	16
Table 2. Comparison of cement degradation quantification methods.....	24
Table 3. Scenario sets for experimental program.....	34
Table 4. Load limits that loading rate changed for fracture tests.....	42
Table 5. Load limits that loading rate changed for flexure tests.....	42
Table 6. Summary data for 1-week, neat fracture properties.....	63
Table 7. Summary data for 12-week fracture properties.....	64
Table 8. Summary data for 24-week fracture properties.....	64
Table 9. P-values for E, comparing across RH exposures.....	65
Table 10. P-values for MoR, comparing across RH exposures.....	65
Table 11. P-values for G_F , comparing across RH exposures.....	65
Table 12. P-values for E, comparing across neat exposure times.....	66
Table 13. P-values for MoR, comparing across neat exposure times.....	66
Table 14. P-values for G_F , comparing across neat exposure times.....	66
Table 15. P-values for E, comparing across sulfate attack exposure times.....	66
Table 16. P-values for MoR, comparing across sulfate attack exposure times.....	67
Table 17. P-values for G_F , comparing across sulfate attack exposure times.....	67
Table 18. Average values for E at 99%RH exposure.....	77
Table 19. Damage metrics determined for tests performed.....	77

1. INTRODUCTION

1.1. Background and Motivation

Current research on concrete durability, longevity, sustainability, and resilience necessitates an understanding of the effect that external factors have on the long-term degradation of concrete. As cement is the main binder in concrete, understanding cement's isolated behavior is critical to better understanding concrete behavior as a composite. Concretes and cements serve in all kinds of climates and humidity conditions; therefore, it is also important to understand how exposure to different relative humidity levels may impact a degraded cement matrix. This will provide a pathway to improve modelling of both cement paste and concrete.

Degradation that is isolated to cement paste alone is still not fully understood. The topic has many influencing factors, which is an inherent reason for the level of complexity associated with cement degradation. Studies that have been performed often use an array of different approaches and methods for the type of cement, degradation processes, and modelling or quantification. This makes it challenging to paint one, clear picture. In addition, fracture of cement paste is not often an area that is given attention in previous work that pertains to cement degradation.

1.2. Scope of Work

This work aims to quantify damage in a cement matrix due to degradation and to give better understanding on the interaction between a degraded cement matrix and exposure to different humidities. We also aim to understand how the combined effect of environmental exposure and relative humidity changes affect strength and fracture behavior of cement paste. Cement paste samples were degraded by calcium leaching and sulfate attack,

exposed to several relative humidities, and tested in flexure and fracture to observe changes. Samples were exposed to degradation for either 1-, 12-, or 24-weeks. Leached depth was also observed through visual observation using fluorescence as well as through microstructural changes at various depths through Thermogravimetric Analysis (TGA). Fracture characteristics were analyzed using a quasi-brittle fracture mechanics (QBFM) analysis to quantify changes in fracture characteristics of cement paste. The results from both the leached depth analysis and fracture tests were utilized to assess damage due to both degradation modes. Relating change in mechanical and fracture properties to degradation is a key part of better understanding the implications of degradation on cement paste.

The work in this thesis represents part of an ongoing research program being performed at the University of New Mexico (UNM) in collaboration with Sandia National Laboratories (SNL). The work has aimed to provide critical experimental observation for modelling of cement and concrete degradation and how this degradation impacts damage (change in properties) on the matrix.

1.3. Outline of Work

There are seven chapters that make up this thesis: Introduction, Literature Review, Materials and Methods, Results and Discussion, Conclusion, References, and Appendices.

Chapter 2, Literature Review, discusses previous studies and the state of current knowledge regarding cement degradation, damage theory, and fracture mechanics. Each of these areas give important context to this thesis.

Chapter 3, Materials and Methods, covers the materials used in these studies, the methods used for the various tests performed, and how data analysis was performed.

Chapter 4, Results and Discussion, presents the results found for fracture properties and leached depth. These are then used to quantify damage and discussed. Again, only the results for experiments performed at the time of this thesis being written are presented and discussed.

Chapter 5, Conclusion, contains the conclusions that were able to be drawn from the experiments performed at this point in the project. Future work is also presented.

2. LITERATURE REVIEW

2.1. Cement Degradation Review

To better understand cement degradation methods and which degradation modes impact the most damage, a review of cement degradation literature was performed and is discussed in this section. This was used to help determine which degradation modes and associated methods would be implemented in the experimental program. The review is focused on the chemical degradation of cement, not the degradation of concrete as a composite with aggregate and/or reinforcement. This excludes common concrete degradation concerns such as an alkali-silica reaction and chloride-ion attack. We limit our discussion of the degradation of concrete or cement mortars to the extent that it relates to the chemical degradation of cement paste. Cement paste is defined as a mix of cement and water. Cement mortar is a mix of cement, water, and fine aggregate. Concrete is a mix of cement, water, and aggregate; admixtures and cement alternatives may be included. This review is focused on hardened cement paste with no discussion on powder cement. Throughout this paper, hardened cement paste is referred to as cement. Figure 1 shows a breakdown of the types of materials examined in the references covered herein.

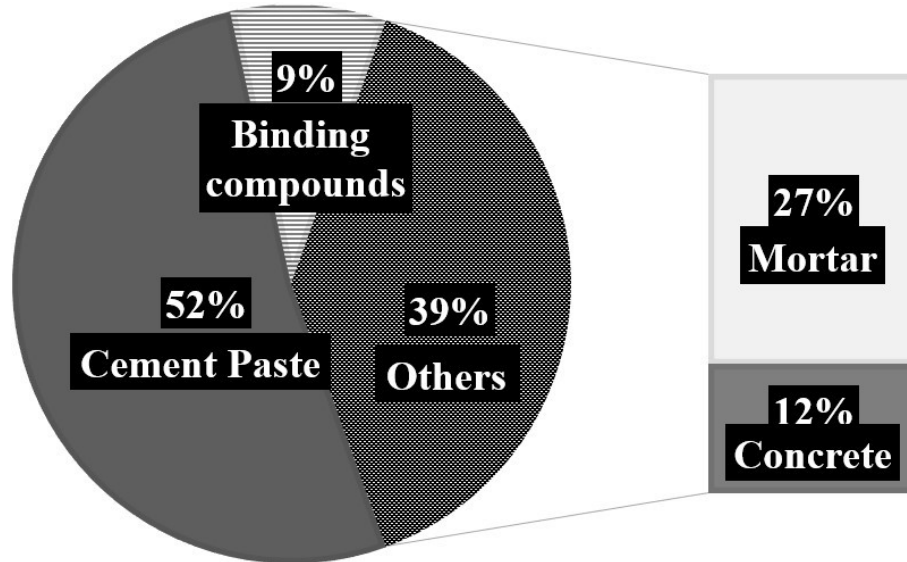


Figure 1. Breakdown of materials used in making cement degradation specimens by 35 studies reviewed in this section.

Cement degrades due to chemical reactions that cause the original, strong matrix composition either to become more porous (through the dissolution of binding compounds) or to crack on the microscale (through the formation of expansive compounds). In all the diverse settings that concrete and cement composites are implemented, many forms of degradation can occur. The primary forms of cement degradation include, but are not limited to: calcium leaching, sulfate attack, carbonation, and chloride penetration. Degradation of Portland cement (the most common type of cement used) occurs primarily through three distinct paths: exchange reactions between an aggressive fluid and cementitious compounds, dissolution and leaching of cementitious compounds, or reactions of cement with other materials that form expansive products [1,2].

For the purposes of cement degradation and this study, damage is best described and understood as the observed impact of the degradation mechanisms. Damage can be defined as the change that takes place in the material at a level below the scale of observation and results in a material's loss of stiffness, strength, or both. It has been widely accepted that

damage can only be inferred from observing a material's behavior but cannot be directly measured [3]. It can also be said then that damage is an inferred quantification of degradation.

A schematic representation of the four primary forms of cement and concrete degradation is presented in Figure 2. Water is often a common medium for the transport of ions in these degradation scenarios [1]. In most instances, cement degradation occurs alongside other forms of concrete degradation. In this section, we discuss the different cement degradation scenarios and the laboratory methods used to replicate cement degradation.



Figure 2. Schematic representation of the four primary forms of cement degradation as discussed in this section.

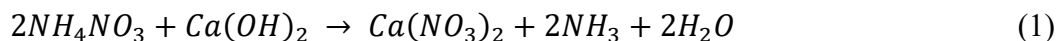
2.1.1. Degradation Modes

Calcium leaching

Calcium leaching, called decalcification, occurs when fluid travels through the porous cementitious matrix, reacts with hydration products – specifically calcium

hydroxide (CH) and calcium silicate hydrate (CSH) – and leaches out calcium-rich compounds over time, thus affecting the major binding compounds in the cement matrix [4]. Calcium leaching can occur in many modes – by virtually any exposure to water. For example, calcium leaching could occur in a runoff channel, or perhaps in sidewalks exposed to rain over time. Studies have shown that calcium leaching of cement paste is essentially a dissolution-driven occurrence; whereas the cementitious matrix and an external solution have a differential in ionic concentration, causing ions within the matrix to migrate out [5]. CH is not as stable a compound as CSH, making it more likely to be leached out [6].

Initially, distilled or deionized water was used to replicate calcium leaching and decalcify concrete specimens in the lab [7,8]. The disadvantage to using water is that the kinetics of the calcium leaching process is slow, requiring days to years' worth of reaction time to decalcify cement [4]. To circumvent the relatively long reaction times necessary for recreating calcium leaching in a lab setting, accelerated calcium leaching processes have been investigated. A common method is to implement an ammonium nitrate solution instead of water; this accelerated method was proven to yield consistent results and to successfully leach out the same binding compounds as water does [9]. Another, less common method to accelerate decalcification is to apply an electrical potential gradient through a specimen while immersed in ion-exchanged water [10]. The general reaction equation between ammonium nitrate and CH is shown in Eq. (1); ammonium nitrate reacts with CH to form calcium nitrate, ammonia, and water [11].



Application of ammonium nitrate as a leaching solution started with a study performed by Lea in 1965 [9] on the effect of ammonium salts in concrete, which found that ammonium salts could degrade concrete in a similar fashion as water but at a much quicker rate. It was not until the 1990's that Carde and François [12] began to implement similar methods to leach cement pastes to model the degradation of cement paste, which has led to additional studies using similar approaches. Le Bellégo et al. [11], examined the effect of leaching on the flexural behavior of cement. A loss of stiffness, a decrease in maximal load, and decreased fracture energy were reported when calcium leaching increased. Other studies also identified that as the water-to-cement ratio of the cement paste increased, the effects of calcium leaching (i.e., strength loss, leaching depth) increased. This was attributed to the increase in cement porosity observed in specimens with high water-to-cement ratios; high porosity enables calcium leaching to occur at a greater depth compared with specimens with low water-to-cement ratios [5,13]. The relationship between porosity and leaching is discussed in Section 2.1.2.

Sulfate Attack

Sulfate attack was identified as a significant source of cement and concrete degradation in the mid-1900s but was not well studied until later in the 20th century [14,15]. Sulfate attack occurs most often in foundations or underground concrete systems due to exposure to soils with high sulfate contents. It can also be observed in concrete-lined sewage systems and in concrete exposed to water carrying sulfates. It is generally accepted that sulfate attack is primarily caused by ettringite formation from monosulfate, but the precise mechanism of this expansion is debatable and is beyond the scope of this study [1]. Ettringite forms due to the reaction of the sulfate ions in the gypsum added during cement

manufacturing with tricalcium aluminate (C3A) which is a main component of the clinker [1]. Ettringite begins as long and slender needles that form at an early age of hydration and slowly turn plate-like as it reacts with sulfates [1]. Sulfate attack has two forms that often occur simultaneously – external and internal sulfate attack.

External sulfate attack occurs when external sulfate ions (existing in seawater, groundwater, sewage water, etc.) penetrate concrete and encounter unhydrated C3A in the cement matrix, leading to the expansive formation of ettringite and thus cracking [16]. Internal sulfate attack, also known as delayed ettringite formation (DEF), occurs due to unreacted internal sulfate ions. When the initial cement hydration is interrupted by either high curing temperature or insufficient humidity, ettringite formation is suppressed. This process can leave a high number of unreacted sulfates inside the concrete pores. The surplus of sulfates can react with calcium and aluminum later in the process and form expansive ettringite.

Both external and internal sulfate attack cause expansion and high internal stresses that the cement matrix cannot handle, and thus microcracks form [1,17]. Fu et al. [18] suggested that three factors govern sulfate attack: Portland cement composition, curing temperature, and environment moisture. If the cement composition has a high content of C3A, there is an increased chance of either form of sulfate attack. High curing temperatures and moist environments have also been shown to increase the risk of internal sulfate attack [16,18]. Zhang et al. [19] found that both a high concentration of sulfate ions from external sources as well as a high water-to-cement ratio led to severe damage from expansion in CSH specimens. Ma et al. [20] observed pore size changes, sulfate content, and cracks in cement pastes exposed to sodium sulfate solution (30 g/L) up to 189 days of exposure. It was

observed that after 70 days of exposure to the solution, pore diameter was less than initial values and leveled out as the matrix reached a point where pores filled and the matrix could only expand. This phenomenon of sulfate attack creating pores filled with materials leads to an interesting behavior. Liu et al. and others note that, up to ~90 days of exposure, samples actually gain strength, then lose strength as microscale pressure due to expansion exceeds the tensile strength and begins to cause microcracks [21,22]. Even with this, it can take considerable time (up to 270 days) before notable strength loss can be observed with a sodium sulfate concentration of 0.350 mol.

Sulfate attack is most often replicated by exposing specimens to a sulfate solution for various amounts of time. For the sulfate solution, most studies used sodium sulfate [17,23,24], while a few used magnesium sulfate [14,25]. Wang [17] used sodium sulfate with a concentration of 0.350 mol on cement paste specimens to observe the leaching behavior and determined that ettringite formation accounted for most of the observed damage. Another study using sodium sulfate – at concentrations of 0.011 mol and 0.211 mol – found that stress in restrained cement paste specimens was much higher when exposed to higher concentrations than lower concentrations [23]. This is explained by the expansive nature of sulfate attack. Liu et al. [25] considered the effect of relative humidity and temperature on the degradation of cement mortar exposed to sulfate attack; it was found that sodium sulfate deteriorated cement more than magnesium sulfate. Deterioration was observed through mass change, relative dynamic modulus of elasticity, and water-soluble sulfate content. Also, low relative humidity led to high levels of degradation compared with high relative humidity. It was suggested that this is due to physical forms of attack (i.e., salt crystallization and surface scaling) being more likely to occur in a dry

environment [25]. Planel et al. [24] looked for similarities between sulfate attack and calcium leaching mechanisms and determined that dissolution occurred in a similar fashion in both a sodium sulfate and deionized water environment, but significantly more binding compounds precipitated out from the sulfate attack specimens.

Carbonation

Carbonation, or CO₂ attack, is a form of cement degradation that occurs when CO₂ in the atmosphere penetrates the cementitious matrix and reacts with water and CH. Carbonation can occur slowly over a long period of time as concrete is exposed to air with high CO₂ content. It can also occur when the cement matrix is exposed to CO₂ dissolved in water or in a supercritical state (e.g., CO₂ sequestration wells) [26–28]. While it is acknowledged that other hydration products also react with CO₂, it is widely accepted that CH reacts the most noticeably [29,30]. This reaction transforms CH into calcium carbonate that can leach out of the concrete compromising the strength and stiffness of the matrix by introducing cracks and negatively impacting porosity, pH, and micro-mechanical properties [27–29,31]. If the pH of the matrix drops significantly, the binding compounds of the cement can destabilize and lose considerable strength and stiffness [1]. While most effects observed due to carbonation are undesired, there have been studies looking into the utilization of carbonization in applications such as curing, concrete recycling, or waste immobilization [29,32,33].

Methods to recreate the degradation of cement due to carbonation in a lab setting include natural and accelerated processes. The natural approach includes exposing concrete specimens to ambient air for an extended period of time; Garcia-Gonzalez et al. [32] exposed concrete specimens to CO₂-incorporated air for 200 days. Accelerated processes

traditionally include exposing specimens to air or aqueous solutions with relatively high concentrations or supercritical CO₂ [27,28,30,31,33]. Urbonas et al. [33] exposed cement pastes and mortars with varying alkalinities to supercritical CO₂ and found that higher alkalinity of cement led to slower carbonation and that the carbonation treatment could allow the cement paste specimens to gain compressive strength.

Chloride penetration

An area of widespread concern in cement degradation is damage from exposure to deicing salts due to chloride penetration. Chloride ions can displace hydroxide, sulfate, and carbonate groups in ettringite and/or AFm phases in hydrated cement paste [34]. The AFm phase in Portland cements refers to a family of hydrated calcium aluminates based on the hydrocalumite-like structure of $4\text{CaO}\cdot\text{Al}_2\text{O}_3\cdot 13\text{--}19\text{ H}_2\text{O}$ [35]. If water containing chlorides penetrates the cement matrix, salts can crystallize inside the cement pores, thus creating high internal stresses that can lead to spalling [34,36–38]. Research examining the effects of chlorides and deicing salts on cement paste alone is limited. Methods to replicate the chloride and deicing salt exposure to cement include submerging specimens in a chloride solution for varying time periods. This is often coupled with either wet-dry cycles or freeze-thaw cycles.

Balonis et al. [34] explored phase relations between AFm and chloride; it was determined that chloride ions can displace sulfate in monosulfoaluminate, which indirectly causes sulfate attack. Zhang et al. [39] combined flexural loading and wet-dry cycles of seawater in an environmental chamber and found that such a combination accelerates the deterioration of cement paste's microstructure. Farnam et al. [40] exposed cured cement paste specimens to a calcium chloride solution for three days before performing freeze-

thaw tests; a phase diagram relating calcium chloride and CH to temperature was developed. Wang et al. [41] reported that the scaling of cement paste decreased when a sodium chloride-based deicing agent was used (compared with a calcium chloride-based deicing agent) under both wet-dry and freeze-thaw cycles. Another study by Farnam et al. [42] found that magnesium chloride deicers had a significant degradation effect due to the production of magnesium silicate hydrate (MSH) and brucite ($\text{Mg}(\text{OH})_2$). The formation of MSH was found to damage cement as it reduced the elastic modulus of concrete.

2.1.2. Cement damage quantification methods

The methods for quantifying cement damage due to degradation have changed over the last three decades. Early methods to observe this change consisted of observing macroscopic changes (visual observations, mass loss measurement, direct strength tests, etc.). In an effort to better understand the macroscopic changes, researchers began exploring microscopic changes. Microstructural changes can be observed and compared through advanced techniques like scanning electron microscope (SEM), X-ray diffraction (XRD), energy-dispersive X-ray spectroscopy (EDS), Fourier-transform infrared spectroscopy (FTIR), and thermal gravimetric analysis (TGA). The microscale methods give context and help explain the macroscopic observations.

2.1.2.1. Damage theory

Quantification of cement degradation is a critical step to both evaluate the methods used to simulate degradation as well as to develop computational models for degradation under varying service environments. Research on integrated modeling approaches where chemical, physical, and mechanical simulations are integrated have been reported in literature and will play a significant role in the future of concrete infrastructure modeling

[4,5,7,14,43]. For instance, in some non-local models a damage parameter is explicitly included in the formulation [44,45]. Damage quantification describes the level of damage and relates it to microscopic or macroscopic cement features, including visual and mechanical features. Recall the definition of damage: the change that takes place in the material at a level below the scale of observation and results in a material losing stiffness, strength, or both. For example, if the initial cement elastic modulus "E₀" is observed at the macroscale, the change in elastic modulus due to changing environment at the ith instant can be used to describe the damage at the ith instant - "D_i" - as described in Eq. (2). This definition was proposed by Krajcinovic (1984) and adopted by subsequent damage mechanics studies [3,46].

$$D_i = 1 - \frac{E_i}{E_0} \quad (2)$$

Where E_i is the new elastic modulus at the ith instant. It is critical to note that the damage quantified here at the macroscale accounts for changes that happen at the subscale (e.g., microscale), which cannot be observed at the scale damage is quantified. Specifically, the macroscale change observed in cement behavior (e.g., elastic modulus) is attributed to damage taking place at the microscale. The same concept can extend to measure the elastic modulus or strength at the microscale (e.g., using nano- or micro-indentation) and thus quantifying damage due to changes happening in the material at the nanoscale. A schematic representation of damage in concrete due to microcracking and its quantification using macroscale observations of stress-strain curve is illustrated in Figure 3. It can be realized that a distinction of the scale at which damage is quantified is paramount. Furthermore,

connecting the quantification across the scales is critical for future computational approaches.

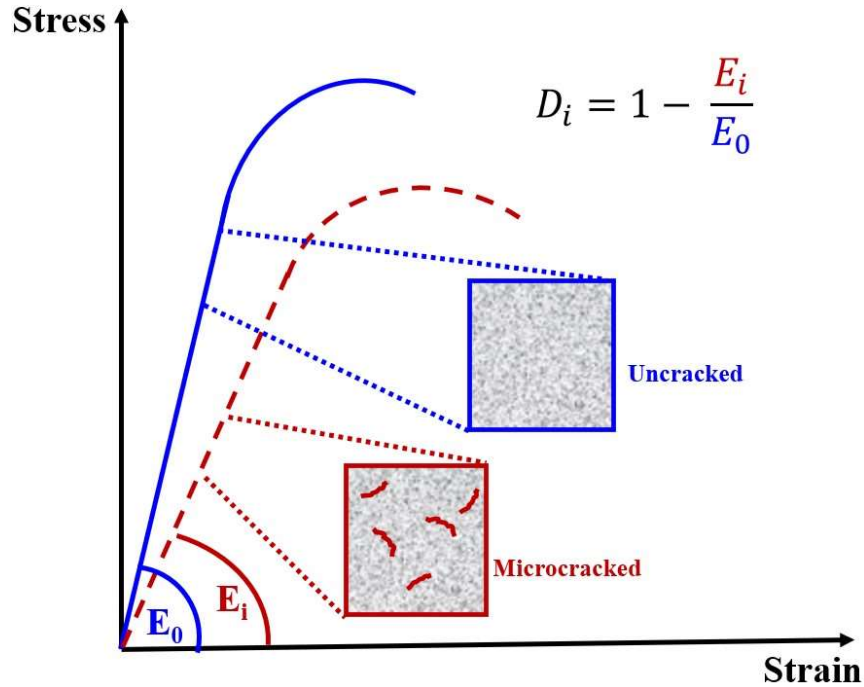


Figure 3. Schematic illustration showing damage on microscale (cracking) in cement and its quantification using macroscale observations of the stress-strain behavior. The elastic modulus is measured as the slope of the stress-strain curve.

To better compare the references considered in this review, metrics were defined for several quantification methods that were commonly used across the references including $D_{E,i}$, $D_{\sigma,i}$, $D_{P,i}$, $D_{l,i}$. Eq. (2) was used for papers that measured change in stiffness due to degradation, for consistency, $D_{E,i}$. A similar equation was applied to papers that observed change in compressive strength; E_i and E_0 were replaced with the degraded strength and the neat strength, respectively. The compressive strength metric is denoted by $D_{\sigma,i}$. Eq. (3) was applied to papers that reported an increase in porosity due to degradation and $D_{P,i}$ is used to define this damage metric. This equation was defined by using reported porosity (%) to determine the percentage of solids, then using the change in solids as the damage.

P_i represents the porosity of the specimen at the i^{th} instant and P_0 represents the undegraded porosity. Eq. (4) was applied to reports of leached depth with the damage as the percentage of the width or diameter lost to leaching. $D_{l,i}$ is used to denote this damage metric with l_i as the leached depth at the i^{th} instant and l_0 as the dimension being affected (typically width or diameter). Eq. (3) assumes the dimension affected by leaching is not affected by degradation in any other dimension. All values for damage metrics were reported as a percentage. Table 1 shows which damage metrics were applied to the various sources considered in this review. These metrics were compared directly and the maximums and minimums for each degradation mode are summarized later in the discussion.

$$D_{P,i} = \frac{P_i - P_0}{1 - P_0} \quad (3)$$

$$D_{l,i} = \frac{2 * l_i}{l_0} \quad (4)$$

Table 1. Damage metrics applied to references.

Damage Metric	Reference
Change in E ($D_{E,i}$)	[11,27,29,38,47–50]
Change in compressive strength ($D_{\sigma,i}$)	[9,10,29,41,51–53]
Change in porosity ($D_{P,i}$)	[29,52–54]
Leached depth ($D_{l,i}$)	[10,11,24,27,28,33,40,42,43,52,55,56]

2.1.2.2. Macroscopic methods

As mentioned, an early method for quantifying damage in cement was to realize its physical changes by comparing the weight and dimensions before and after exposure to degradation environments [7,8]. Another method that often accompanied these measurements was mechanical testing to observe the change in strength and stiffness between control and degraded specimens. Ouyang [57] was able to expand on Eq. (2) and

similar work to model compressive properties of cement mortar exposed to sulfate attack. These methods revolving around mechanical testing are still implemented in recent studies but typically supplemented by microscopic observations. For example, Liu et al. [49] and Ponloa and Sajjavanich [48] considered the strength change in specimens using nanoindentation while also looking at porosity and other microscale properties. This approach gives a holistic view of what has occurred in the cement specimen exposed to degradation mechanisms and helps to relate damage observed at the macroscale to the changes taking place at the micro- or nano- scales due to degradation.

2.1.2.3. Microscopic methods

Several methods are currently used to capture changes at the microscopic level and quantify degradation (damage) in cement. The following methods discussed herein are the most commonly reported in literature.

Porosity

Porosity has proven to be a useful analog to quantify cement degradation. A cement matrix with high porosity tends to be weaker than neat specimens; this has been linked to the removal of major binding compounds during leaching [10,11,49,51]. An early method to estimate a porosity was to weigh a saturated specimen, dry it at warm temperatures (ranging from 80°C-105°C) and take regular weight readings until the weight stabilized. This method assumes that the weight loss represents water loss in available pore space [51,53,56]. Such assumption has proven to be controversial since studies have shown that bound water in the matrix can be lost at high temperatures, meaning results can overestimate the true porosity [49,53,58]. More precise characterization methods such as scanning electron microscopy (SEM) with backscattered electron imaging can be used to

observe changes in the cement microstructure, including microcracking and porosity. Kutchko et al. [27] implemented this methodology by analyzing nanoscale SEM images of carbonation degraded samples..

Mercury intrusion porosimetry (MIP) is a widely used method to determine porosity and pore size distribution [20,39,47,50,52,59]. Pressure is applied to force mercury into pore spaces, then the pressure is relieved. Using the Washburn equation, the pressure applied can be related to the pore size distribution and cement pore volume [60]. Choi and Yang [52] utilized the MIP approach to show a significant increase in pore volume after calcium leaching. Researchers must be careful when using the MIP method. It has been suggested that if it is not possible to condition cement specimens by outgassing or freeze-drying, a vacuum and high temperature (150°C) might be used to eliminate foreign fluids [61]. As previously mentioned, it is important not to overestimate porosity by unintentionally removing bound water. Furthermore, the pressures used in the MIP method can also change the pore structure based on the level of cement compressibility, which is a function of the cement matrix composition. Such potential impacts of the testing method on the measurement of porosity led to numerous critiques and shed doubt on the precision of the cement porosity measured using the MIP method [61,62].

Diffusivity

Diffusivity is defined as the diffusion rate of ions through water-filled pores and has been used as a parameter to measure degradation in the literature [1]. As degradation is often driven by diffusion of leachants, diffusivity is an important property to measure for modelling purposes [11]. In 1990, Garboczi [62] discussed the inherent challenges of measuring and predicting diffusivity in cementitious materials. It was noted that the

complex and highly variant nature of the pore network in cementitious materials makes it challenging to accurately measure fluid transport, thus complicating the estimation of diffusivity. Recent studies explored correlating diffusivity and electrical conductivity, which showed encouraging results [63,64]. Otherwise, researchers have used standards to estimate concrete resistance to chloride ion penetration and have also used this measure to quantify degradation [65]. A higher chloride diffusion coefficient has been directly correlated to a higher level of concrete degradation [47,66].

Leached depth

Observing the leached depth (furthest depth from the contact surface that leaching has occurred) in a cement specimen with definable degradation zones has allowed researchers to model degradation processes [11,28,51,57,67–69]. Generally, across the degradation modes, there is a degraded zone at the exposed surface of the specimen, a degradation front (composed of both a reaction front and a dissolution front), and an unleached core of the specimen [27,28,55,56]. Figure 4, adopted from SEM micrograph observed by Kutchko et al. [27], shows four degradation zones identified in a carbonated specimen. Segura et al. [43] and others have observed a noticeably linear relationship between leached depth and exposure time [10,43,70]. The leached depth has been useful when simulating leaching or degradation processes since it can be directly related to time. SEM micrographs and other tests (TGA, FTIR, etc.) can be used to identify the degradation processes' reactants and support the identification of leached zones. Adenot and Buil [67] used SEM to identify Portlandite in degraded zones of the cement paste.

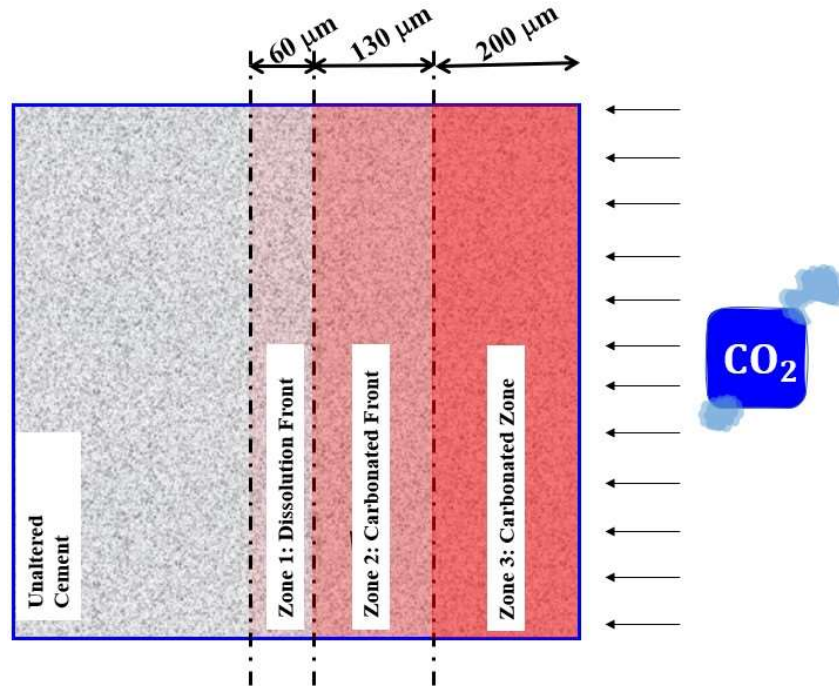


Figure 4. Schematic representation of four identifiable degradation zones in a cement paste specimen exposed to carbonation. The figure shows the unaltered cement core, Zone 1: Dissolution front, Zone 2: Carbonated front, and Zone 3: Carbonated Zone. The dimensions of the degradation zones are based on observations reported in the literature [27].

Fluorescence is a tool that allows visual and manual measurement of leached depth. Solutions that change color when exposed to varying pH levels, such as phenolphthalein, can be used to observe pH changes in cement specimens. Since degraded cements tend to have a lower pH than that of non-degraded cement, fluorescence has been recognized as a useful tool to identify cement degradation [11,31,48,52,56,69]. When exposed to phenolphthalein, for example, a degraded cement specimen may have a bright pink interior (where little or no degradation has occurred) that fades toward the exterior of the specimen (where most of the degradation has occurred and the pH is lower). There is an implicit complication in this method since it is a visual observation. Lo and Lee [71] compared the carbonation depth observed through this method against a microstructural assessment for carbonation depth and found that the phenolphthalein method gave less consistent readings

and a 24% lower estimation of the degradation depth. Other studies have also found similar results [10,11].

Microstructural changes

Tests to determine microstructural changes are specifically valuable to identify which compounds have been leached or altered in the cement matrix. This method can assist in supporting a hypothesis of how degradation has occurred. For example, when looking at an XRD pattern of an unleached cement specimen, it is possible to identify compounds present such as CH and ettringite [53,59]. TGA analysis can then provide data on phase transitions and decomposition of compounds [72]. TGA is often used to identify which compounds are present in a specimen after certain exposure times. Chemical analysis using FTIR spectrographs has also been used in a way similar to TGA to detect the existence (or lack) of specific chemical compounds in cement specimens after degradation. However, the ability of FTIR to quantify chemical change has been questioned by several researchers [73].

Catinaud et al. [59] used both TGA and XRD analyses to observe microstructural changes of monosulfoaluminate and ettringite due to calcium leaching in cement-based materials with limestone. Delagrave et al. [68] utilized TGA to observe calcium concentrations throughout decalcified cement pastes and it was noted that as specimens are exposed for longer time periods, a high calcium concentration progressed further toward the center of the specimen. From Alarcon-Ruiz et al. [74], it is known that the following reactions occur as undegraded cement is exposed to increasing temperatures:

- 30-120°C: evaporable water and partial bound water is eliminated.

- 110-170°C: gypsum and ettringite decompose, some carboaluminate hydrates lose water.
- 180-300°C: CSH dehydrates and carboaluminate phases decompose.
- 400-500°C: CH is dehydroxylated.
- 700-800°C: calcium carbonate is decarbonated.

It is standard to consider these temperature windows when determining presence of various compounds using TGA tests [74]. In addition to these, it is important to note that CSH dehydrates in the 180-300°C window mentioned, but it decomposes at wide temperature ranges (40-600°C), which makes it difficult to attribute a single temperature to CSH loss [75]. To better observe the weight loss occurrences, it has become common practice to find the derivative weight to identify peaks where rapid weight loss occurs. This is used to relate peaks with compounds decomposition [76].

When considering calcium leached samples, it is also important to note the decomposition temperatures of leaching products. The main leaching product of concern when using ammonium nitrate is calcium nitrate. Depending on several factors, the primary reactions that end up governing the leaching reaction will vary, this means that the compounds present in the matrix can vary. The following reactions for leaching products are important to consider when using TGA for calcium leached samples [75]:

- 30-225°C: calcium nitrate dehydrates
- ~220°C-375°C: ammonium nitrate dehydrates.
- 450-650°C: calcium nitrate decomposes.
- ~500°C: nitrous oxide (N₂O) decomposes.
- 600-700°C: nitrogen (N₂) and oxygen (O₂) decompose.

Studies have shown that since calcium leaching breaks down binding compounds and introduces new compounds, it can skew the windows previously mentioned for undegraded samples [75]. This means that resulting TGA curves can blend peaks influenced by several compounds and not follow the exact, expected windows as compounds dehydrate and dissociate. Ammonium nitrate can be leftover in the matrix and begins to dehydrate ~220-375°C, but can fully decompose either at low temperature (~320°C), or at a higher temperature (~560°C) [75]. Several factors impact the dissociation of these compounds and can lead them to behave slightly differently.

Table 2 presents an overview of the sources used in this paper for cement degradation quantification techniques. Note that some sources use more than one quantification technique, and some methods can be used to provide more than one form of degradation metrics in the specimen. It is important to note those metrics are not usually identical.

Table 2. Comparison of cement degradation quantification methods.

Scale	Quantification Technique	Information Given	Quantification Method	Reference
Macroscopic	Structural tests	Change in compressive strength, flexural strength, etc.	Compressive test, flexural test, etc.	[11,27,31,33, 41,47–54,57,77,78]
	Mass loss	Change in weight/mass	Weight/mass measurement before and after degradation	[41,50,67,77, 78]
Microscopic	Porosity tests	Change in porosity	SEM	[27]
			MIP	[20,32,33,39, 43,47–49,52,54,78]
	Leached depth	Depth that leaching occurred within specimen	SEM	[20,27,28,39, 67,78]
			Fluorescence	[11,31,33,42, 48,52,56,69,71,77]
	Microstructural change	Chemical/molecular changes that have occurred	TGA	[27,32,43,54, 59,68,77,79]
			XRD	[24,27,28,31, 32,41,43,50,53–56,59,67,77]
FTIR			[71]	

Table C.1. in Appendix C lays out the references used throughout this review to demonstrate the varying methods used to analyze and quantify degradation of cement. Not noted in Table C.1. is the specimen size.

2.1.3. Cement degradation discussion

Overall, the breadth of cement degradation is wide, complex and diverse. Research in this area provides a base for understanding the various relationships and interactions between external factors and the cement matrix. Quantification methods used for cement degradation are based on macroscopic and microscopic observations related to cement damage using damage models. The macroscopic tests are standardized, making them essential for these models and giving empirical context to the damage that has occurred at

the microscopic level. Microstructural methods are essential to understand the physical and chemical changes that cause the macroscale behavior. Macroscale behavior can be used to quantify degradation through damage metrics.

Figure 5 summarizes the minimum and maximum damage observed by the applied damage metrics as outlined in Table C.1. As explained at the beginning of Section 2.1.2, the change in material properties following degradation can be used to represent damage. It should be noted that this method does not account for differences across specimens as far as water-to-cement ratio of the cement, specimen size, exposure time, etc. While this is true, it is still useful to get a general idea of which degradation modes impact the most damage. As observed in Figure 5 and based on the references considered in this review, calcium leaching resulted in the highest level of damage with 84% maximum damage, while carbonation showed the least damage with 6% minimum damage. Sulfate attack exhibited the third-most maximum damage (65%) and the most minimum damage (33%). Chloride penetration had the least amount of damage overall, with 48% maximum damage. Of the studies reviewed, there was only one that looked to find the coupled impact of more than one of these degradation methods on cementitious materials [24]. The damage that specimens would experience due to multiple degradation methods is an area that requires further study.

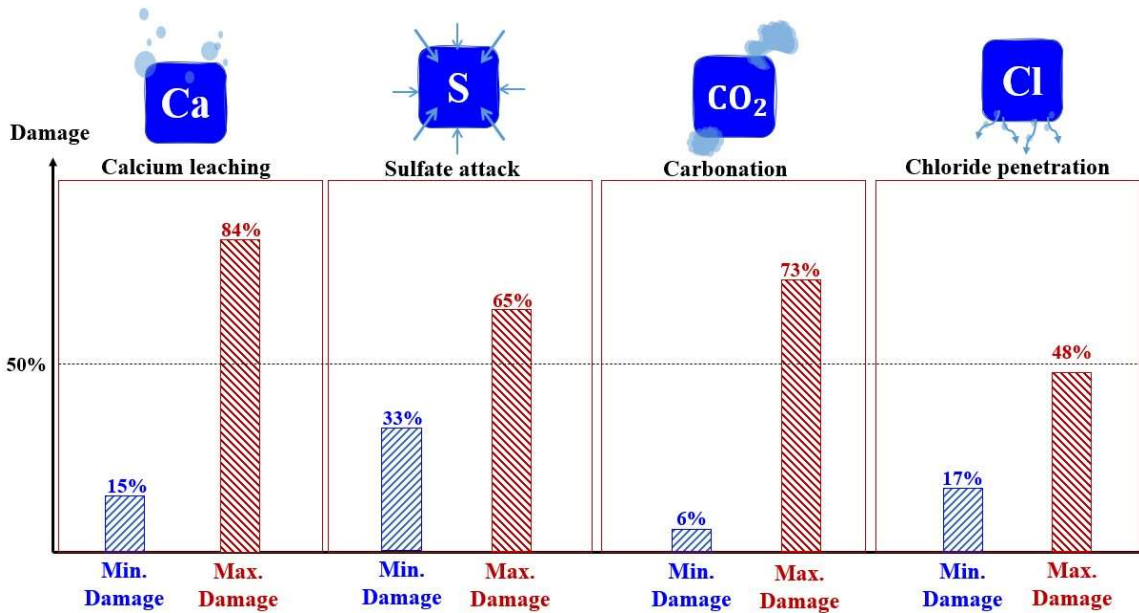


Figure 5. Schematic representation of the level of minimum and maximum levels of cement damage/degradation as reported in the literature noted in Table C.1. Note different quantification methods used with each type of degradation.

2.2. Fracture Mechanics

Fracture mechanics (the study of the propagation of cracks in materials) has been an important area of study alongside the development of modern materials within the past century. Fundamentally, it is understood that two criteria must be met in order for a crack to propagate – the stress criterion and the energy criterion. The stress criterion was defined by Inglis in the early 1900's [80]. It states that there must be sufficient stress at the tip of the crack to break the interatomic bond. The energy criterion was defined soon after by Griffith [81]. It states that there must be sufficient energy to form new surfaces of a crack. From these essential findings, fracture mechanics has grown into a field full of complex and unique theories and methods across all materials.

Regarding fracture, materials are typically grouped by their ductile behavior. If a material is more ductile, such as steel, elastic-plastic and plastic fracture mechanics theories need to be considered. For brittle materials, linear elastic fracture mechanics

theory applies. Concrete is a unique material that is relatively brittle, but cracking enables it to demonstrate some features of plastic behavior. Therefore, it is quasi-brittle due to its composite nature as it has both plastic and elastic characteristics. This makes it difficult to apply one theory to concrete [82,83]. Due to this, there are no standards yet that exist for performing or analysis of fracture testing. There is however an array of work done in the field with certain methods applied. There is also a draft ASTM by the ACI Committee 446 with suggested procedures for fracture tests [84].

The three main models that are applied today are: linear elastic fracture mechanics (LEFM), quasi-brittle fracture mechanics (QBFM), and elastic plastic fracture mechanics (EPFM). Each model defines the resulting fracture toughness – the material’s ability to resist crack propagation - parameter a little differently. Several variables are used with the models: G_f , K_{IC} , G_{IC} , and J_{IC} . Each of these parameters are used to define fracture toughness. G_f is defined as the total fracture energy consumed by a material. K_{IC} is defined as the critical stress intensity factor. G_{IC} is defined as the critical elastic energy release rate. J_{IC} is defined as the critical plastic energy release rate. The model applied in this study is QBFM: elastic crack modulus method, as discussed in the next section. This model was chosen as cement paste can be considered a quasi-brittle material and this is the type of material the model is meant for.

2.2.1. Quasi-brittle fracture mechanics (QBFM) analysis: Elastic crack modulus method

The theory behind quasi-brittle fracture mechanics (QBFM): elastic crack modulus method was first introduced by Jenq and Shah in 1985 [85]. This method assumes the material consumes similar amounts of energy both elastically and through the fracture

process zone (FPZ). This was shown to be an important factor by Shah et al. when they found that concrete materials can consume energy in the FPZ [83]. The method combines pieces of the other methods and uses both flexure and fracture test results to determine fracture properties. It also considers all of the aforementioned fracture properties, whereas other models do not. An additional parameter that is vital to the model is the critical crack tip opening displacement (a_c). Using a secant compliance on the elastic portion of the post-peak load vs. crack mouth opening displacement (CMOD) curve, an estimate of an effective elastic crack length is made. This can be applied in a similar fashion as in the linear elastic fracture mechanics (LEFM) method to obtain the G_{IC} and K_{IC} . In order to best obtain the critical effective crack length, Reda Taha et al. proposed a closed-loop approach as shown below in Figure 6 [82].

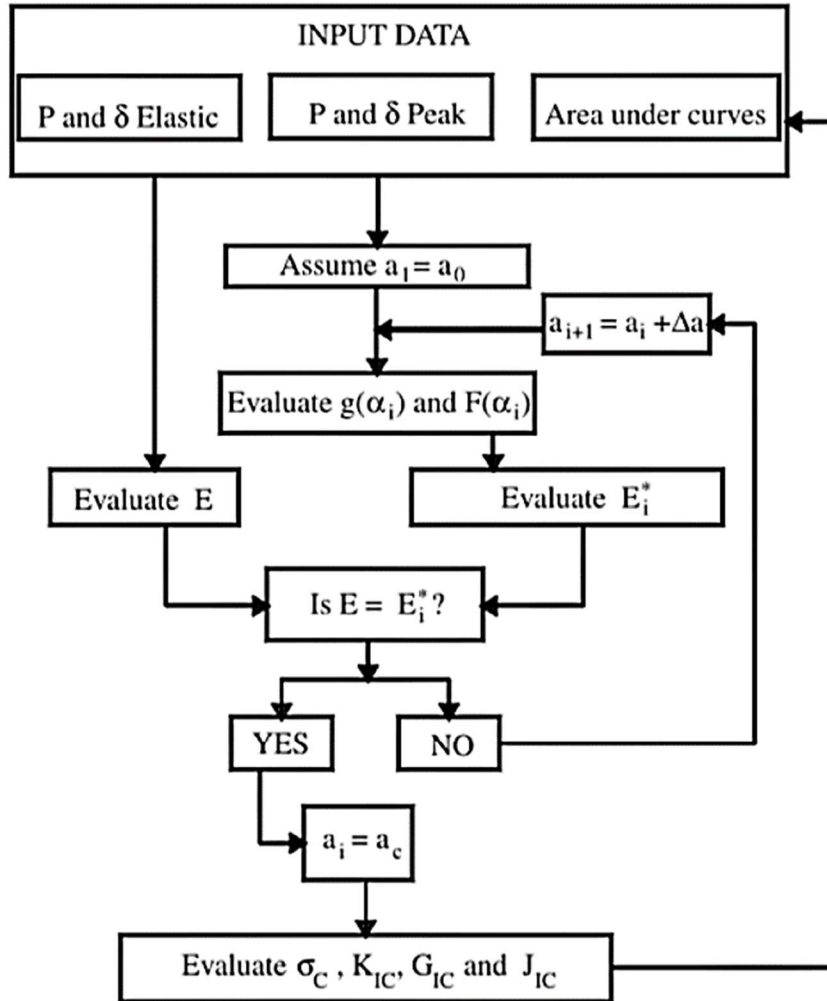


Figure 6. Closed-loop approach for QBFM effective crack modulus [82].

This model obtains the secant modulus by making the elastic modulus equal to the modulus at the peak stress to determine fracture properties. The model has been modified for three-point bending. Details of this method will be described in the Materials and Methods Section (Section 3).

3. MATERIALS AND METHODS

3.1. Sample Preparation

The samples used in this study are cement paste samples with a water/cement ratio of 0.45. They were cast into molds with dimensions 300mm x 25mm x 25mm (L x W x D). Twenty-four hours after casting, samples were demolded and moved to a curing room where the humidity is 99%RH. All samples were allowed to cure unbothered for 6 additional days. At 7 days of age, the samples were individually removed and hand sawn in half lengthwise to make the samples have final dimensions of 150mm x 25mm x 25mm (L x W x D). Final dimensions for both the fracture and flexure specimens are shown below in Figure 7. These dimensions met the ACI 446 report guidelines [84]. The report suggests that sample geometry be decided per the depth, “D”. A sample’s loading span shall be 3 times the depth. Total sample length shall be at least 3 times the depth, plus an additional 50mm. Typically, the width, “B”, is equal to the depth, giving samples a square cross section. For fracture samples, the notch depth shall be $D/3 \pm 10\%$, and the notch width shall be less than $0.02D$. With this, the samples in this study were all 150mm x 25mm x 25mm (L x W x D), with loading spans of 100mm. Fracture samples had notches of depth 8.3mm and width of 0.3mm.

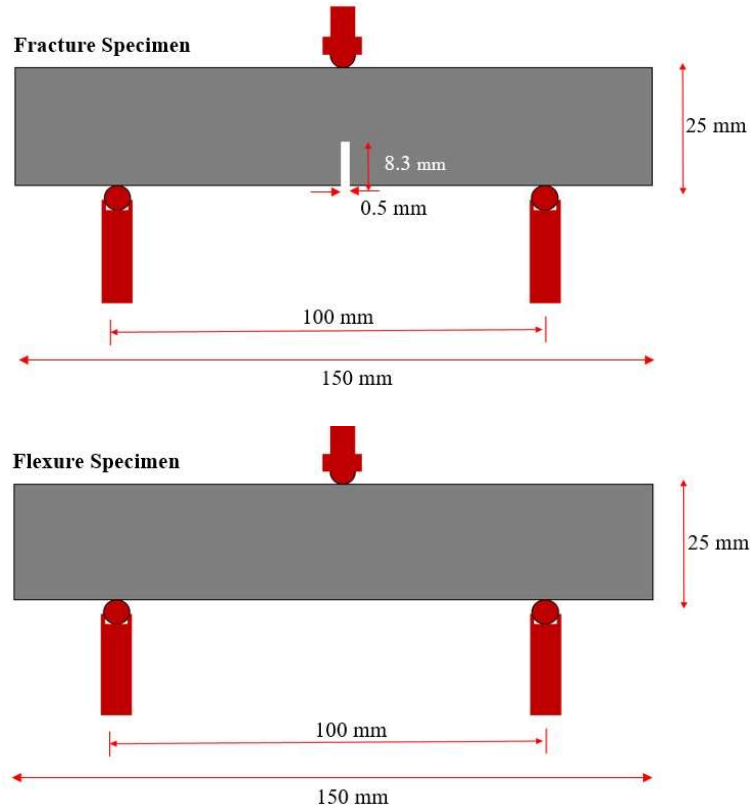


Figure 7. *Top:* Testing dimensions for fracture specimens. *Bottom:* Testing dimensions for flexure specimens.

The steps to notch the fracture specimens is visualized in Figure 8. The specimens were marked at midspan and at the necessary depth for the notch (8.3mm). The initial notch was made using a thin handsaw (thickness = 0.6mm) to obtain half of the final notch depth. The specimen was then taken to the Buehler IsoMet Low Speed precision saw. This precision saw is equipped with a blade of thickness 0.3mm, which was used to touch up the initial notch to the final notch depth. This ensured that the notch meets the ACI 446 guidelines [84].

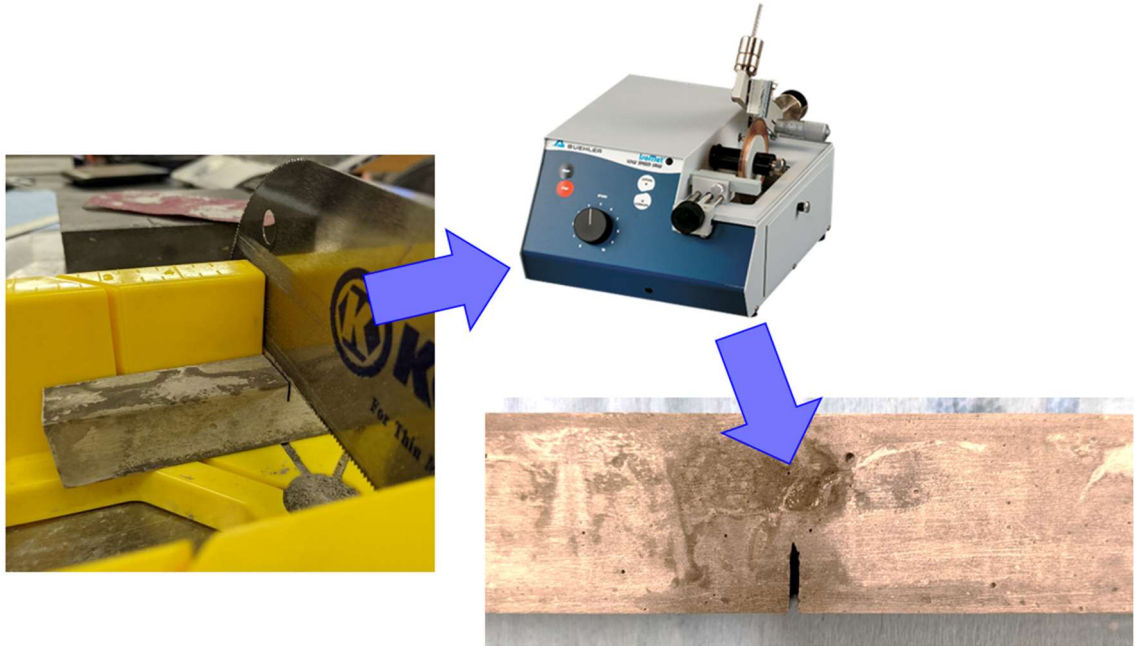


Figure 8. Diagram of steps to attain notch in fracture samples.

Once samples were through the notching process, initial measurements were made of the samples. For the degradation samples, a covering was wrapped around the sample on four of the six faces, as shown in Figure 9. The covering was made such that degradation could only occur through one plane – this simplifies the complex degradation process by limiting it to one direction. The samples were then labeled and placed in their respective degradation mode to be exposed for the predetermined amount of time.



Figure 9. Schematic of the covering on degradation samples.

Samples were labeled according to their exposure time, degradation mode, relative humidity exposure, type of test, and sample number within a scenario set. Exposure time

was considered to be number of weeks exposed. Degradation mode was either “NEAT”, “SULF”, or “NHNO” – NHNO is shorthand for the chemical formula of ammonium nitrate (NH_4NO_3). Relative humidity exposure was either “0” for 16%RH, “50” for 50%RH, or “99” for 99%RH. Type of test was either “N” for notched fracture test or “U” for unnotched flexure test. Sample number was simply 1-6, as 6 samples were tested for each scenario set. For example, the 1-week, neat, 99%RH, fracture sample that was the first in the set was labeled: “1NEAT99N-1”.

Exposures that are considered are: neat, 12-, and 24-week exposures. For each scenario set, 6 fracture and 6 flexure tests were planned in order to be able to obtain flexure and fracture properties. Table 3 outlines the testing matrix – tests that have been completed have an “X”. The “N1” (the 12-week, calcium leached, 16%RH exposure, fracture tests), reflects a batch that was not tested due to visible cracks stemming from the notch prior to testing. This was likely due to the severe degradation observed at 12-weeks of calcium leaching exposure and any drying that took place in the low humidity. The other, “N2” (the 12-week, sulfate attack, 16%RH exposure, fracture tests), reflects a batch that was tested, but removed from analysis due to unreasonable results. This could be due to the 12-week tests being the first tests performed for this report and the loading process had not been finalized yet. Boxes with an asterisk were determined to be unable to test due to excessive degradation.

Table 3. Scenario sets for experimental program. “X” marks the tests that have been completed at the time of this report.

Exposure time (weeks)	Degradation mode	Humidity exposure	Fracture	Flexure
1	Neat	16%RH	X	X
		50%RH	X	X
		99%RH	X	X
12	Neat	16%RH	X	X
		50%RH	X	X
		99%RH	X	X
	Calcium leaching	16%RH	N1	X
		50%RH	X	X
		99%RH	X	X
	Sulfate attack	16%RH	N2	X
		50%RH	X	X
		99%RH	X	X
24	Neat	16%RH	X	X
		50%RH	X	X
		99%RH	X	X
	Calcium leaching	16%RH	*	*
		50%RH	*	*
		99%RH	*	*
	Sulfate attack	16%RH	X	X
		50%RH	X	X
		99%RH	X	X

*Unable to be tested.

3.2. Degradation

Once the samples were properly prepared and initial measurements had been taken, they were placed into their respective degradation mode – neat, calcium leaching, or sulfate attack. The neat samples were simply placed back into the curing room. The calcium leaching samples were placed into an ammonium nitrate (NH_4NO_3) solution bath with concentration of 480 g/L (6M). The sulfate attack samples were placed into a sodium sulfate (Na_2SO_4) bath with concentration 50 g/L (0.35M). The baths are shown in Figure 10.

Each bath was equipped with a pump to constantly stir the solution. The pump was located in the lower half of the bath and effectively stirred the solution in the horizontal plane. The solutions were entirely renewed once every four weeks, this process was

performed to mitigate oversaturation. pH of the solutions was monitored every few weeks for quality control using a pH meter. Temperature was monitored as well, but there were no temperature control methods implemented. The calcium leaching solution (ammonium nitrate) has a neat pH around 5 and the sulfate attack solution (sodium sulfate) has a neat pH of about 6. Cement paste is a base and has a natural pH ~ 12 . Once samples are exposed to the solution and chemical reactions begin, the pH changes within a day or two. The calcium leaching solution increases from a pH of 5 to around 9. The sulfate attack solution increases from a pH of 6 to 12.

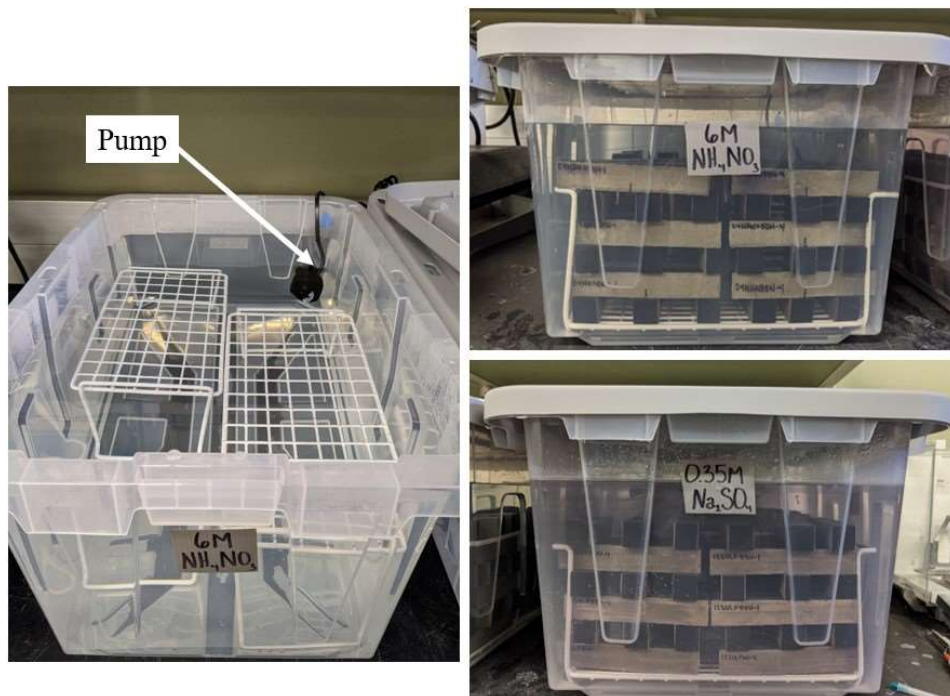


Figure 10. *Left:* Bath with no samples, showing pump location. *Right:* Both degradation baths with samples.

As samples degraded, measurements were periodically taken to monitor dimension, weight, and therefore density changes. Measurements were taken after cure and after 1, 2, 3, 4, 8, 12, 16, and 24 weeks of exposure.

3.3. Humidity Exposure

Once samples had been exposed to their respective degradation mode for their pre-determined amount of time, they were exposed to their respective relative humidity prior to fracture testing. The 16%RH environment was simply the ambient condition in the structures laboratory – this is the natural relative humidity of the lab and was monitored using a hygrometer. The ambient humidity did not vary while samples were exposed to it. The 50%RH environment was constructed using a large, plastic storage container and a humidifier that could maintain a set humidity. The humidifier maintained the humidity within the chamber at $50 \pm 7\%$ RH. Images of the 50%RH chamber are shown in Figure 11. Both the 16%RH and 50%RH conditions were monitored using hygrometers while samples were exposed. The 99%RH environment was the same room the samples are cured in that maintains 99%RH using misters.



Figure 11. Showing the 50%RH chamber which was comprised of a 50-gallon container, rack for samples, humidifier, and hygrometer.

Early on, it was determined that the samples would be exposed to their relative humidity exposure overnight. To observe the weight change that samples would undergo when exposed to the 16%RH and 50%RH conditions overnight, a preliminary test was performed. Typical samples from the 99%RH exposure were placed in both the ambient, 16%RH and intermediate 50%RH conditions and periodically weighed for 48 hours. Two samples were observed for each humidity exposure and averaged. A graph illustrating the results of this preliminary test is shown in Figure 12. It was observed that after about 20 hours, an approximate 2.8% and 2.1% weight loss was observed for the 16%RH and 50%RH exposures, respectively. 20 ± 2 hours of exposure to the relative humidity condition was implemented for the tests.

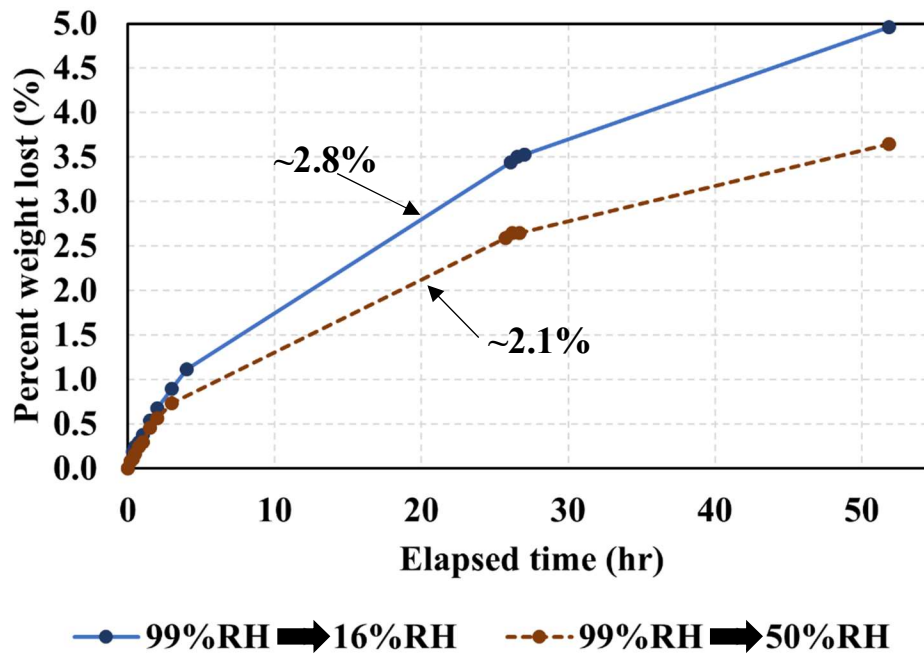


Figure 12. Results from preliminary relative humidity exposure test.

Prior to placing the samples in their humidity exposure, the degradation covering was removed. Samples were then left unrestrained on a rack in their respective relative

humidity exposure overnight. On the day of testing, samples were all weighed and then wrapped in plastic to prevent further moisture loss before testing.

3.4. Fracture Toughness Tests

The tests performed were done per the ACI 446 report [84]. While not an official ASTM for fracture testing, it was composed by authors in the field of fracture testing on concrete; it has guidelines for dimensions and loading setup. Another reference that was used was previous work by Douba in 2017 – this work also utilized the ACI 446 report [86].

The report also has guidelines to prevent unstable failure due to the self-weight of the sample. This can be achieved either by ensuring the sample overhang is sufficient or implementing counterweights. Counterweights were utilized in this study. The report suggests that counterweights should be put in place such that they create a hogging bending moment at the midspan within the range of $mgS/32 < M < mgS/16$. Where m is the sample mass, g is specific gravity, S is the loading span, and M is the resulting moment at midspan. The schematic used to calculate the counterweight positioning is shown below in Figure 13.

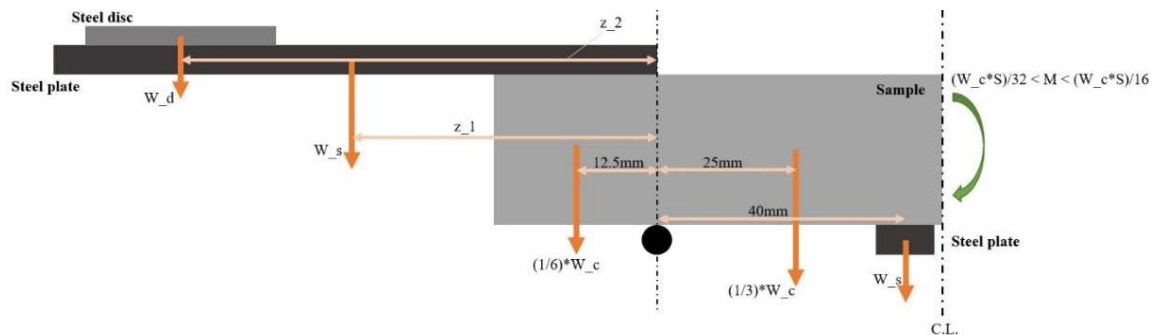


Figure 13. Schematic of the testing setup used to calculate the counterweight positioning.

Figure 13 is a front view of one half of the test setup, it shows the forces in orange, distances in tan, and the moment in green. W_d is the weight of the steel disc, W_s is the

weight of the steel plates, W_c is the total weight of the cement sample, z_1 is the distance from the support to the center of gravity of the steel plate, and z_2 is the distance from the support to the center of gravity of the steel disc. W_s and W_d were the only two values that were constant when determining the moment for each sample. Since the weight of the samples varies from test to test, calculations were performed for each experiment to determine the placement of the steel disc to ensure the proper moment was attained. This was done through the use of computer code where the weight of the sample could easily be changed to determine the possible range for z_2 . Images of this code in Mathcad can be found in Appendix B (for a sample weighing 190g). Depending on the weight of the sample, z_1 also had to be adjusted.

3.4.1. Test setup

When it was time to test the samples and they had spent approximately 20 hours in their respective relative humidity exposure, they were weighed and wrapped in plastic to prevent any further moisture loss. Final dimension measurements were taken just before testing. Fracture samples were spray painted white on their front face and marked such that they could be recorded via video camera. This gave the backup option to utilize digital imaging correlation (DIC) if the displacement data was not usable.

Before testing, samples were removed from the plastic, marked for the DIC recording and at supports, measurements taken, and then steel plates, frame, and the counterweights were attached. Steel plates were attached with superglue at the bottom of the sample for the Linear Variable Differential Transformers (LVDTs), used to measure axial displacement. The steel plates for the fracture samples have knife edges attached at the center for the Crack Mouth Opening Displacement (CMOD) gage. The frame was attached

using hot glue above the support locations – this ensured that the frame did not influence any moment on the sample. The counterweights were attached using hot glue as determined using the Mathcad code as previously discussed. An image of a sample ready for testing is shown in Figure 14.

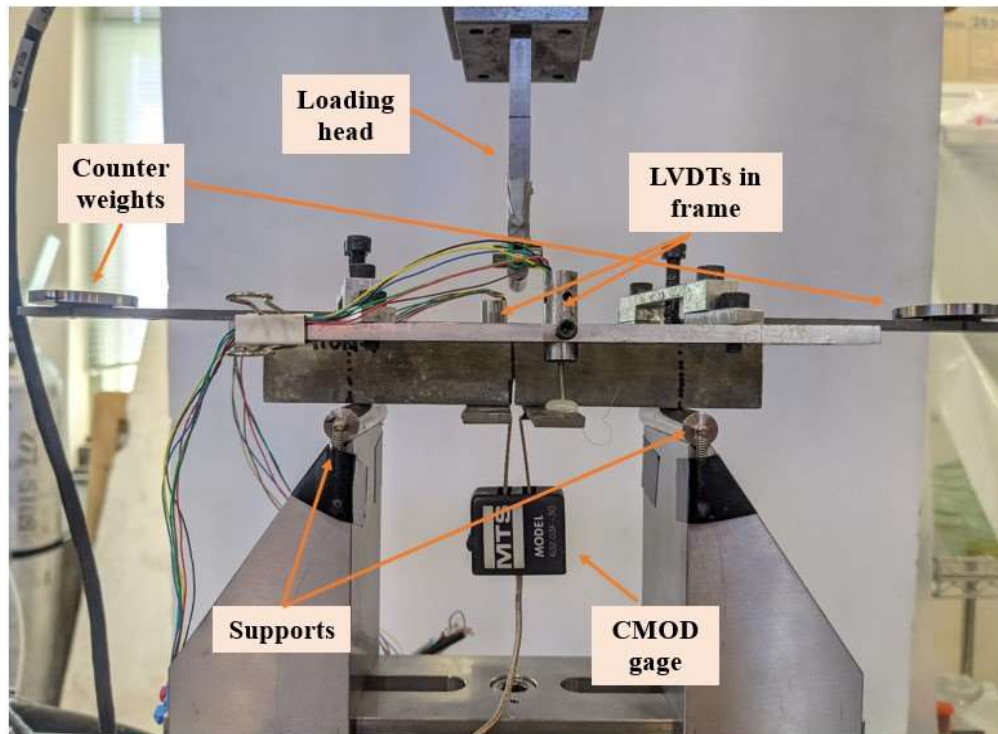


Figure 14. Fracture sample ready for testing, showing all measurement and counterweight accessories.

3.4.2. Loading procedure

As cement paste is a very brittle material, an extremely low loading rate was necessary to capture the post-peak behavior of the fracture samples. The ACI report suggests using a CMOD feedback loop to control the loading rate, but the machinery used could not support this. Instead, a stepped loading rate procedure based on load limits was implemented. Through preliminary testing, it was determined that a loading rate of 0.0005mm/min could reliably capture the post-peak behavior of the fracture specimens. Since this rate is extremely slow, a stepped loading rate procedure was used up to 50-75%

of the estimated peak load. The initial the loading rate was 0.003mm/min up to Limit 1. Limit 1 was determined to be ~15-20% of the estimated peak load. The next loading rate was 0.002mm/min up to Limit 2. Limit 2 was determined to be ~30-40% of the estimated peak load. The penultimate loading rate was 0.001mm/min up to the final Limit 3. Limit 3 was 50-75% of the estimated peak load. Once Limit 3 was met, the final loading rate of 0.0005mm/min was used until the test was complete. Since this methodology depends on the peak load, the first sample for each scenario set was used as a gauge for what Limit 1, Limit 2, and Limit 3 would be for the remaining samples in that set. The loads at which the loading rate would adjust for each fracture scenario set completed so far are shown below in Table 4.

Post-peak behavior is not necessary for the flexure testing, so a similar loading rate procedure without Limit 3 was implemented. Only the first three rates were used, this means that the slow 0.0005mm/min was not used. For example, up to Limit 1, 0.003mm/min loading rate was used Then up to Limit 2, the 0.002mm/min loading rate was used. Once Limit 2 was met, the remainder of the test was performed using the 0.001mm/min rate. Similar to the fracture tests, the first sample in a scenario set was used to gage what the estimated peak load would be to determine Limit 1 and Limit 2. The loads at which the loading rate would adjust for each flexure scenario set completed so far are presented below in Table 5. Generally, the limits were similar within sets that shared exposure time and degradation mode.

Table 4. Load limits that loading rate changed for the fracture tests performed.

	Limit 1 (N)	Limit 2 (N)	Limit 3 (N)
1NEAT0	15	30	45
1NEAT50	20	40	60
1NEAT99	15	30	45
12NEAT0	30	50	70
12NEAT50	20	40	60
12NEAT99	30	50	70
12SULF50	14	28	42
12SULF99	20	40	60
12NHNO50	-	10	15
12NHNO99	-	10	15
24NEAT0	25	50	70
24NEAT50	17	34	51
24NEAT99	14	28	42
24SULF0	15	30	45
24SULF50	15	30	45
24SULF99	15	30	45

Table 5. Load limits that loading rate changed for the flexure tests performed.

	Limit 1 (N)	Limit 2 (N)
1NEAT0	100	200
1NEAT50	40	80
1NEAT99	40	80
12NEAT0	100	175
12NEAT50	200	400
12NEAT99	100	175
12SULF0	50	75
12SULF50	50	100
12SULF99	50	100
12NHNO0	45	90
12NHNO50	45	90
12NHNO99	45	90
24NEAT0	100	200
24NEAT50	125	250
24NEAT99	150	300
24SULF0	50	100
24SULF50	50	100
24SULF99	50	100

For both fracture and flexure tests, each test took an average of ~70 minutes to complete. Once the test was complete, the frame and steel plates were removed from the sample, photos of the fracture were taken, and the sample was wrapped in plastic once

again to ensure no further moisture loss until the leached depth analysis could be performed.

3.5. Leached Depth Quantification

Since previous studies had shown that leached depth is not best quantified by visual approximation via fluorescence, both fluorescence and a microstructural method were implemented. Once samples had completed their test, 2 samples from each exposure time were taken to perform leached depth analysis on. Samples were cut at quarter-span to obtain two 5mm x 25mm x 25mm (L x W x D) samples. One had a low-concentration phenolphthalein solution applied to obtain the visual approximation. Phenolphthalein turns deep pink when applied to a more basic pH material, and colorless when applied to a neutral or acidic material. Neat cement paste has a pH ~12, turning the solution deep pink. Leached areas of a cement paste matrix do not change color.

The other cut sample was cut again through the degradation plane every 5mm, producing five 5mm x 5mm x 25mm (L x W x D) samples for the TGA analysis. From these samples, a 10-20 mg piece was tested in the TGA with a heating rate of 20°C/min up to 800°C with an air flow of nitrogen at 40 ml/min. This microstructural method supplements the visual readings and gives a more specific picture of what compounds are present in the cementitious matrix.

3.6. Analysis

After tests were completed, several forms of analysis were performed. The data from the tests (load, displacement, and CMOD) had to be processed and aligned as the LVDTs used a separate system from the load and CMOD system. Both systems recorded data at intervals of 0.01s. A Matlab code was used to calculate the mechanical and fracture

characteristics – detailed in the fracture model described below – from the data. The Matlab codes used can be found in Appendix A.

Another layer to the analysis that was included was the implementation of t-tests. T-tests are statistical tests used for small batches of data to determine if the difference between two groups of data is significantly higher than the difference within the groups themselves. One group is held as a control. This statistical test gives a p-value, which ranges from 0-1. It is up to the user to set a confidence interval to determine if the p-value reflects significance or not. The confidence interval used in this study is 95%, meaning that a p-value of 0.05 or less reflects significance. A p-value greater than this reflects that the groups are not significantly different. This test is a pass-fail test, meaning that once the confidence interval is set, either the results is that the two sets are significant or not. T-tests were used to evaluate if the relative humidity exposure made a significant impact on measured values. For these t-tests, the constant batch was assumed to be the 99%RH results. T-tests were also used to help understand how properties evolve with exposure time for the neat and sulfate attack tests performed. For these t-tests, the constant batch was assumed to be the 12-week results.

3.6.1. Fracture model

The fracture model utilized in this study is the quasi-brittle fracture mechanics (QBFM), as previously mentioned in Section 2. A Matlab code was used to first process and align the data, which could then be used to find mechanical properties and definitive test values to serve as inputs into the closed-loop model. For each scenario set, at least four representative tests were used to obtain properties. The input values were the flexural peak load ($P_{U,peak}$), elastic displacement ($\delta_{elastic}$), fracture peak load ($P_{N,peak}$), peak displacement

(δ_{peak}), and the area under the flexure and fracture curves (A_N and A_{UN}). These values were then used in an iterative process to obtain the effective critical crack length, a_c . Once this value was determined, it could be used to determine the fracture properties (G_f , K_{IC} , G_{IC} , J_{IC}). Eq. (5) through Eq. (20) below were used in the Matlab code, which can be found in Appendix A.

$$E_{UN} = \frac{1}{bd\delta_{eUN}} * \left(0.9745 * \frac{P_{eUN}l^3}{4d^2} + \frac{13}{15} * \frac{3*(1+\nu)*P_{eUN}l}{4} \right) \quad (5)$$

$$MOR = \frac{3P_{eUN}l}{2bd^2} \quad (6)$$

$$H_c = d - a_c \quad (7)$$

$$\alpha = \frac{a}{d} \quad (8)$$

$$g_1(\alpha) = 1.122 - 1.4\alpha + 7.33\alpha^2 - 13.08\alpha^3 + 14\alpha^4 \quad (9)$$

$$g(\alpha) = g_1(\alpha) * \sqrt{\pi} \quad (10)$$

$$F(\alpha_i) = \int_0^{\alpha_i} (\alpha * g(\alpha)^2) d\alpha \quad (11)$$

$$n_p = \frac{P_c}{N_c} \quad (12)$$

$$A_N = \sum_{i=0}^{n_p} \frac{(\Delta_{N,i+1} - \Delta_{N,i}) * (P_{N,i+1} + P_{N,i})}{2} \quad (13)$$

$$A_{UN} = \sum_{i=0}^{n_p} \frac{(\Delta_{UN,i+1} - \Delta_{UN,i}) * (P_{UN,i+1} + P_{UN,i})}{2} \quad (14)$$

$$E_{elastic} = \frac{1}{bd_e} * \left(0.9745 * \frac{P_e l^3}{4d^2} + \frac{13}{15} * \frac{3*(1+\nu)*P_e l}{4} + \frac{13}{15} * \frac{9P_e l^2}{2d} * F(\alpha) \right) \quad (15)$$

$$E_{critical} = \frac{1}{bd\delta_c} * \left(0.9745 * \frac{P_c l^3}{4d^2} + \frac{13}{15} * \frac{3*(1+\nu)*P_c l}{4} + \frac{13}{15} * \frac{9P_c l^2}{2d} * F(\alpha_c) \right) \quad (16)$$

$$G_f = \frac{1}{b(d-a)} * \int_0^{\delta_c} P(\delta) d\delta \quad (17)$$

$$K_{IC} = g_1(\alpha) \sigma_c \sqrt{\pi \alpha_c} \quad (18)$$

$$G_{IC} = \frac{K_{IC}^2(1-\nu^2)}{E_{UN}} \quad (19)$$

$$J_{IC} = \frac{2}{H_c b} * (A_N - A_{UN}) \quad (20)$$

- Notation -

a : crack depth (mm)

a_c : critical crack depth (mm)

A_N : area under the load-displacement curve of notched specimen up to the peak load (N*mm)

A_{UN} : area under the load-displacement curve of unnotched specimen up to the peak load of similar notched specimen (N*mm)

b : specimen's width (25mm)

d : specimen's depth (25mm)

$E_{elastic}$: plane strain elastic modulus of notched specimen (MPa)

$E_{critical}$: plane strain elastic modulus of an imaginary beam including effective elastic crack (MPa)

E_{UN} : elastic modulus of unnotched specimen (MPa)

$g_1(\alpha)$: geometric correction factor

G_{IC} : critical energy release rate (N/m)

H_c : critical ligament length (mm)

J_{IC} : critical plastic energy release rate (N/m)

K_{IC} : critical stress intensity factor

l : loading span (100mm)

MOR : modulus of rupture of unnotched specimen (GPa)

N_c : number of steps up to peak load of notched specimen

P_e : load at elastic limit of notched specimen (N)

P_{eUN} : load at defined elastic limit of unnotched specimen (N)

P_c : peak load of notched specimen (N)

$P_{N,i}$: load at given time step for notched specimen (N)

$P_{UN,i}$: load at given time step for unnotched specimen (N)

α : notch to depth ratio

α_i : initial notch to depth ratio

α_c : critical notch to depth ratio

δ_e : displacement at the elastic limit of notched specimen (mm)

δ_{eUN} : displacement at defined elastic limit of unnotched specimen (mm)

δ_c : displacement at peak load of notched specimen (mm)

$\Delta_{N,i}$: displacement at given time step for notched specimen (mm)

$\Delta_{UN,i}$: displacement at given time step for unnotched specimen (mm)

σ_c : critical stress of notched specimen (MPa)

ν : Poisson's ratio of cement paste (0.26)

3.6.2. Damage quantification

To better compare results, metrics were defined for the two quantification methods implemented in this study: $D_{E,I}$ for change in stiffness and $D_{l,i}$ for leached depth. These metrics were outlined in Section 2. Eq. (2) was used to quantify damage through change in stiffness due to degradation, called $D_{E,i}$. Eq. (4) was applied to the measured leached depth, with the damage as the percentage of the width or diameter lost to leaching. $D_{l,i}$ is used to denote this damage metric with l_i as the leached depth at the i^{th} instant and l_0 as the dimension being affected (width). Eq. (4) assumes the dimension affected by leaching is not affected by degradation in any other dimension. All values for damage metrics are reported as a percentage. These metrics are compared directly and the results for each degradation mode are summarized later in the discussion.

4. RESULTS AND DISCUSSION

The following results evaluate changes observed due to calcium leaching and sulfate attack of cement paste samples through density observations, fracture and flexure tests, and a leached depth analysis. When considering the following results, it is important to keep in mind the mechanisms that occur within the cementitious matrix for each degradation mode (calcium leaching and sulfate attack). Generally, for normal Portland cement, it is known that rapid strength gain is observed within the first 4-5 weeks of being cast [1]. After this period of time, the strength and characteristic properties tend to plateau as the majority of reactions that lead to strength gain have occurred to their full extent. When calcium leaching occurs due to ammonium nitrate, the ammonium nitrate reacts with CH to form calcium nitrate, ammonia, and water [11]. As discussed in Section 2, sulfate attack occurs when sulfates are either externally introduced to the matrix to prompt further formation of ettringite that the hardened matrix cannot handle or the initial formation of ettringite is interrupted somehow and reinitiated later when the matrix has already hardened [1,16]. Sulfate attack disrupts the matrix by forming more binding compounds, whereas calcium leaching breaks down and removes binding compounds entirely.

4.1. Fracture Toughness Tests

The fracture toughness tests were evaluated as outlined in Section 3. Through the tests performed, the extremely brittle nature of cement paste was realized. The counterweight calculations proved to be very important to be able to properly capture the post-peak behavior of the cement paste samples and avoid abrupt failure. The tests completed at this stage of the work took an average of 70 minutes to complete.

Resulting median load-displacement curves for the flexure tests performed are shown below in Figures 15-20. Considering the 12-week results (Figures 16-18), a large loss in stiffness and maximum load is observed from the neat curves to the degraded curves. The 24-week results (Figures 19-20) also reflect a similar trend, with the sulfate attack samples observing lessened stiffness and peak load than the neat samples.

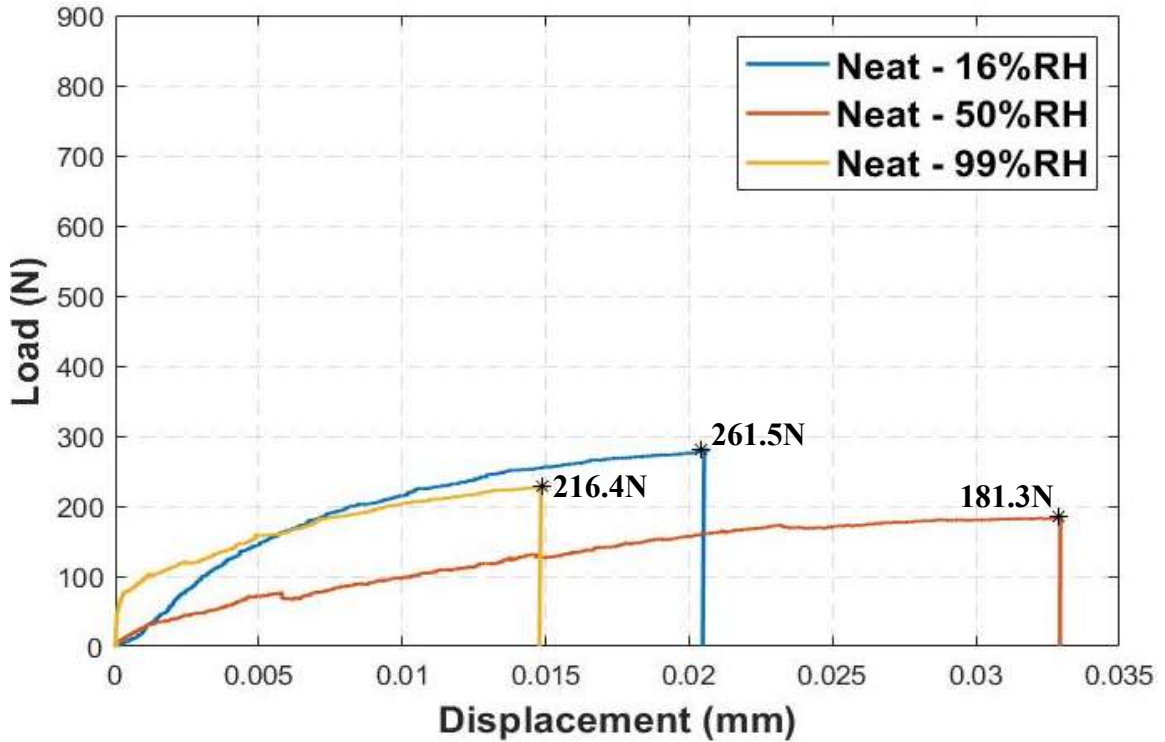


Figure 15. Median load-displacement curves for the 1-week, neat flexure tests.

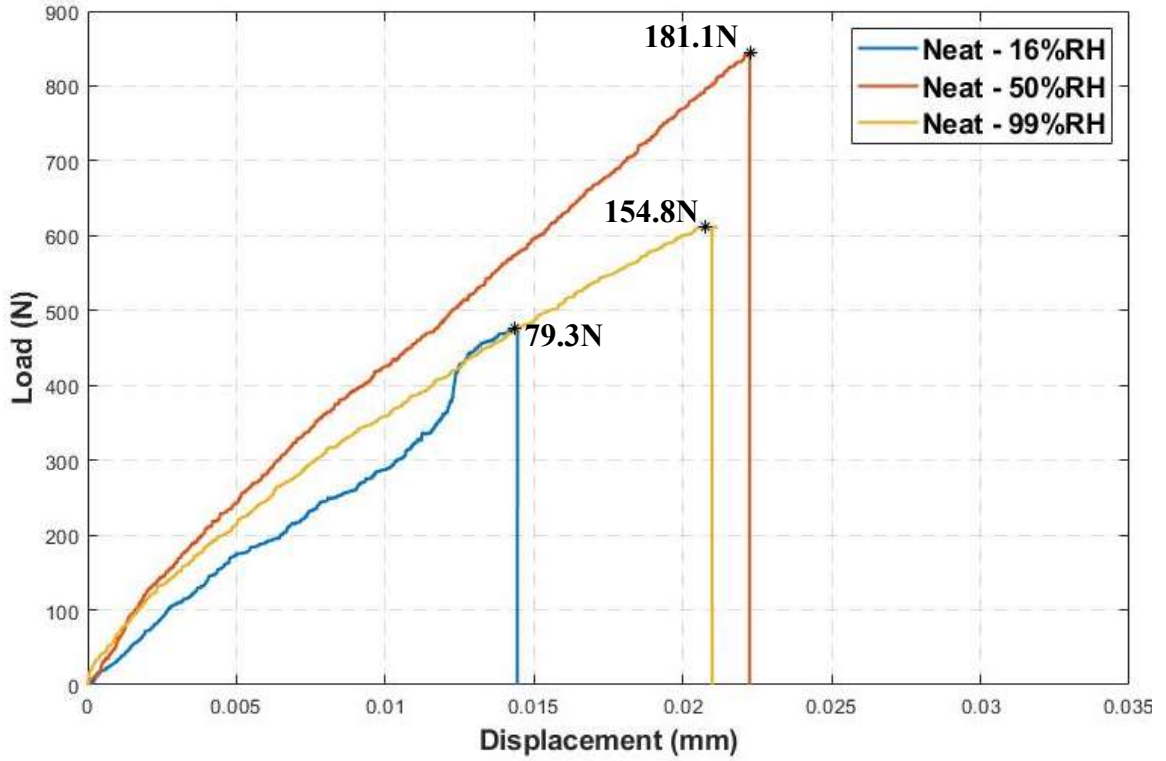


Figure 16. Median load-displacement curves for the 12-week, neat flexure tests.

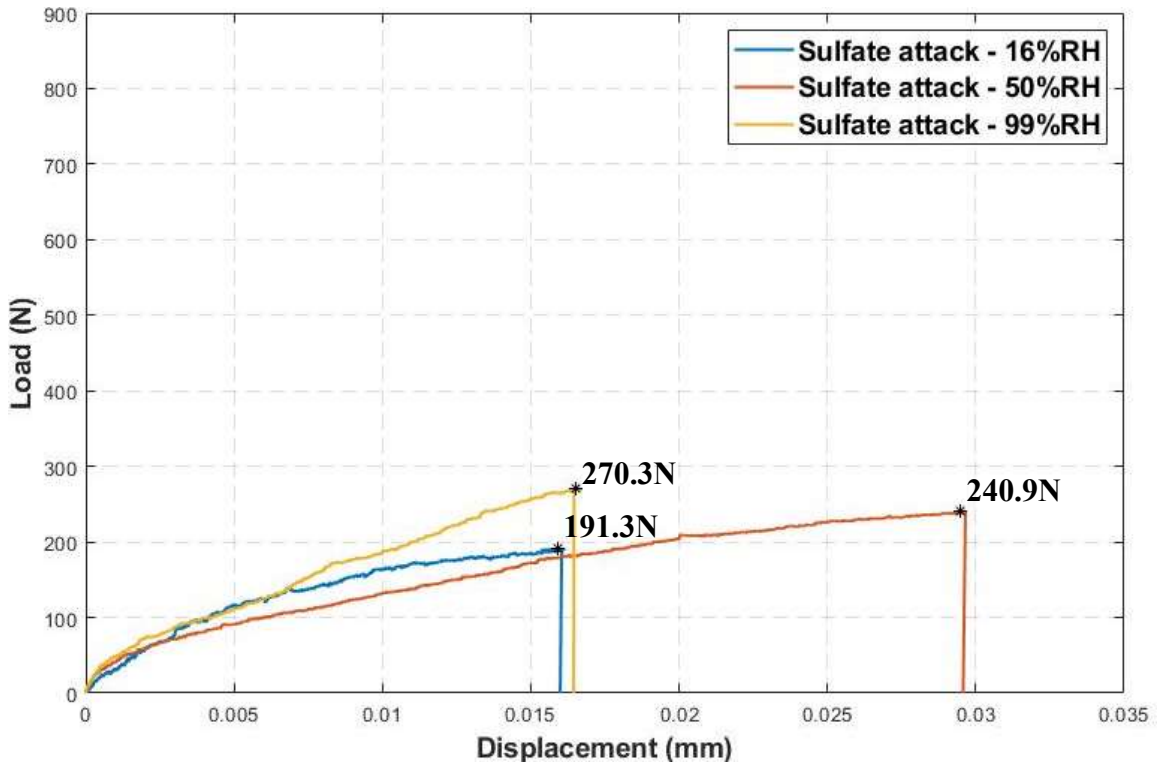


Figure 17. Median load-displacement curves for the 12-week, sulfate attack flexure tests.

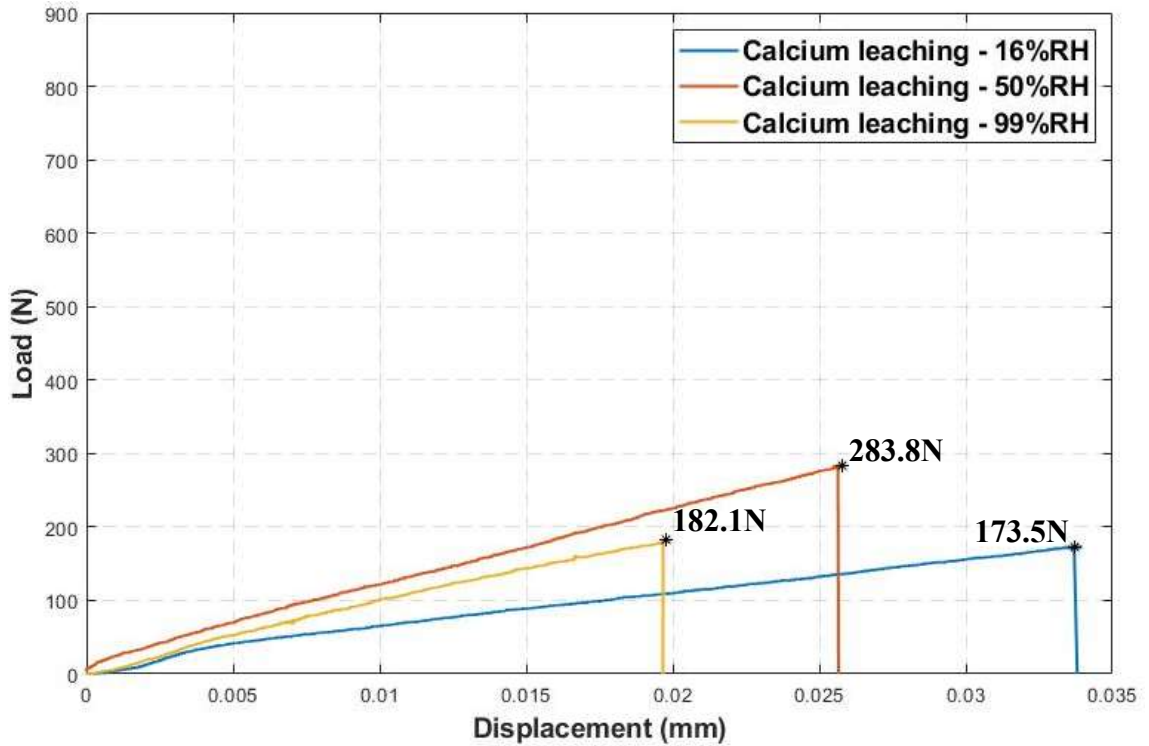


Figure 18. Median load-displacement curves for the 12-week, calcium leaching flexure tests.

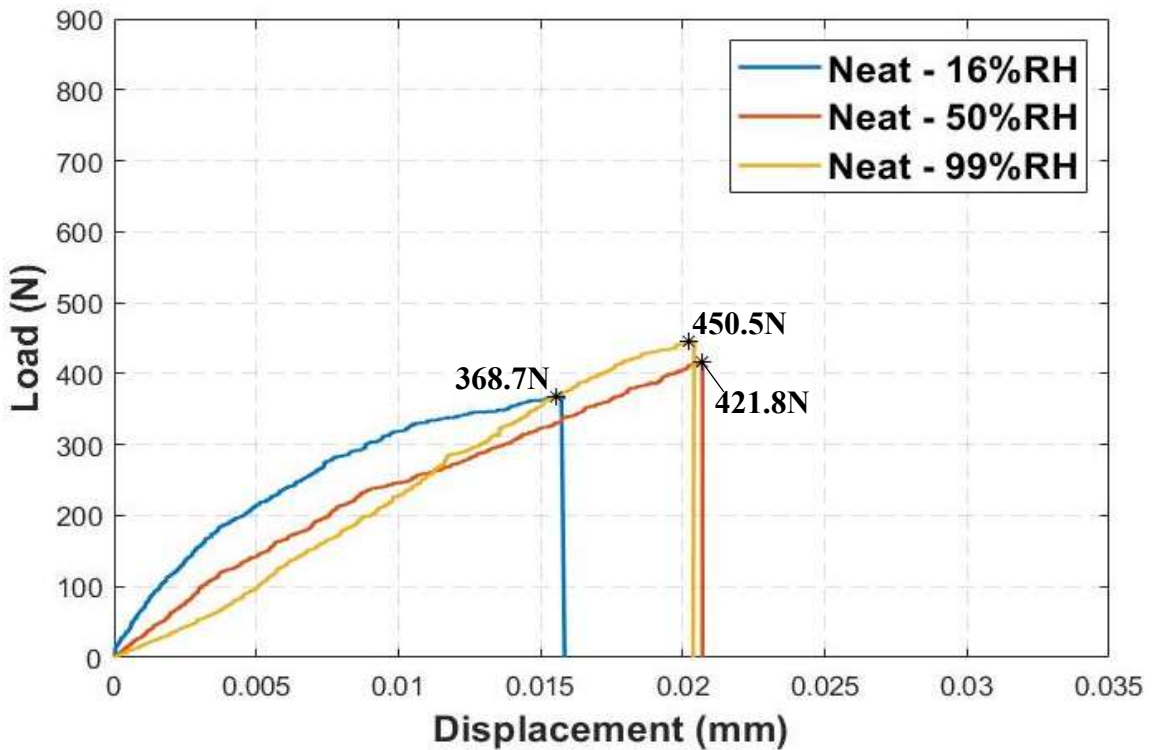


Figure 19. Median load-displacement curves for the 24-week, neat flexure tests.

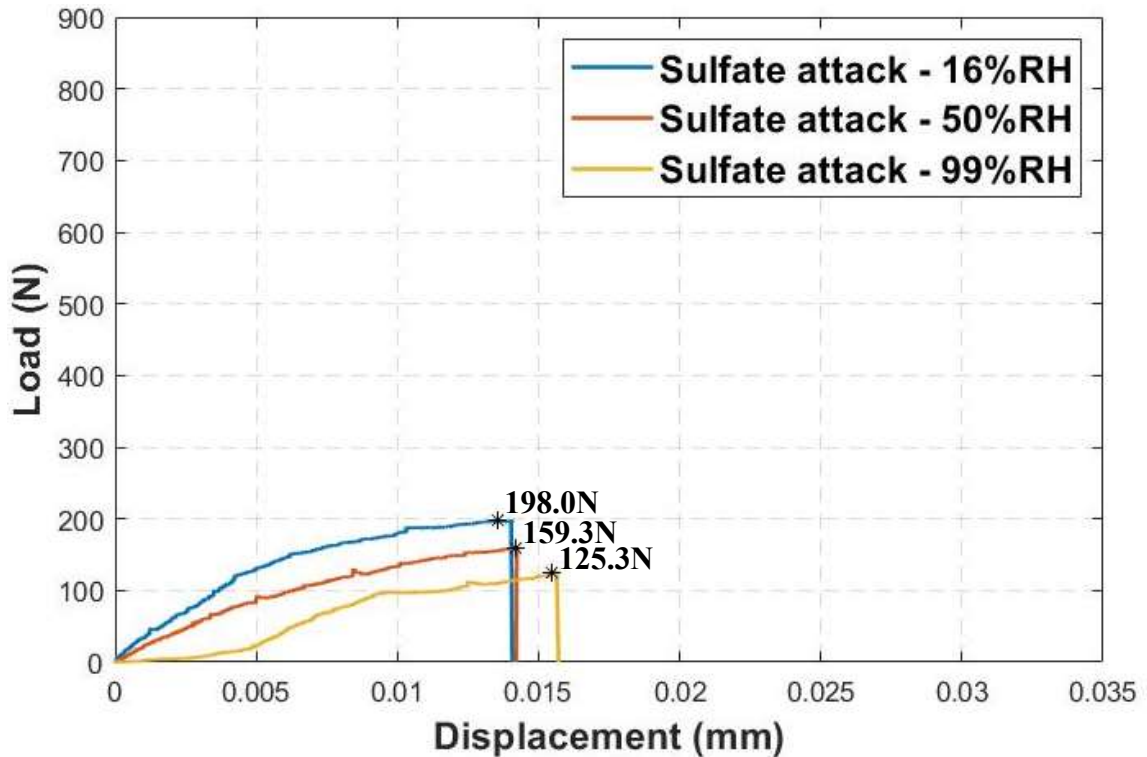


Figure 20. Median load-displacement curves for the 24-week, sulfate attack flexure tests.

Resulting median load-CMOD curves for the completed tests are shown below in Figures 21-26. The 12-week load-CMOD curves (Figures 22-24) portray that the calcium leaching impacts the peak load and stiffness the most. Note that the 12-week sulfate attack and calcium leaching tests for the 16%RH exposure are not shown in the graph. As a reminder, these tests were removed either due to inconsistencies in results or inability to test. The 24-week load-CMOD curves (Figures 25-26) do not follow the same trends observed in the 24-week load-displacement curves (Figures 19-20) or in the 12-week load-CMOD curves (Figures 22-23); the load-CMOD curves for the neat and sulfate attack samples seem overall similar at 24-weeks with no clear difference between the two.

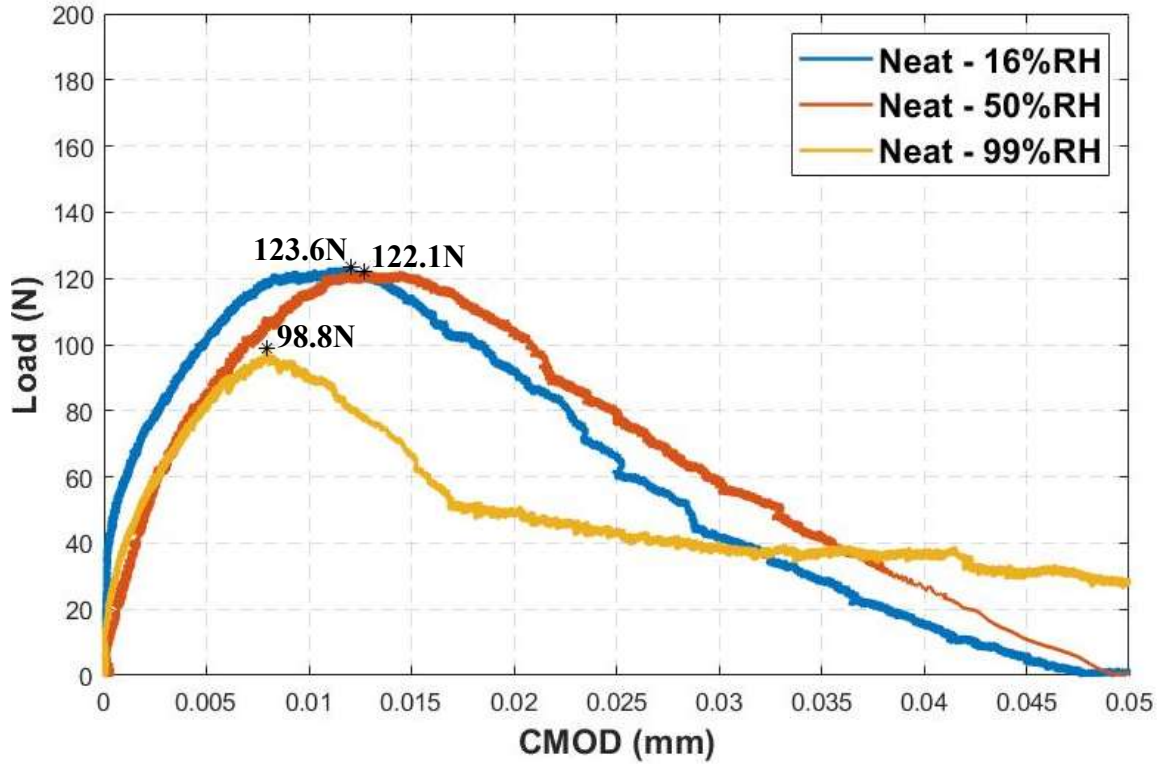


Figure 21. Median load-CMOD curves for the 1-week, neat fracture tests.

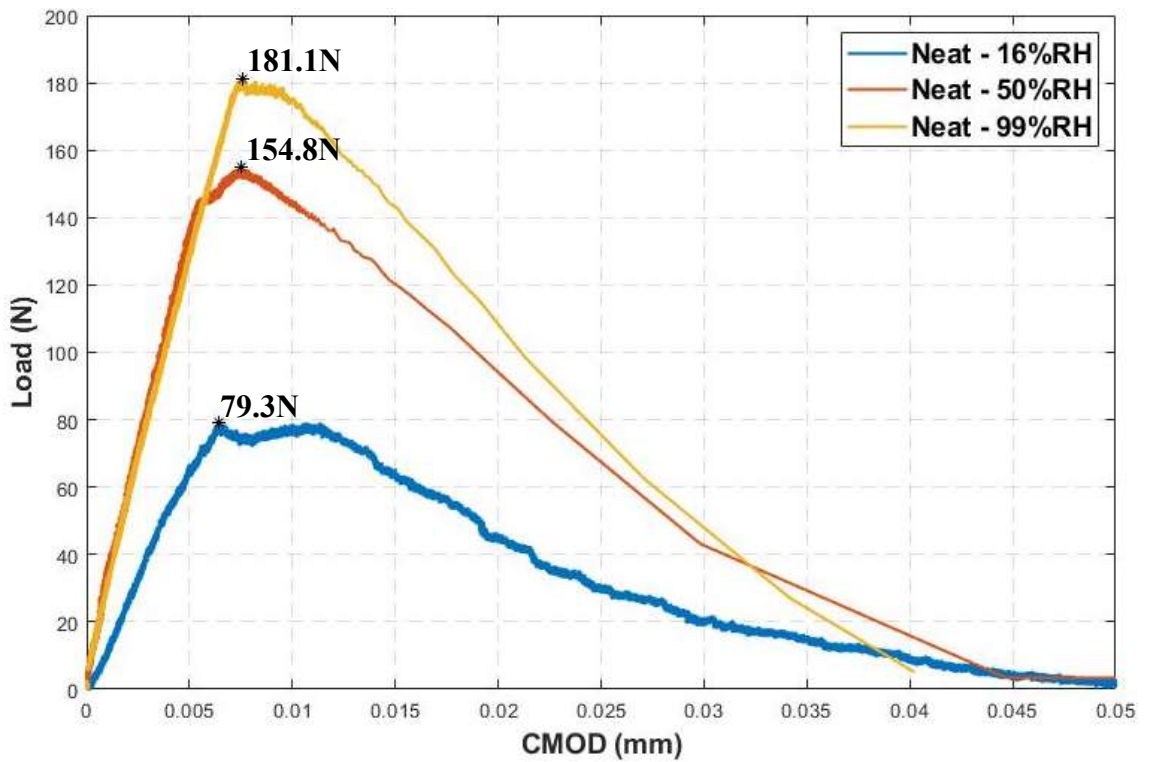


Figure 22. Median load-CMOD curves for the 12-week, neat fracture tests.

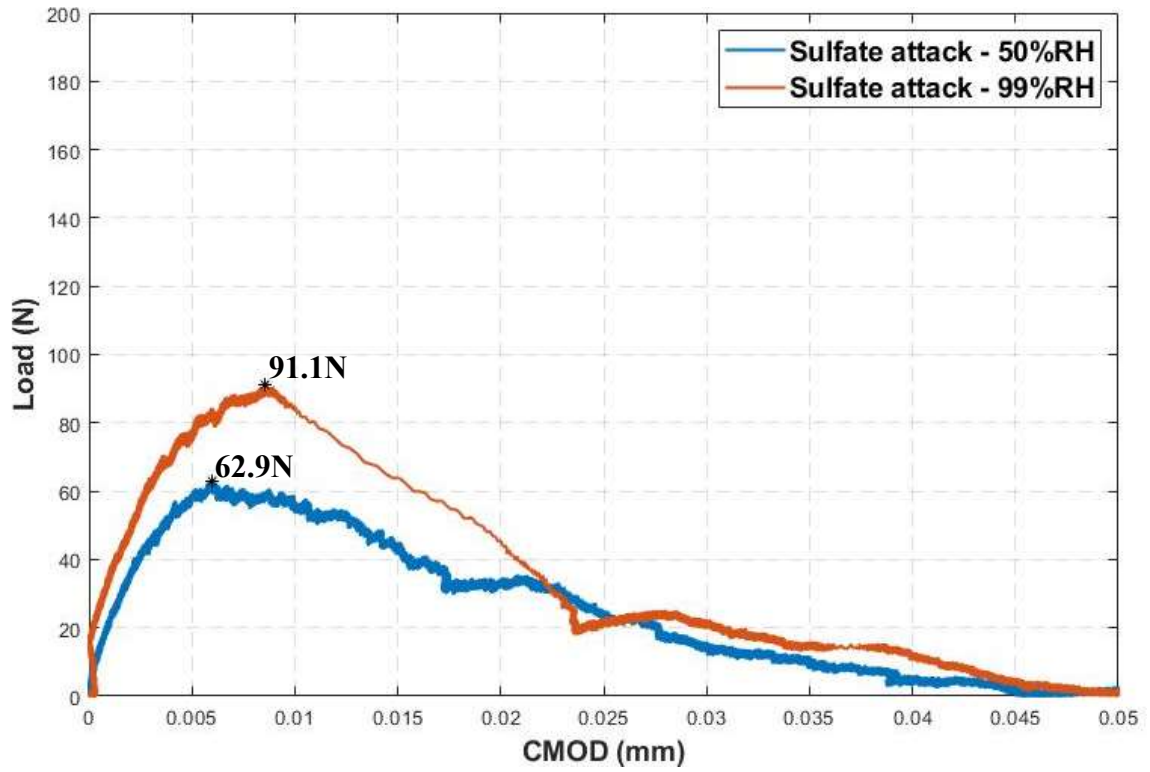


Figure 23. Median load-CMOD curves for the 12-week, sulfate attack fracture tests.

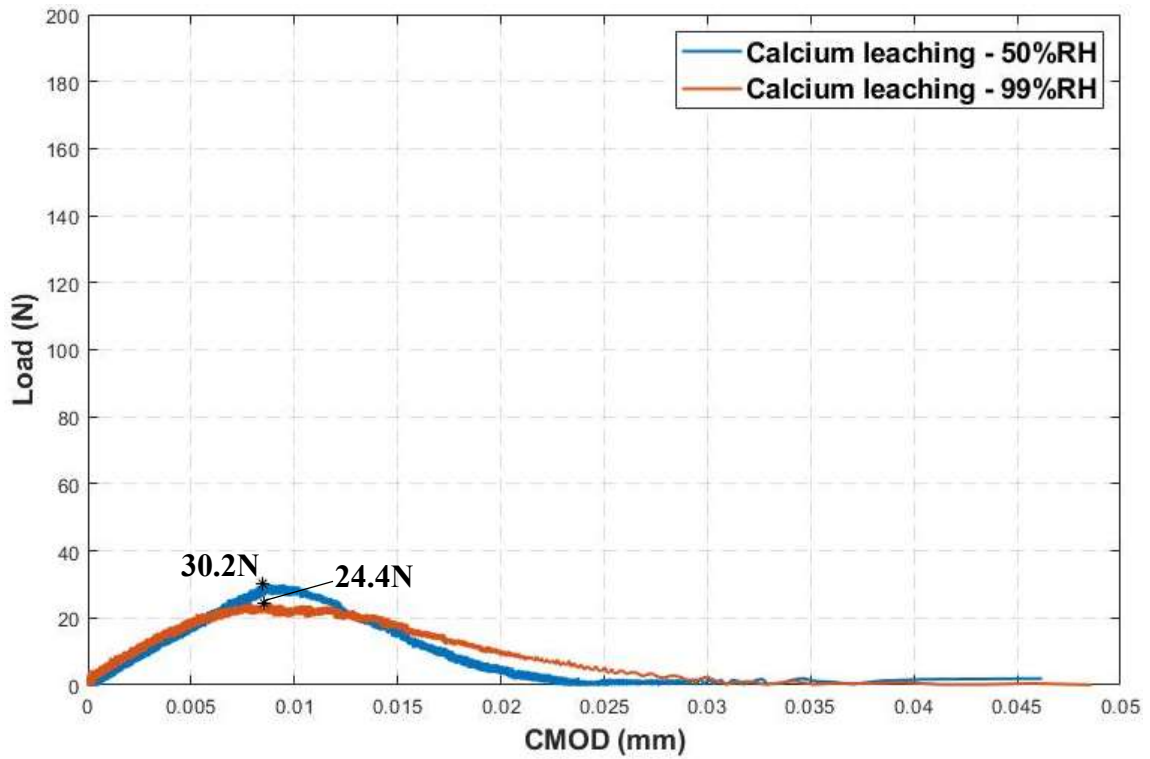


Figure 24. Median load-CMOD curves for the 12-week, calcium leached fracture tests.

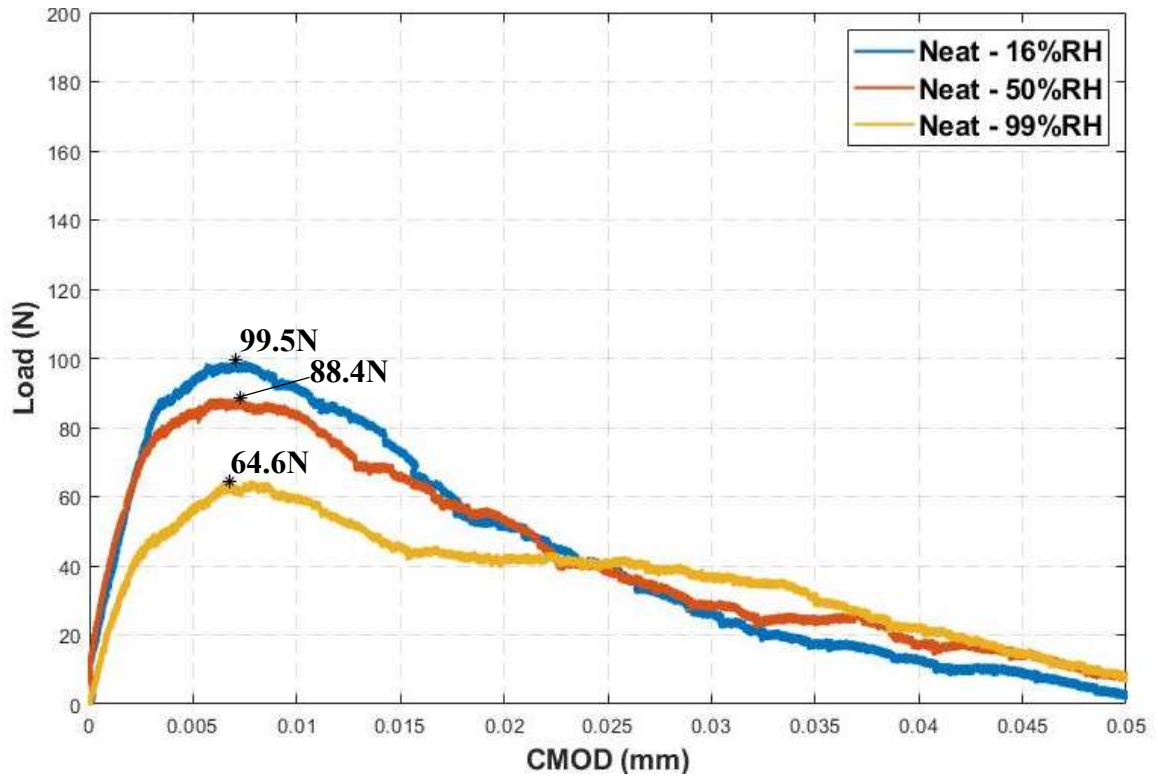


Figure 25. Median load-CMOD curves for the 24-week, neat fracture tests.

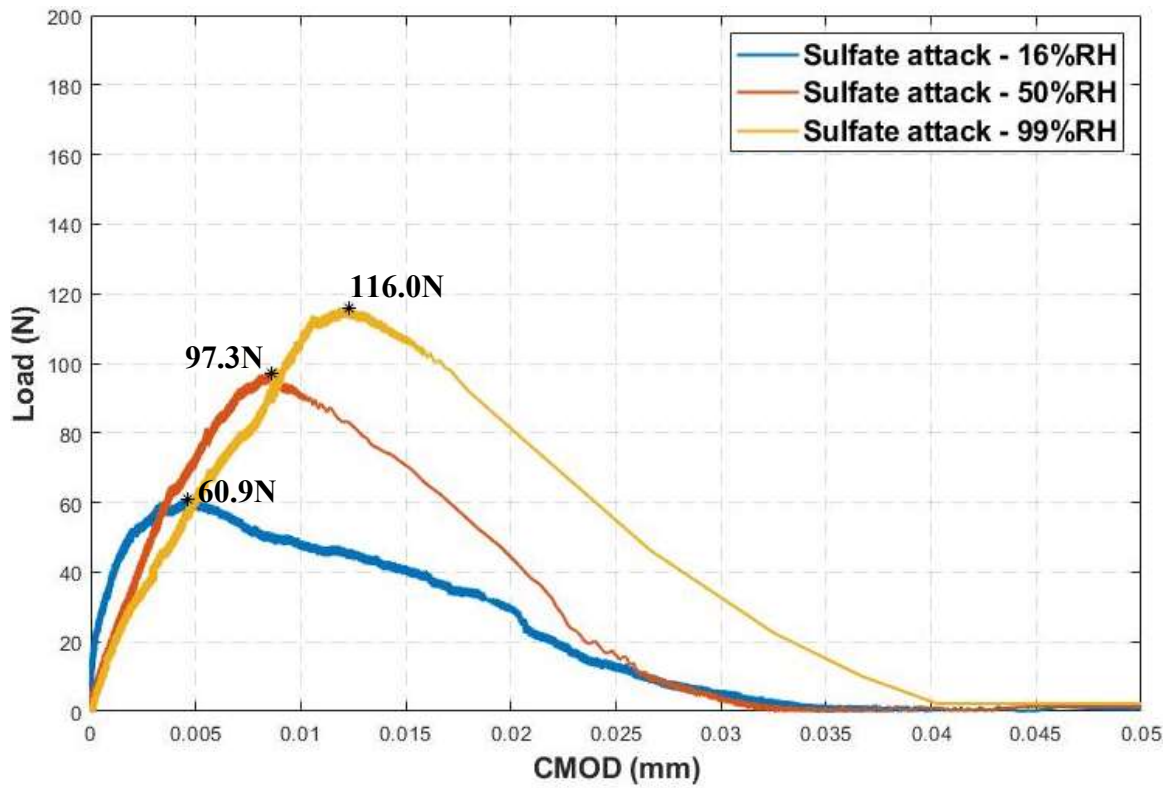


Figure 26. Median load-CMOD curves for the 24-week, sulfate attack fracture tests.

Using the methods outlined in Section 3 for analysis and the Matlab code shown in Appendix A, apparent mechanical and fracture properties were derived from test results as presented in Figures 27-38. The QBFM: effective crack modulus method was utilized by equating the elastic modulus of the unnotched specimen to the elastic modulus at the critical crack length using secant compliance at the maximum load. Figures 27-29 show the summary data for the 12-week tests performed. Across the 99%RH exposure in these figures, the stiffness, modulus of rupture, and the fracture energy are all greatly lessened in both degradation exposures. Figures 30-32 show the summary data for the 24-week tests performed. Figures 33-35 show the summary data for the 1-week, 12-week, and 24-week neat tests performed for context of how the properties have changed over time. Figures 36-38 show the summary data for the 12-week and 24-week sulfate attack tests performed for context of how the properties have changed over time.

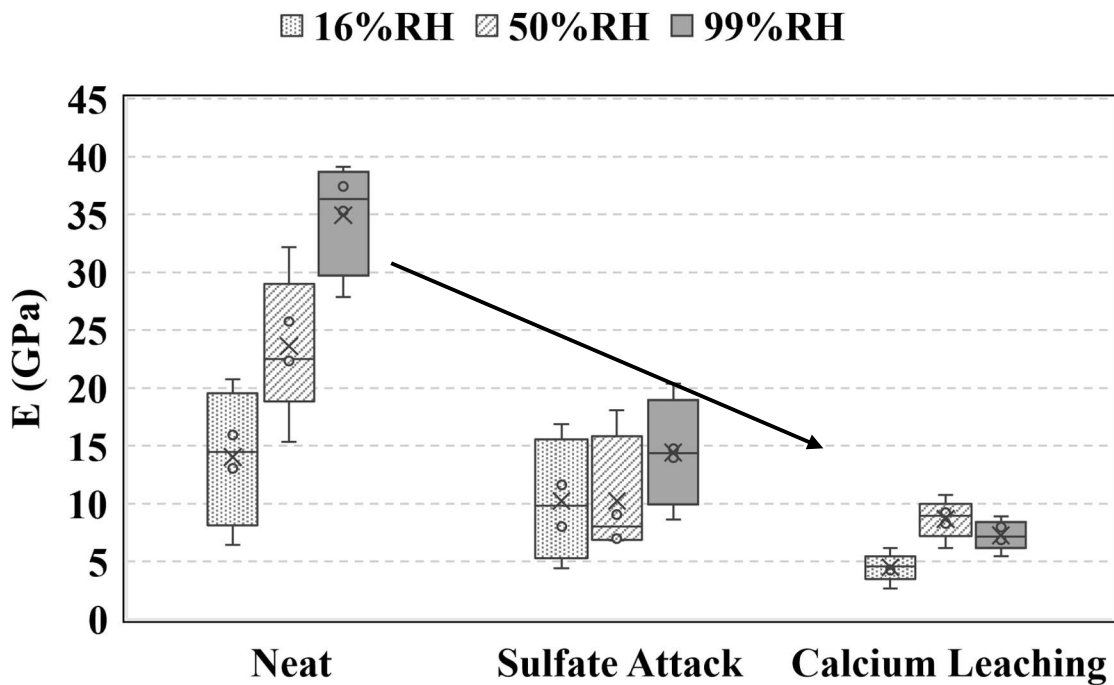


Figure 27. Summary data for modulus of elasticity of unnotched specimens for 12-week exposure. Arrow shows downward trend in 99%RH exposures across degradation modes.

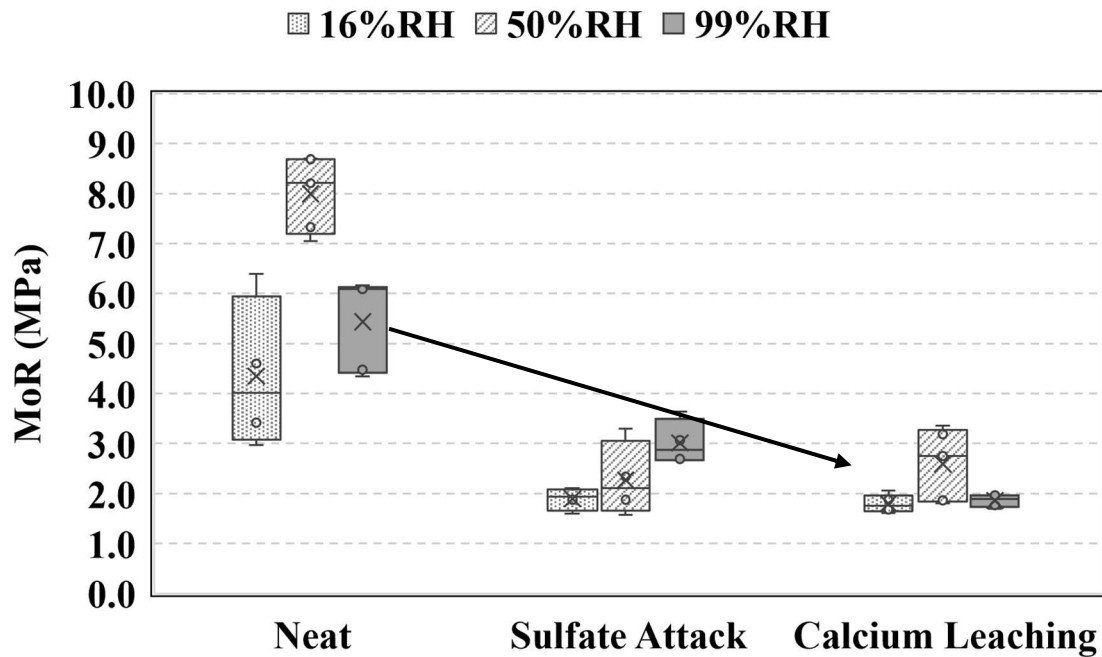


Figure 28. Summary data for the modulus of rupture of unnotched specimens for 12-week exposure. Arrow shows downward trend in 99%RH exposures across degradation modes.

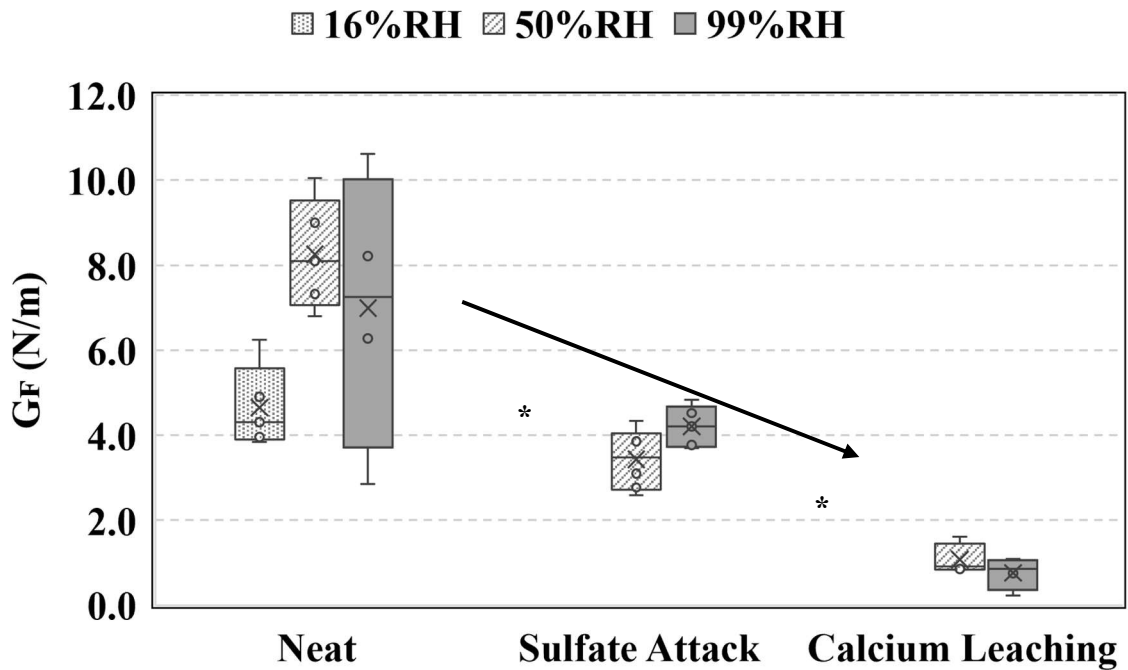


Figure 29. Summary data for the fracture energy of notched specimens for the 12-week exposure. Arrow shows downward trend in 99%RH exposures across degradation modes.

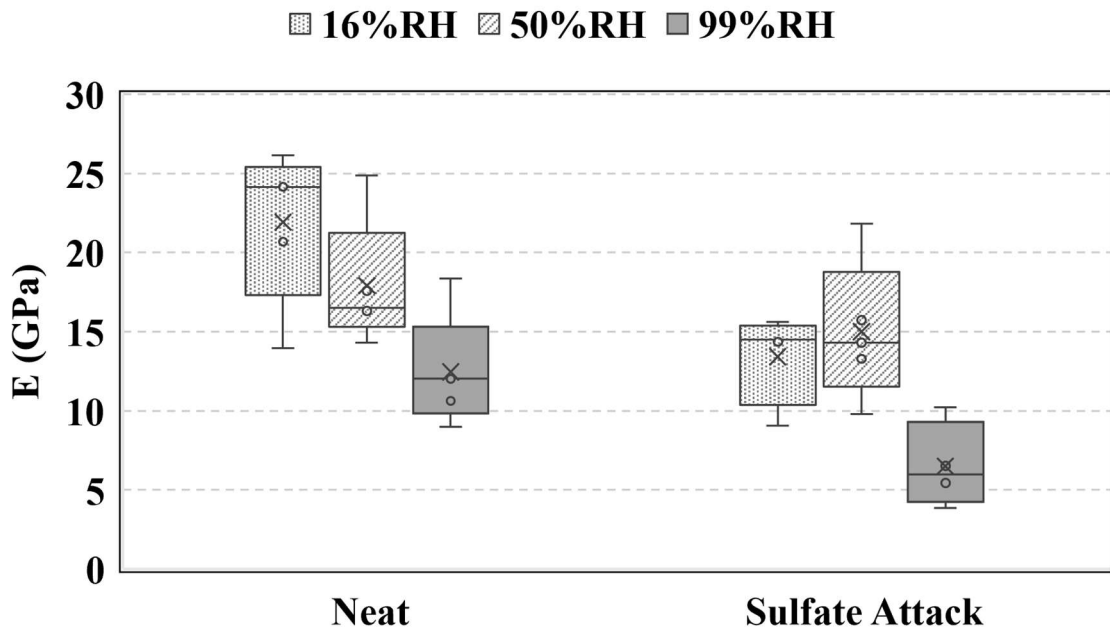


Figure 30. Summary data for modulus of elasticity of unnotched specimens for 24-week exposure.

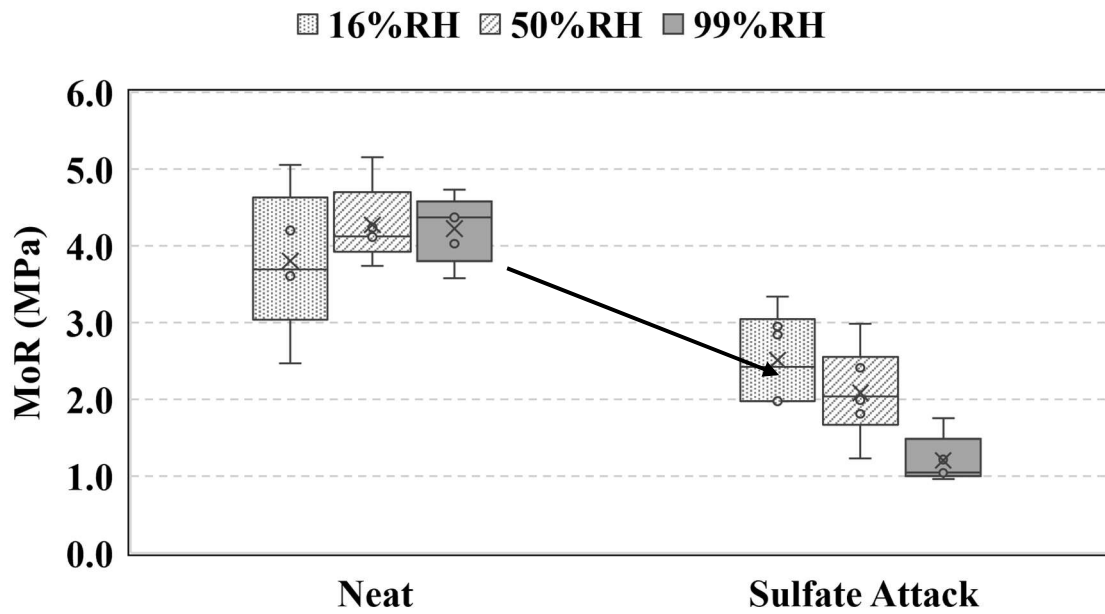


Figure 31. Summary data for the modulus of rupture of unnotched specimens for 24-week exposure. Arrow shows downward trend in 99%RH exposures across degradation modes.

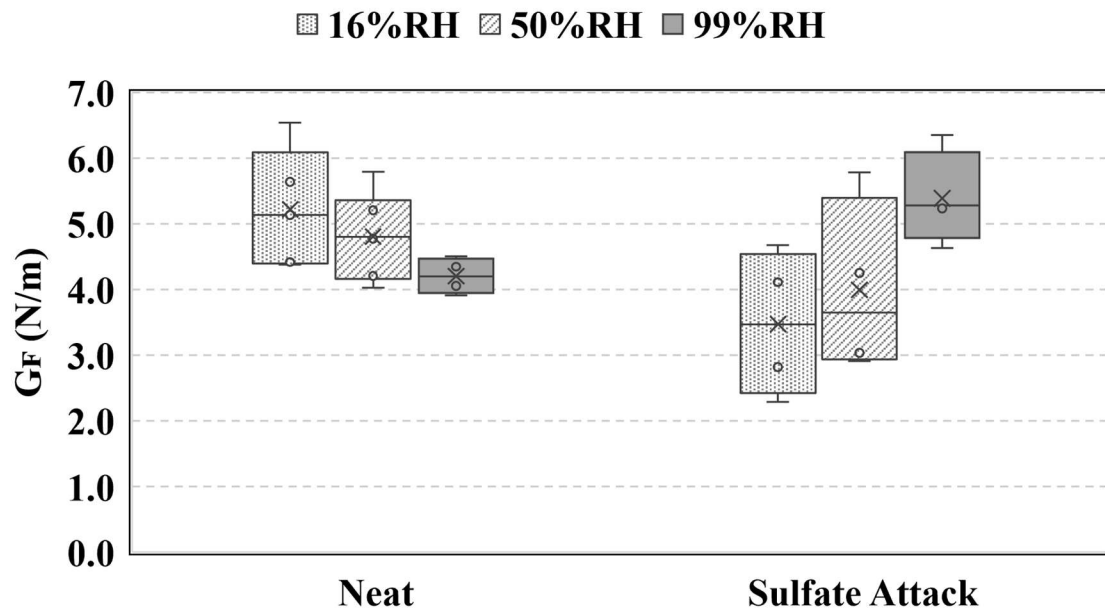


Figure 32. Summary data for the fracture energy of notched specimens for the 24-week exposure.

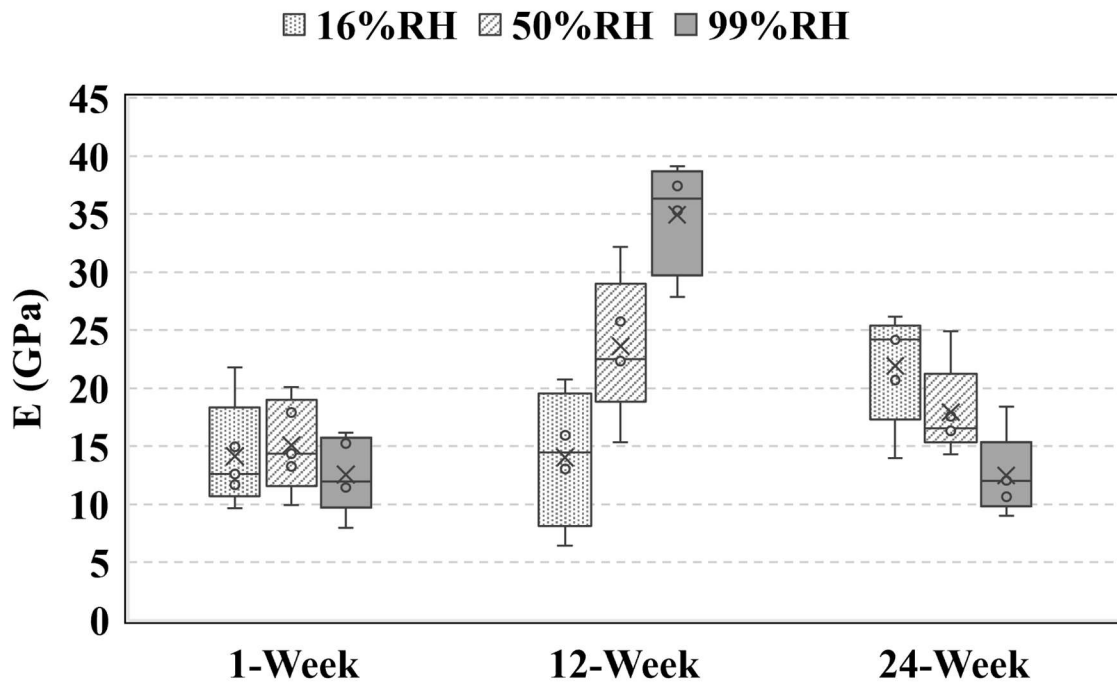


Figure 33. Summary data of modulus of elasticity for neat, unnotched tests performed at different exposure times.

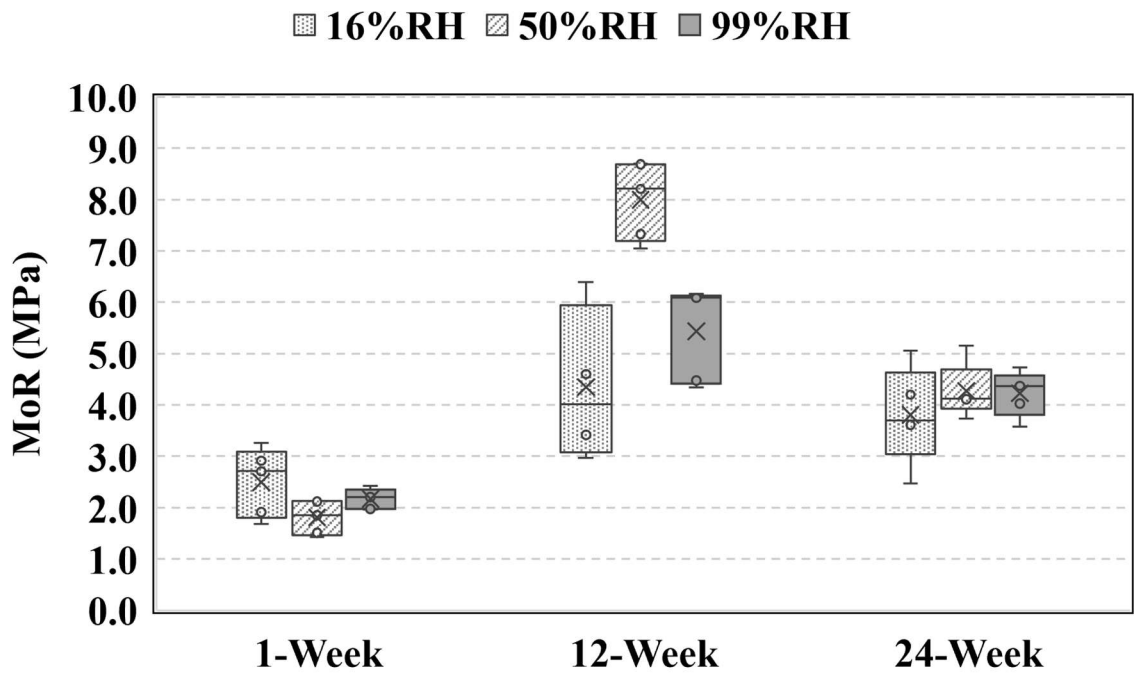


Figure 34. Summary data of modulus of rupture for neat, unnotched tests performed at different exposure times.

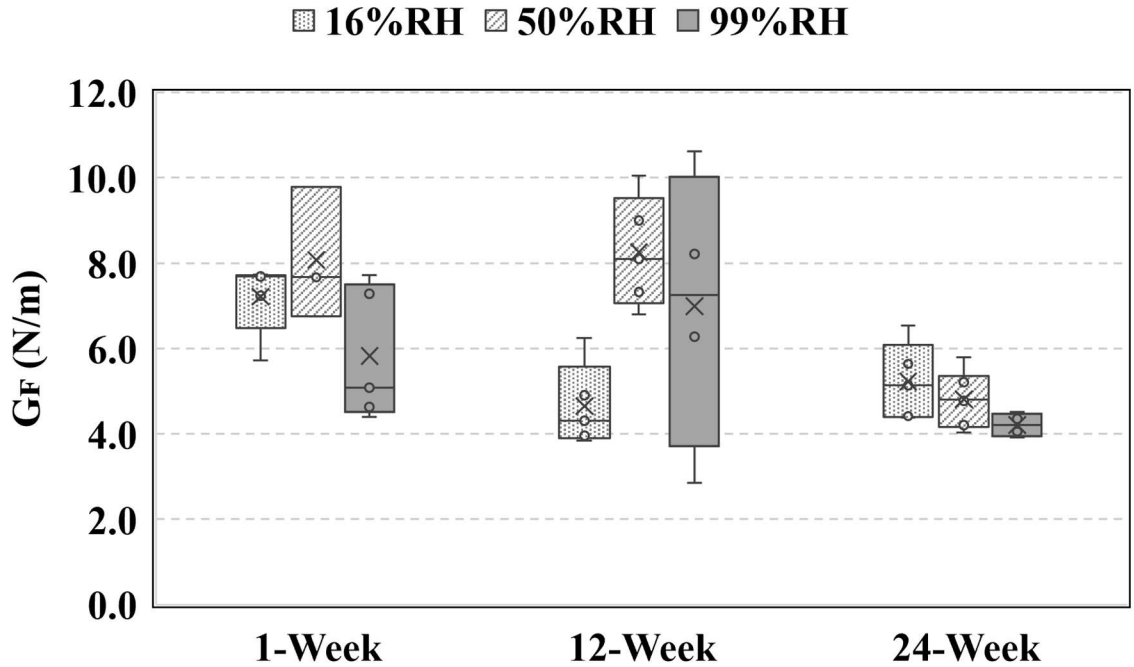


Figure 35. Summary data of fracture energy for neat, notched tests performed at different exposure times.

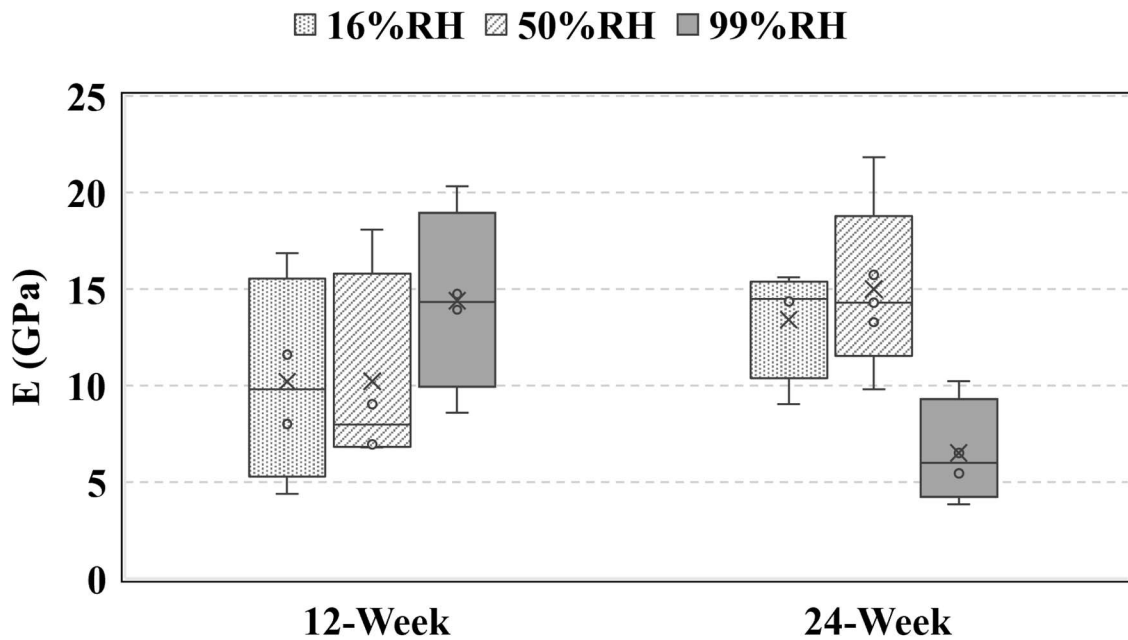


Figure 36. Summary data of modulus of elasticity for unnotched tests performed on sulfate attack samples after different exposure times.

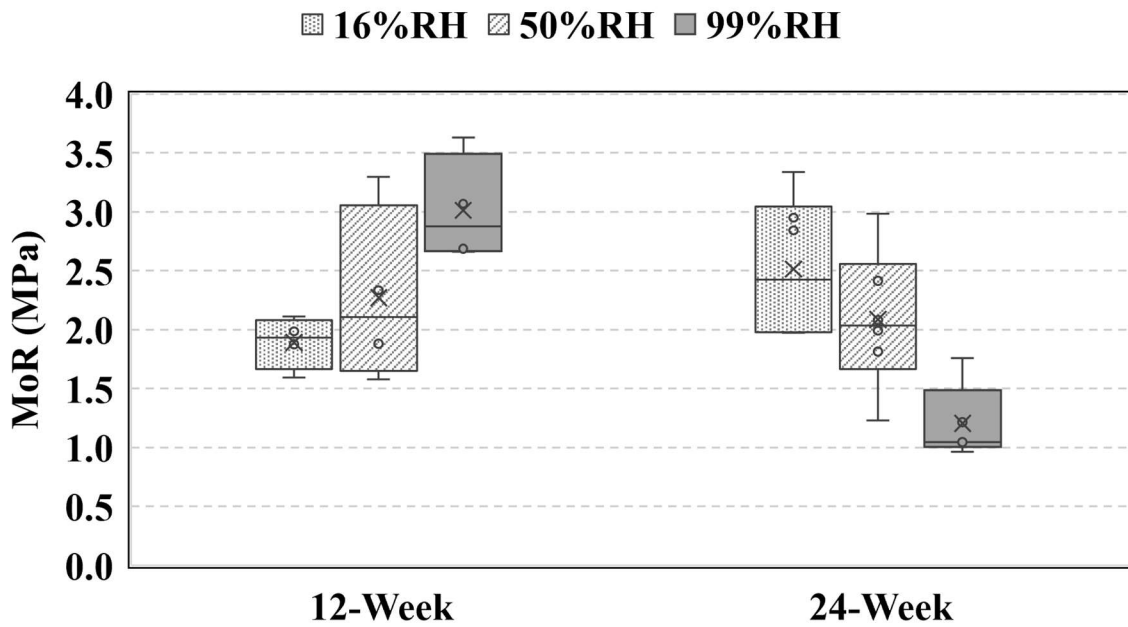
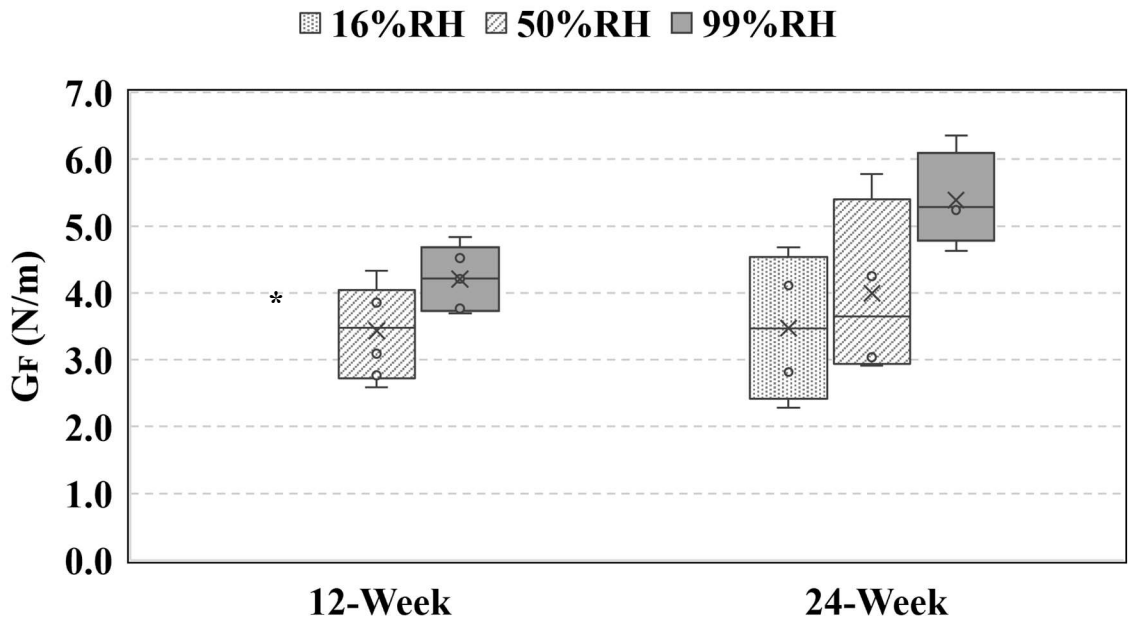


Figure 37. Summary data of modulus of rupture for unnotched tests performed on sulfate attack samples after different exposure times.



**Removed or not tested.*

Figure 38. Summary data of fracture energy for notched tests performed on sulfate attack samples after different exposure times.

Tables 6-8 show the found mean and standard deviation for the apparent G_{IC} (critical elastic energy release rate) and J_{IC} (critical plastic energy release rate) values. Table 7, of the 12-week data, shows a mostly consistent decrease in these two properties between the degradation modes – the neat samples had the highest values, the sulfate attack samples had the second highest, and the calcium leached samples exhibited the lowest values for both G_{IC} and J_{IC} . The 24-week results do not reflect the same downward trend from neat to degraded samples. It is important to note that J_{IC} may be inconsistent as it reflects plastic behavior. Cement paste, as observed in this study was a very brittle, linear elastic material with little to no plastic behavior.

Table 6. Summary data for 1-week, neat fracture properties, G_{IC} and J_{IC} .

1-Week	G_{IC} (N/m)			J_{IC} (N/m)		
	16%RH	50%RH	99%RH	16%RH	50%RH	99%RH
Neat	24.9±7.9	23.3±16.1	9.2±2.2	4.9±1.9	4.7±1.6	2.9±0.7

Table 7. Summary data for 12-week fracture properties, G_{IC} and J_{IC} .

12-Week	G_{IC} (N/m)			J_{IC} (N/m)		
	16%RH	50%RH	99%RH	16%RH	50%RH	99%RH
Neat	11.1±7.7	13.5±5.9	11.6±6.5	1.4±2.6	2.6±1.2	5.9±2.1
Sulfate Attack	*	6.2±3.5	7.2±3.8	*	2.5±1.0	2.6±1.4
Calcium Leaching	*	1.2±0.7	3.6±3.5	*	0.6±0.7	0.2±0.4

*Removed or not tested.

Table 8. Summary data for 24-week fracture properties, G_{IC} and J_{IC} .

24-Week	G_{IC} (N/m)			J_{IC} (N/m)		
	16%RH	50%RH	99%RH	16%RH	50%RH	99%RH
Neat	6.0±2.5	7.1±4.5	2.9±1.7	3.1±0.8	2.6±0.8	1.3±0.8
Sulfate Attack	5.9±2.9	5.5±3.1	11.8±6.2	1.9±0.8	3.4±0.8	5.4±1.9

To complement the analysis discussed so far, t-tests were performed to determine if tests of interest are statistically significant to each other through p-values. The results of this are outlined in Tables 9-14. “Statistically significant” is considered to have a p-value less than 0.05 (95% confidence interval), these cells are highlighted in grey. Tables 9-11 show the 16%RH and 50%RH condition results compared to the 99%RH condition results. For E , MoR , and G_F , a majority (74%) of comparisons are not statistically significant. This is likely due to the relatively short period of time that the samples are exposed to relative humidity. It does not appear that short-term exposure to various relative humidities makes a notable difference in observed test results.

Table 9. P-values for modulus of elasticity comparisons across relative humidity exposures.

	16%RH & 99%RH	50%RH & 99%RH
1-Week Neat	0.551	0.302
12-Week Neat	0.002	0.018
12-Week Sulfate Attack	0.462	0.464
12-Week Calcium Leaching	0.009	0.173
24-Week Neat	0.009	0.054
24-Week Sulfate Attack	0.147	0.076

Table 10. P-values for modulus of rupture comparisons across relative humidity exposures.

	16%RH & 99%RH	50%RH & 99%RH
1-Week Neat	0.348	0.078
12-Week Neat	0.271	0.002
12-Week Sulfate Attack	0.009	0.153
12-Week Calcium Leaching	0.539	0.085
24-Week Neat	0.404	0.877
24-Week Sulfate Attack	0.002	0.014

Table 11. P-values for G_F comparisons across relative humidity exposures.

	16%RH & 99%RH	50%RH & 99%RH
1-Week Neat	0.129	0.113
12-Week Neat	0.252	0.511
12-Week Sulfate Attack	*	0.063
12-Week Calcium Leaching	*	0.277
24-Week Neat	0.064	0.082
24-Week Sulfate Attack	0.033	0.089

*Removed or not tested.

To better understand the sample's response to exposure over time, t-tests were also performed within degradation modes over time. P-values for the neat tests are outlined in Tables 12-14. Again, statistically significant values are shaded grey.

For the neat tests, it can be observed that about half of the results are statistically significant when compared with each other over time. Since the neat samples' properties plateau over time, it is expected that 1-week tests exhibit statistically different properties than the 12-week, while the 12- and 24-week properties should be more similar. This expectation is generally true when comparing the 1-week results with the 12-week results (56% of results are statistically significant), but not when comparing the 12- and 24-week

results (44% of results are statistically significant). This could be due to the inherent sensitivity of cement paste in handling and testing and could require re-evaluation.

Table 12. P-values for modulus of elasticity comparisons for neat tests performed, across exposure times, within humidity exposures.

	16%RH	50%RH	99%RH
1-Week & 12-Week	0.978	0.036	0.001
12-Week & 24-Week	0.078	0.128	0.000

Table 13. P-values for modulus of rupture comparisons for neat tests performed, across exposure times, within humidity exposures.

	16%RH	50%RH	99%RH
1-Week & 12-Week	0.089	0.000	0.001
12-Week & 24-Week	0.564	0.000	0.042

Table 14. P-values for G_F comparisons for neat tests performed, across exposure times, within humidity exposures.

	16%RH	50%RH	99%RH
1-Week & 12-Week	0.002	0.874	0.547
12-Week & 24-Week	0.366	0.002	0.188

The p-values comparing the 12- and 24-week sulfate attack exposure times are outlined in Tables 15-17. Generally, the properties are not statistically significant across the two exposure times. This could be explained by the mechanism behind sulfate attack and observations made by previous studies. Recall that sulfate attack leads to the expansive formation of ettringite and that this can simultaneously fill and cause new pores due to the expansive stresses. The samples considered in this study were exposed for 12-weeks (84 days) and 24-weeks (168 days). With previous studies (as discussed in Section 2) exhibiting that sulfate attack can take long periods of time (up to 270 days) before noticeably impacting the macroscale properties, it is reasonable that this explains the 12- and 24-week results appearing to not be significantly different [22].

Table 15. P-values for modulus of elasticity comparisons for sulfate attack tests performed, across exposure times, within humidity exposures.

	16%RH	50%RH	99%RH
12-Week & 24-Week	0.541	0.345	0.137

Table 16. P-values for modulus of rupture comparisons for sulfate attack tests performed, across exposure times, within humidity exposures.

	16%RH	50%RH	99%RH
12-Week & 24-Week	0.056	0.692	0.001

Table 17. P-values for G_F comparisons for sulfate attack tests performed, across exposure times, within humidity exposures.

	16%RH	50%RH	99%RH
12-Week & 24-Week	*	0.481	0.036

*Removed or not tested.

4.2. Leached Depth

The leached depth analysis was performed as outlined in Section 3. The leached depth analysis was completed for each degradation mode at the 12-week exposure time. The results of the fluorescence tests are shown in Figure 32. The fluorescent solution turns deep purple/pink when exposed to a higher pH and remains colorless when exposed to lower pH. Again, cement paste is expected to have a pH ~12. It is expected that degraded samples reflect the pH of the solution they were degraded in due to equilibrium. The sulfate attack degradation bath has a neat pH ~9 that increases to ~12 when samples are placed in it. The calcium leaching bath has a neat pH ~5 that increases to ~9 after equilibrium with samples.

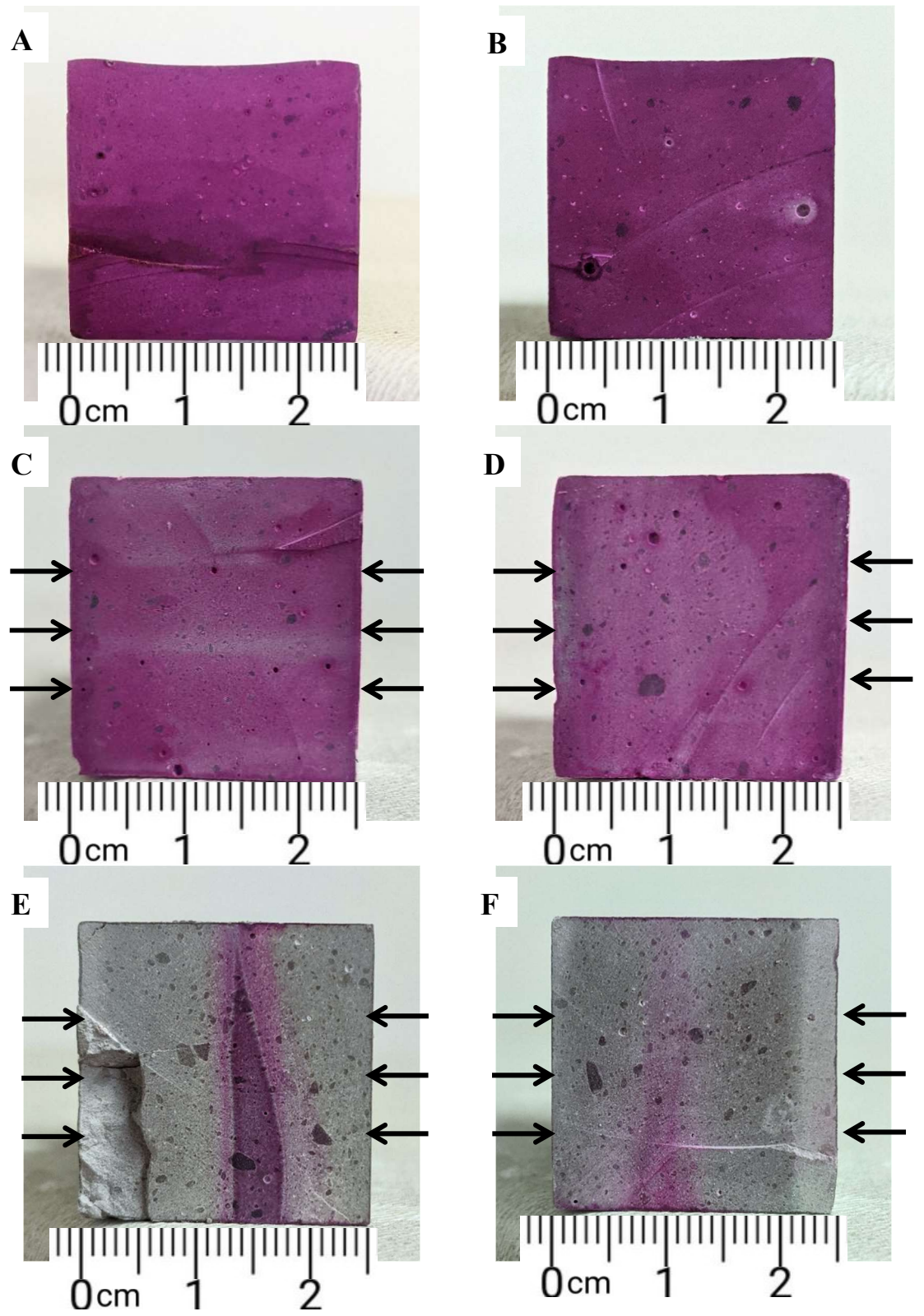


Figure 39. Images of fluorescence exposure to cross sections of 12-week samples with scale. Arrows show the degradation plane. A and B are the neat samples. C and D are the sulfate attack samples. E and F are the calcium leached samples.

The neat samples, shown in Figure 39(A) and (B), exhibit a deep shade of purple, which is expected as the pH of neat cement is high. The sulfate attack samples (C & D) have no clear degradation depth but do show a slightly lighter shade of purple. The calcium leached samples (E & F) show severe degradation with faint, thin strips of higher pH near their center. In Figure 39(E), only about 5mm is not fully leached. Figure 39(F) is nearly fully leached. It was observed that between the two calcium leached samples, the average leached depth (measured from the edge to the center of the cross section) was 9.3mm.

The results of the TGA tests performed on the 12-week exposure samples reflected the presence of main binding compounds to different extents. Figures 40-48 show typical results of the observed depths (edge, mid-depth, and center) for the 12-week exposure samples. The peaks observed will be assessed as they relate to the windows discussed in Section 2. The scale for all axes was held constant for all figures to better compare. The neat samples lost ~25% of their initial weight through the course of the test. The sulfate attack samples lost slightly more, ~27% of their initial weight. The calcium leached samples lost ~35% of their starting weight.

For the neat results (Figures 40-42), all depths observed peaks ~100°C (where the evaporable water, ettringite, and gypsum are decomposed) and between 400-500°C (where CH is dehydroxylated). The minor peak observed just below 400°C can be attributed to carboaluminate phases decomposing. Some tests observed a smaller peak between 650-900°C, this is where decarbonation of calcium carbonate occurs [75]. The major peaks are labeled in Figure 40.

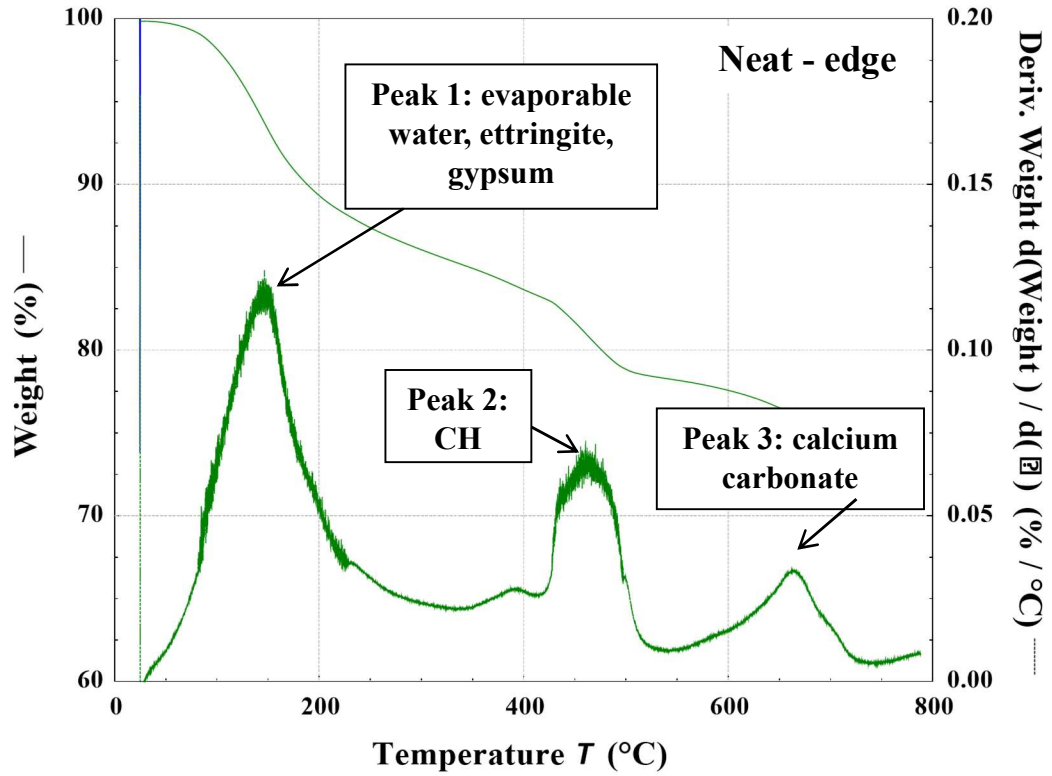


Figure 40. Typical TGA results with derivative weight for 12-week, neat sample at edge of degradation plane (0-5mm or 20-25mm).

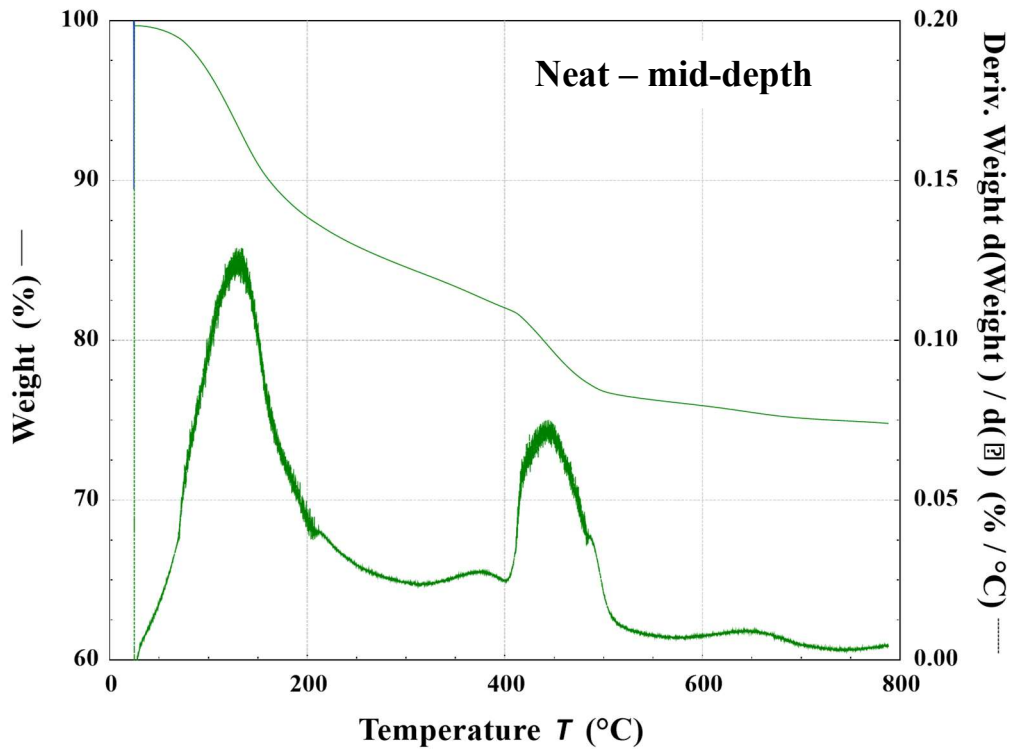


Figure 41. Typical TGA results with derivative weight for 12-week, neat sample at mid-depth of degradation plane (5-10mm or 15-20mm).

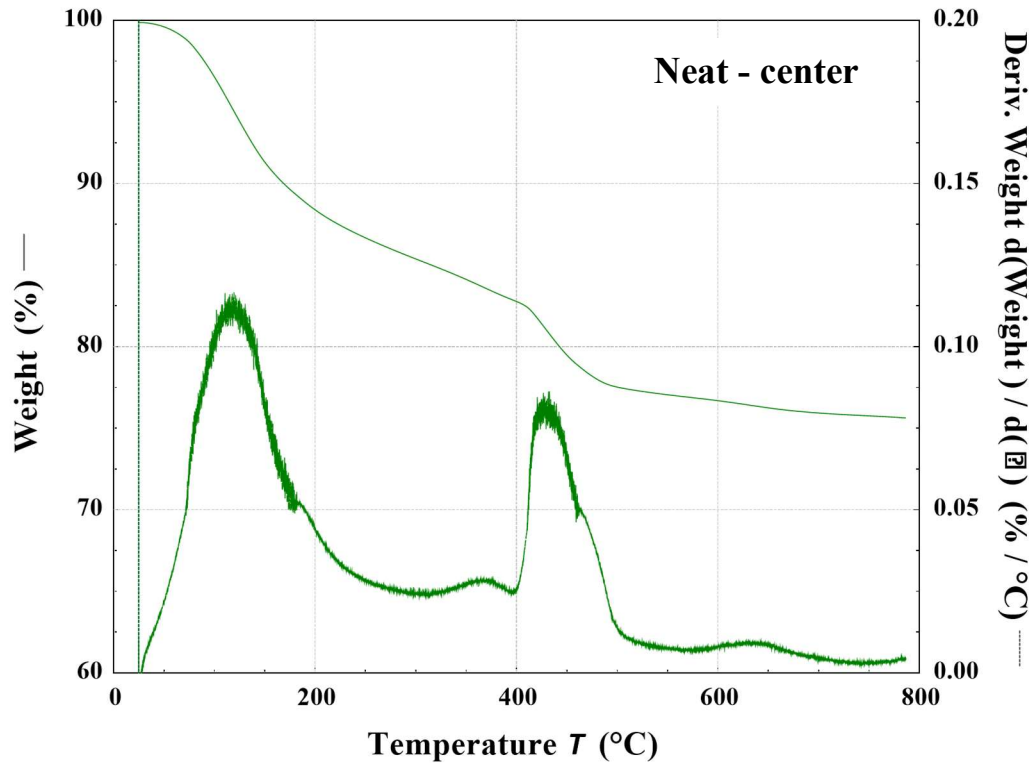


Figure 42. Typical TGA results with derivative weight for 12-week, neat sample at center of degradation plane (10-15mm).

The TGA results for the 12-week, sulfate attack samples are shown in Figures 43-45. It can be observed that, in comparison with the neat, the sulfate attack samples have sharper, more intense initial peak $\sim 100^{\circ}\text{C}$. This can be explained by the mechanism behind the sulfate attack; sulfate attack leads to new formation of ettringite, which is the compound lost at this temperature. This phenomenon is most realized at the edge of the sample as shown in Figure 43. The mid-depth and center of the sulfate attack samples are very similar to each other and do not have as intense of a first peak. Besides this first peak, the sulfate attack curves are very similar to the neat samples, with peaks reflecting the presence of carboaluminate phases ($\sim 375^{\circ}\text{C}$), CH ($\sim 450^{\circ}\text{C}$), and calcium carbonate ($\sim 650^{\circ}\text{C}$). Again, major peaks are labeled on Figure 43.

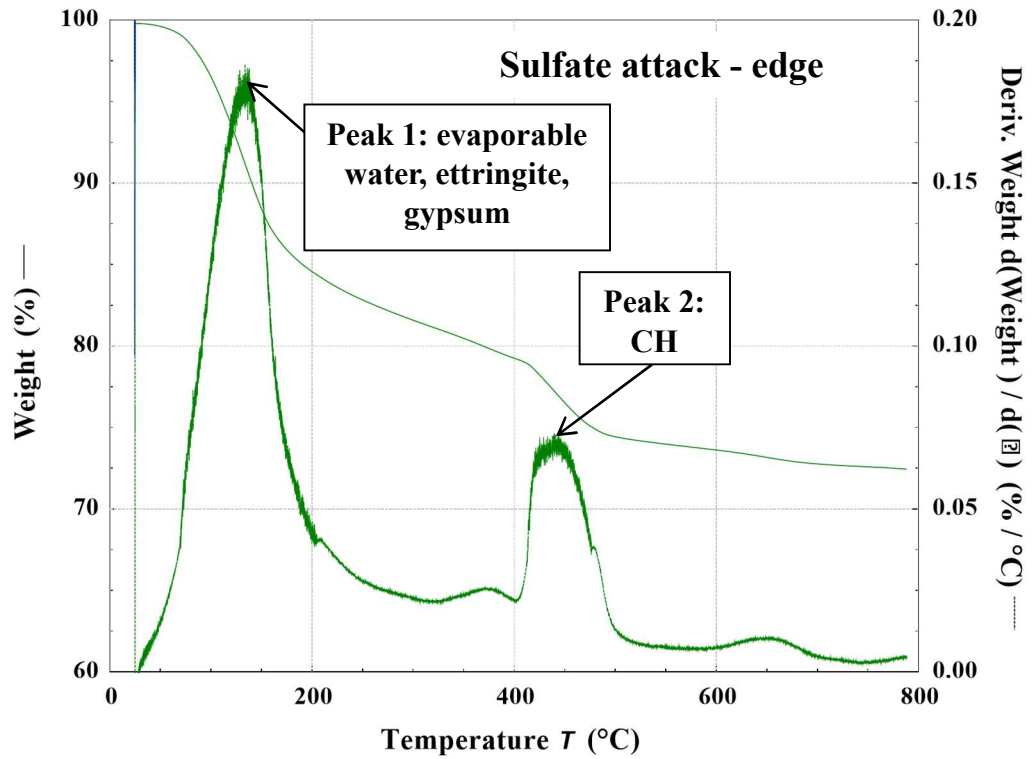


Figure 43. Typical TGA results with derivative weight for 12-week, sulfate attack sample at edge of degradation plane (0-5mm or 20-25mm).

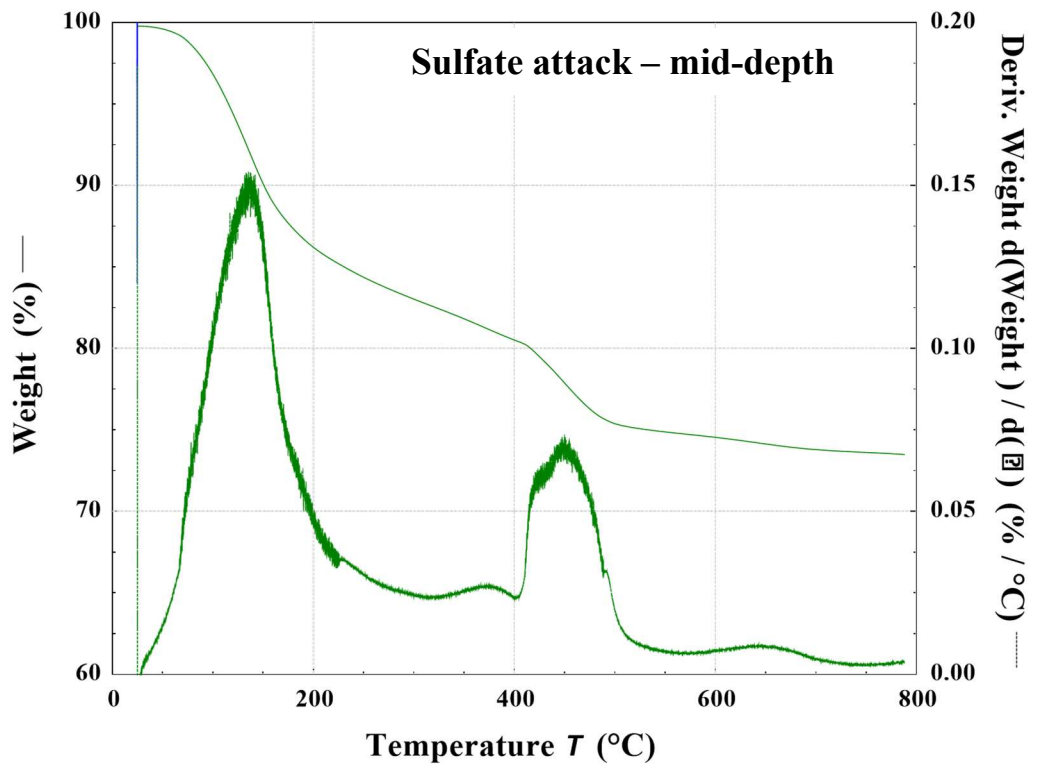


Figure 44. Typical TGA results with derivative weight for 12-week, sulfate attack sample at mid-depth of degradation plane (5-10mm or 15-20mm).

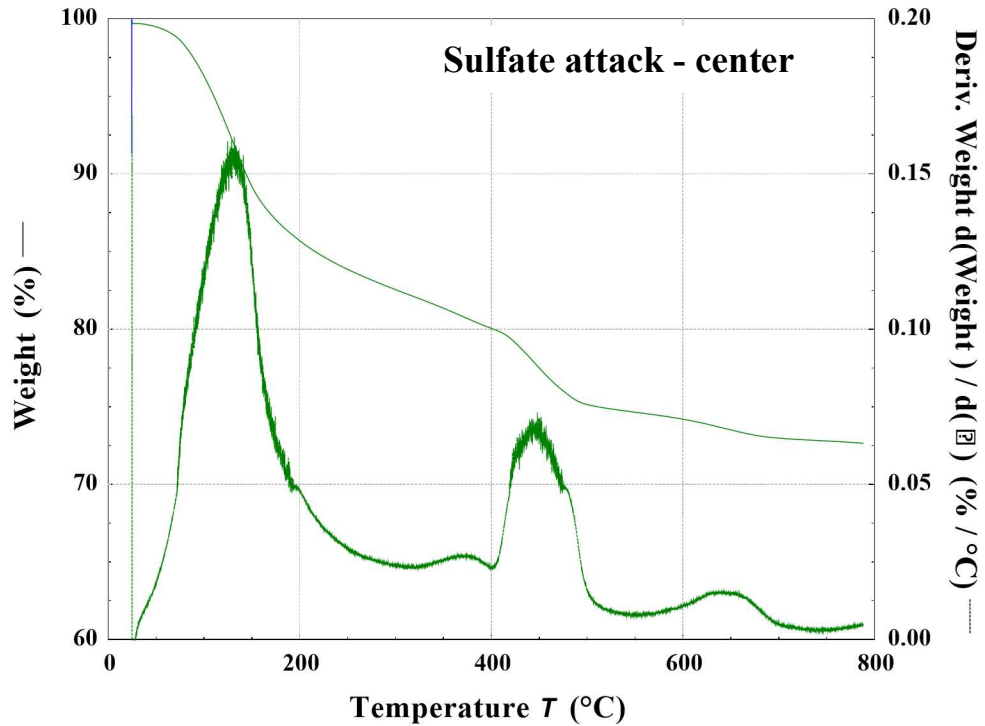


Figure 45. Typical TGA results with derivative weight for 12-week, sulfate attack sample at center of degradation plane (10-15mm).

The typical TGA results for the 12-week, calcium leached samples are shown in Figures 46-48. Two predominant peaks are observed at each depth (at $\sim 100^{\circ}\text{C}$ and $\sim 475^{\circ}\text{C}$), with a third minor peak just above 300°C . The results from the edge (Figure 39), also exhibit a notable peak at $\sim 675^{\circ}\text{C}$. At first glance, the TGA tests seem to reflect the potential presence of important binding compounds, as with the neat and sulfate attack experiments. This can be explained by the similarity between the decomposition of calcium nitrate (and other leaching products) and the decomposition of binding compounds. As discussed in Section 2, almost all of the windows to consider for leaching products overlap in some way with the windows to consider for undegraded cement paste. For example, CH is dehydroxylated between $400\text{-}500^{\circ}\text{C}$, this overlaps with the decomposition of calcium nitrate between $450\text{-}650^{\circ}\text{C}$ [75]. With the previous observations of severe leached depth and significant loss of stiffness and strength, it is reasonable to attribute these similar

dominant peaks, that seemingly show the presence of binding compounds, to actually reflect the presence of calcium nitrate in the leached matrix.

As discussed in Section 2, several factors can influence which leaching reactions govern the leaching process. This can not only vary the temperatures at which compounds (i.e. ammonium nitrate) will dehydrate, but it can also vary if some compounds will show up at all (i.e. pure nitrogen and oxygen) [75]. This means that results will likely fluctuate slightly between calcium leaching studies and explains any minor peaks observed. The minor peak observed at all depths just above 300°C most likely reflects unreacted ammonium nitrate within the matrix dehydrating [75]. The peak observed in the edge sample at ~675°C, can be attributed to the final dissociation of pure nitrogen and oxygen from calcium nitrate's dissociation. Again, major peaks are labeled in Figure 46.

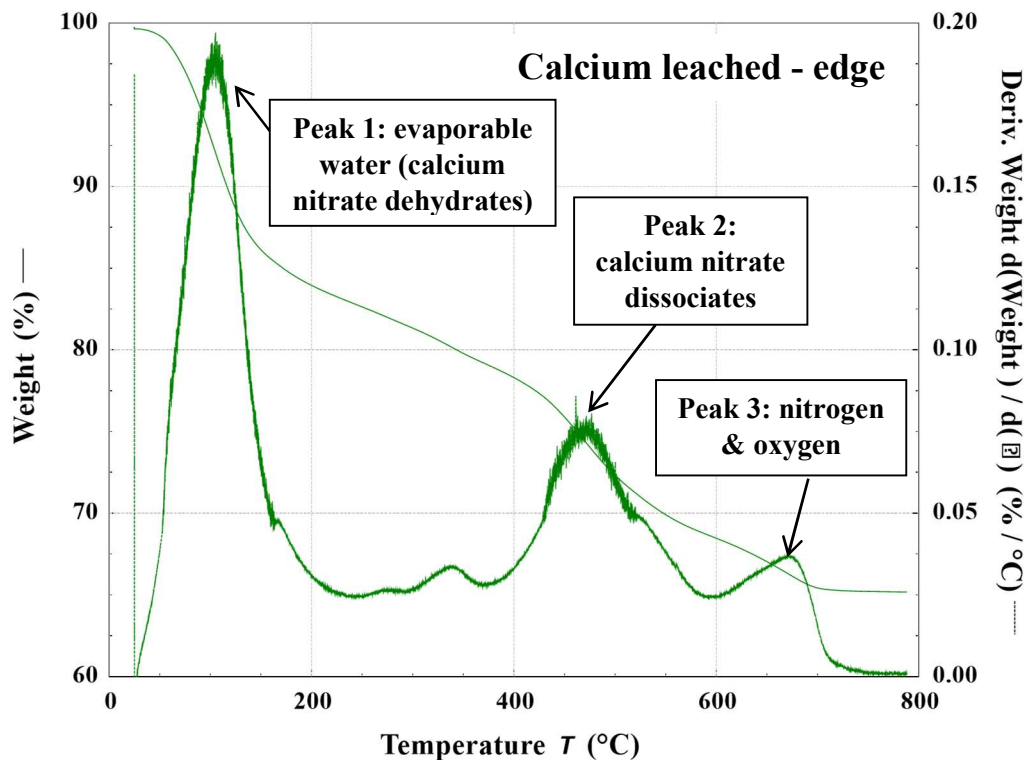


Figure 46. Typical TGA results with derivative weight for 12-week, calcium leached sample at edge of degradation plane (0-5mm or 20-25mm).

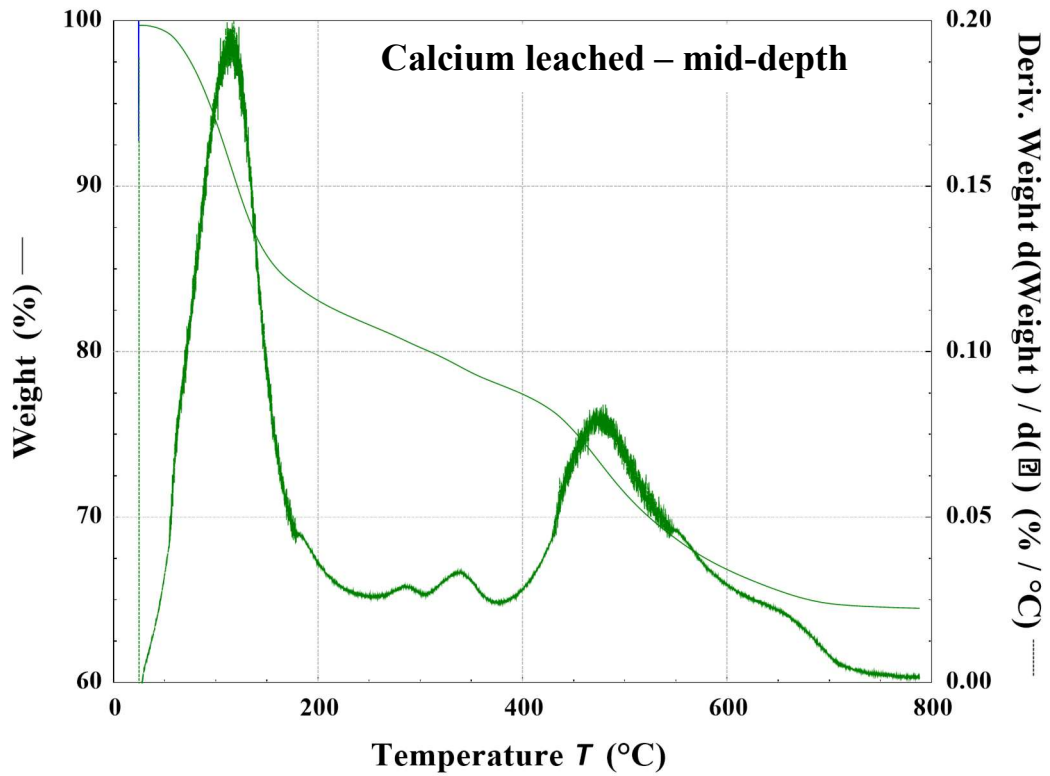


Figure 47. Typical TGA results with derivative weight for 12-week, calcium leached sample at mid-depth of degradation plane (5-10mm or 15-20mm).

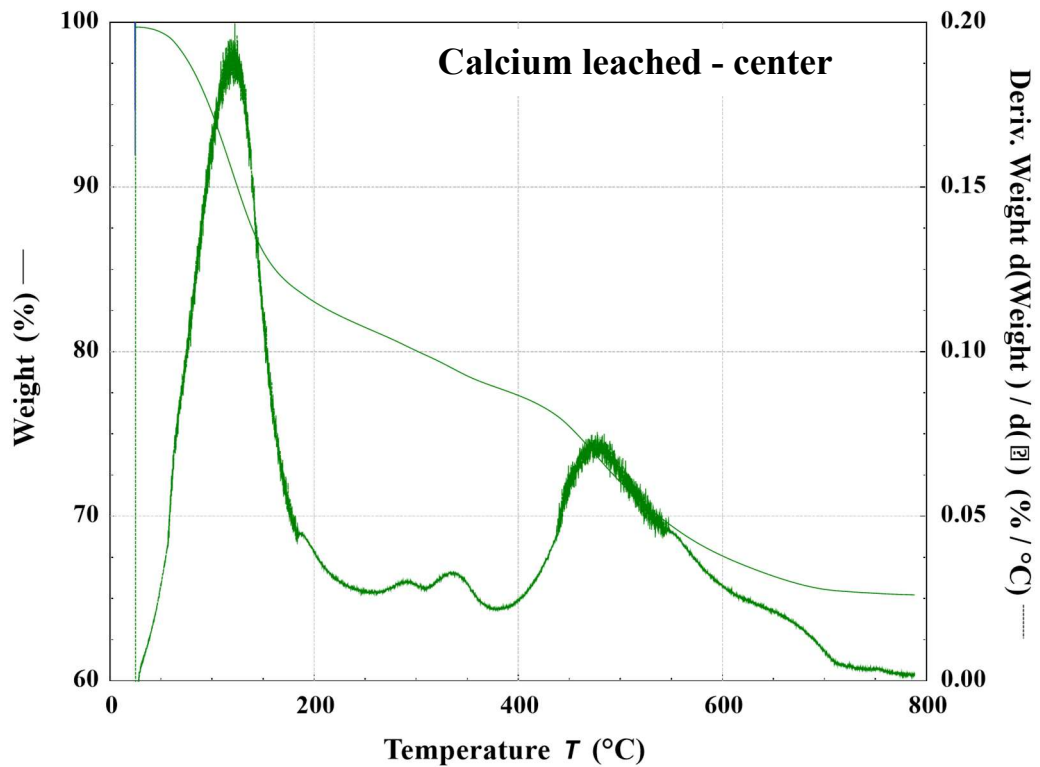


Figure 48. Typical TGA results with derivative weight for 12-week, calcium leached sample at center of degradation plane (10-15mm).

4.3. Damage

Damage was evaluated through several methods. As a baseline, weight and dimensions were monitored as samples degraded. Damage was also evaluated by loss in stiffness and leached depth, as discussed in Section 3. Figure 49 shows the observed density changes as the sample have degraded; the percent values are the percentage of density change since the initial measurements. The neat samples gain some density as time goes on, the sulfate attack samples maintain about the same density, and the calcium leached samples lose a significant amount of density – nearly 19%. This was a large attributing factor to the 24-week and 52-week calcium leached samples being unable to be tested. In addition to losing a large amount of density, the calcium leached samples almost unanimously exhibited visible cracks from degradation at 20 weeks of exposure. A sample of what that looked like is shown in Figure 50.

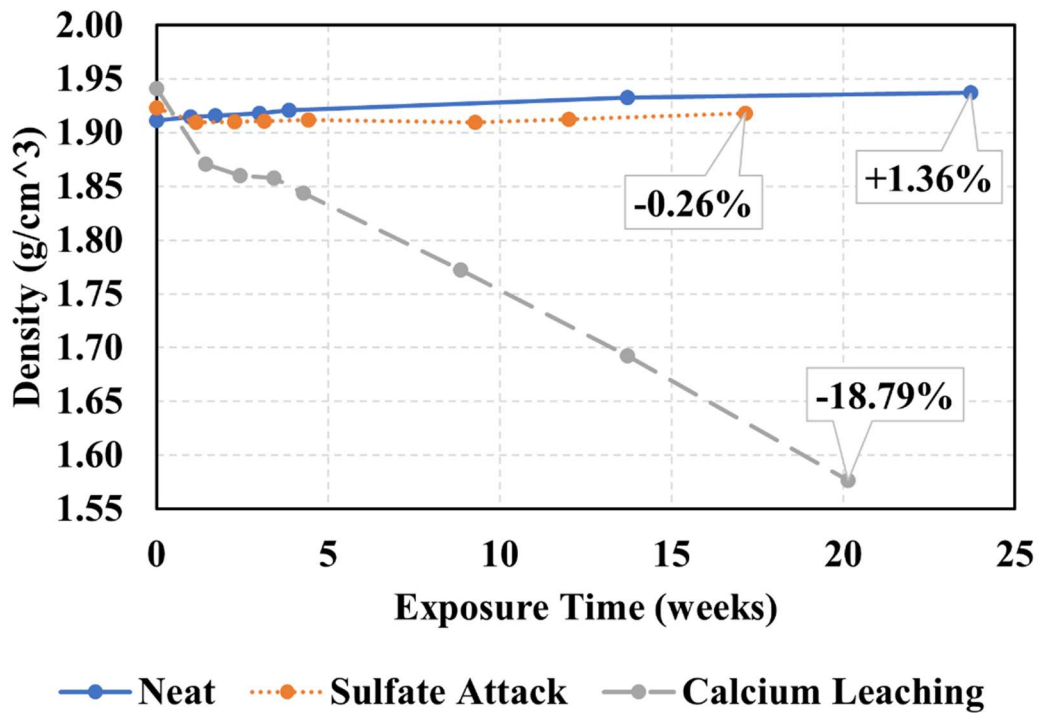


Figure 49. Observed density changes as the samples degrade.



Figure 50. Image of calcium leached sample after 20 weeks of exposure, cracks from degradation are pointed out with arrows.

As discussed in Section 3, damage due to degradation was quantified through change in stiffness and leached depth. Table 18 outlines the average observed values for E from the 99%RH humidity exposures.

Table 18. Average values for modulus of elasticity at 99%RH.

Exposure	Neat E (GPa)	Sulfate Attack E (GPa)	Calcium Leached E (GPa)
12-Week	34.9	14.4	7.2
24-Week	12.5	6.5	-

Using Eq. (2), damage was quantified by comparing the degraded stiffness to the neat stiffness of a sample the same age. Leached depth was only able to be quantified and applied to the 12-week calcium leached samples. It was determined that these samples had an average leached depth of 9.3mm (measured from the edge of degradation plane to the center). This value was applied to Eq. (4) to quantify damage. Table 19 shows the determined values for damage from the tests performed at this point in the study. All damage values are given in a percentage. The 12-week calcium leached samples exhibited the most damage.

Table 19. Damage metrics determined for tests performed.

Exposure	$D_{E,i}$ (%)	$D_{l,i}$ (%)
12-Week Sulfate Attack	58.7	-
12-Week Calcium Leaching	79.3	74.4
24-Week Sulfate Attack	47.8	-

5. CONCLUSION

This thesis examined the influence of calcium leaching and sulfate attack degradation environments as well as change in relative humidity exposure on cement paste fracture. An in-depth literature review was performed on cement degradation to better understand the different degradation modes as well as experimental methods for both degradation and damage quantification.

Cement paste samples were degraded, monitored, tested, and evaluated to observe the effects of degradation environment and relative humidity on cement fracture. Degradation baths were renewed regularly and sample density change was observed over time. Calcium leaching reduced sample density by 18.8% after 20 weeks of exposure. This proved to be so severe that samples exhibited visible cracks from degradation and it was determined that calcium leached samples were unable to be tested beyond 12-weeks of exposure.

Fracture and flexure tests for varying degradation environments and relative humidity were performed to quantify the significance of these environments on fracture toughness of cement. From these tests, both mechanical (E and MoR) and fracture (G_F , G_{IC} , and J_{IC}) properties were able to be determined.

Statistical tests were applied to the apparent values to better understand their significance to each other. It was observed that the short-term exposure to relative humidity conditions did not exhibit a notable impact on the mechanical properties or fracture toughness of degraded or undegraded cement paste. Results across exposure times were also analyzed for significance. The neat samples showed an expected trend that the 1-week strength and fracture toughness was typically significantly lower when compared with the

12-week results. However, the expected trend that 12- and 24-week results would be similar or not significantly different was not observed. The sulfate attack samples for the 12- and 24-week exposures exhibited overall similar behavior, which is inferred to be due to samples having not been exposed long enough for an observable impact on properties.

Considering the neat, sulfate attack, and calcium leached results from the 12-week exposure set, it was observed that both sulfate attack and calcium leaching led to an apparent loss in stiffness, strength, and fracture toughness. For the conditions in this study, it was observed that calcium leaching had a greater impact on fracture toughness than sulfate attack.

Leached depth was analyzed in the 12-week samples through fluorescence as well as a microstructural TGA test. The fluorescence showed clear leached depth in the calcium leached samples, but not in the sulfate attack samples. This could be due to the sulfate solution's similar pH to that of neat cement, making it difficult to identify a clear leached depth. TGA tests showed weight derivative peaks reflecting the presence of binding compounds (ettringite, gypsum, CH, and calcium carbonate) as well as the presence of leaching product (calcium nitrate). The neat samples exhibited similar behavior across the 5 depths tested. The sulfate attack samples also exhibited similar behavior across depths; the edge of the degradation plane did exhibit a higher ettringite peak than the center. This is explained by the fact that sulfate attack leads to new and increased formation of ettringite. The calcium leached samples seemingly had similar curves to that of the neat and sulfate attack samples, but this was explained by the fact that products of the leaching reactions (calcium nitrate, ammonium nitrate, and nitrogen) dehydrate and dissociate at similar temperatures as ettringite, portlandite (CH), and calcium carbonate.

Damage due to degradation was quantified by observing change in stiffness as well as leached depth. Stiffness values were taken from the average 99%RH exposure values. It was observed that when compared to neat samples of the same age, after 12-weeks exposure, the sulfate attack samples saw a 59% decrease in stiffness, while the calcium leached samples saw a 79% decrease in stiffness. After 24-weeks exposure, the sulfate attack samples saw a 48% decrease in stiffness when compared to the neat results of the same age. Leached depth was unable to be quantified for the sulfate attack samples. The leached depth for the calcium leached samples averaged 9.3mm (from the edge to the center of the degradation plane), this reflects 74% damage. With this, and the observations in mechanical and fracture properties, calcium leaching proved to have the greatest negative impact on cement paste when compared to sulfate attack.

Future work could include testing at late ages to give a better picture of the complicated nature of cement degradation as exposure time changes. Since the calcium leached samples become over leached beyond 12-weeks of exposure in these conditions, it might be important to consider testing at the earlier exposure times as this would give crucial insight into the evolving effect of degradation of the cementitious matrix due to calcium leaching. Future work might also include chemical and microstructural investigations of both the sulfate attack and calcium leached degraded samples up to 12-weeks of age. Another area of interest would be to devise a testing scheme to evaluate degradation and relative humidity in parallel, rather than in-series, as they were applied in this study.

6. REFERENCES

- [1] P.K. Mehta, P.J.M. Monteiro, *Concrete: Microstructure, Properties, and Materials*, 3rd ed., McGraw Hill, 2006.
- [2] J.F. Young, S. Mindess, A. Bentur, R.J. Gray, *The Science and Technology of Civil Engineering Materials*, Pearson, 1998. /content/one-dot-com/one-dot-com/us/en/higher-education/program.html (accessed February 8, 2021).
- [3] J. Lemaitre, H. Lippmann, *A Course on Damage Mechanics*, 2nd rev. and enlarged ed. edition, Springer, Berlin ; New York, 1996.
- [4] C. Carde, R. François, Modelling the loss of strength and porosity increase due to the leaching of cement pastes, *Cem. Concr. Compos.* 21 (1999) 181–188. [https://doi.org/10.1016/S0958-9465\(98\)00046-8](https://doi.org/10.1016/S0958-9465(98)00046-8).
- [5] A. Delagrave, B. Gerard, J. Marchand, Modelling calcium leaching mechanisms in hydrated cement pastes, in: *Mech. Chem. Degrad. Cem.-Based Syst.*, CRC Press, 1997: pp. 38–49.
- [6] A.E. Morandau, C.E. White, In situ X-ray pair distribution function analysis of accelerated carbonation of a synthetic calcium–silicate–hydrate gel, *J. Mater. Chem. A.* 3 (2015) 8597–8605. <https://doi.org/10.1039/C5TA00348B>.
- [7] F. Adenot, M. Buil, Modelling of the corrosion of the cement paste by deionized water, *Cem. Concr. Res.* 22 (1992) 489–496. [https://doi.org/10.1016/0008-8846\(92\)90092-A](https://doi.org/10.1016/0008-8846(92)90092-A).
- [8] R.F. Feldman, V.S. Ramachandran, Microstructure of calcium hydroxide depleted portland cement paste I: Density and helium flow measurements, *Cem. Concr. Res.* 12 (1982) 179–189. [https://doi.org/10.1016/0008-8846\(82\)90005-9](https://doi.org/10.1016/0008-8846(82)90005-9).
- [9] F.M. Lea, The action of ammonium salts on concrete, *Mag. Concr. Res.* 17 (1965) 115–116. <https://doi.org/10.1680/mac.1965.17.52.115>.
- [10] F.P. Glasser, J. Marchand, E. Samson, Durability of concrete — Degradation phenomena involving detrimental chemical reactions, *Cem. Concr. Res.* 38 (2008) 226–246. <https://doi.org/10.1016/j.cemconres.2007.09.015>.
- [11] Bellégo C. Le, Gérard B., Pijaudier-Cabot G., Chemo-Mechanical Effects in Mortar Beams Subjected to Water Hydrolysis, *J. Eng. Mech.* 126 (2000) 266–272. [https://doi.org/10.1061/\(ASCE\)0733-9399\(2000\)126:3\(266\)](https://doi.org/10.1061/(ASCE)0733-9399(2000)126:3(266)).
- [12] C. Carde, R. François, J.-P. Ollivier, Microstructural changes and mechanical effects due to the leaching of calcium hydroxide from cement paste, in: *Mech. Chem. Degrad. Cem.-Based Syst.*, CRC Press, 1997: pp. 30–37.
- [13] Y.S. Choi, E.I. Yang, Effect of calcium leaching on the pore structure, strength, and chloride penetration resistance in concrete specimens, *Nucl. Eng. Des.* 259 (2013) 126–136. <https://doi.org/10.1016/j.nucengdes.2013.02.049>.
- [14] C. Ouyang, A Damage Model for Sulfate Attack of Cement Mortars, *Cem. Concr. Aggreg.* 11 (1989) 92–99. <https://doi.org/10.1520/CCA10109J>.
- [15] D.M. Roy, W. Jiang, Concrete chemical degradation: ancient analogues and modern evaluation, in: *Mech. Chem. Degrad. Cem.-Based Syst.*, CRC Press, 1997: pp. 14–21.
- [16] N. Thaulow, U.H. Jakobsen, The Diagnosis of Chemical Deterioration of Concrete by Optical Microscopy, in: *Mech. Chem. Degrad. Cem.-Based Syst.*, CRC Press, 1997: pp. 3–13.

- [17] J.G. Wang, Sulfate attack on hardened cement paste, *Cem. Concr. Res.* 24 (1994) 735–742. [https://doi.org/10.1016/0008-8846\(94\)90199-6](https://doi.org/10.1016/0008-8846(94)90199-6).
- [18] Y. Fu, J. Ding, J.J. Beaudoin, Expansion of portland cement mortar due to internal sulfate attack, *Cem. Concr. Res.* 27 (1997) 1299–1306. [https://doi.org/10.1016/S0008-8846\(97\)00133-6](https://doi.org/10.1016/S0008-8846(97)00133-6).
- [19] M. Zhang, J. Chen, Y. Lv, D. Wang, J. Ye, Study on the expansion of concrete under attack of sulfate and sulfate–chloride ions, *Constr. Build. Mater.* 39 (2013) 26–32. <https://doi.org/10.1016/j.conbuildmat.2012.05.003>.
- [20] X. Ma, O. Çopuroğlu, E. Schlangen, N. Han, F. Xing, Expansion and degradation of cement paste in sodium sulfate solutions, *Constr. Build. Mater.* 158 (2018) 410–422. <https://doi.org/10.1016/j.conbuildmat.2017.10.026>.
- [21] Y. Zhou, H. Tian, L. Sui, F. Xing, N. Han, Strength Deterioration of Concrete in Sulfate Environment: An Experimental Study and Theoretical Modeling, *Adv. Mater. Sci. Eng.* 2015 (2015) e951209. <https://doi.org/10.1155/2015/951209>.
- [22] K. Liu, M. Deng, L. Mo, J. Tang, Deterioration mechanism of Portland cement paste subjected to sodium sulfate attack, *Adv. Cem. Res.* 27 (2015) 477–486. <https://doi.org/10.1680/adcr.14.00051>.
- [23] X. Ma, O. Çopuroğlu, E. Schlangen, N. Han, F. Xing, Expansion and degradation of cement paste in sodium sulfate solutions, *Constr. Build. Mater.* 158 (2018) 410–422. <https://doi.org/10.1016/j.conbuildmat.2017.10.026>.
- [24] D. Planel, J. Sercombe, P. Le Bescop, F. Adenot, J.-M. Torrenti, Long-term performance of cement paste during combined calcium leaching–sulfate attack: kinetics and size effect, *Cem. Concr. Res.* 36 (2006) 137–143. <https://doi.org/10.1016/j.cemconres.2004.07.039>.
- [25] C. Liu, J. Gao, F. Chen, Y. Zhao, X. Chen, Z. He, Coupled effect of relative humidity and temperature on the degradation of cement mortars partially exposed to sulfate attack, *Constr. Build. Mater.* 216 (2019) 93–100. <https://doi.org/10.1016/j.conbuildmat.2019.05.001>.
- [26] A. Duguid, G.W. Scherer, Degradation of oilwell cement due to exposure to carbonated brine, *Int. J. Greenh. Gas Control.* 4 (2010) 546–560. <https://doi.org/10.1016/j.ijggc.2009.11.001>.
- [27] B.G. Kutchko, B.R. Strazisar, D.A. Dzombak, G.V. Lowry, N. Thaulow, Degradation of Well Cement by CO₂ under Geologic Sequestration Conditions, *Environ. Sci. Technol.* 41 (2007) 4787–4792. <https://doi.org/10.1021/es062828c>.
- [28] B.G. Kutchko, B.R. Strazisar, G.V. Lowry, D.A. Dzombak, N. Thaulow, Rate of CO₂ Attack on Hydrated Class H Well Cement under Geologic Sequestration Conditions, *Environ. Sci. Technol.* 42 (2008) 6237–6242. <https://doi.org/10.1021/es800049r>.
- [29] B. Šavija, M. Luković, Carbonation of cement paste: Understanding, challenges, and opportunities, *Constr. Build. Mater.* 117 (2016) 285–301. <https://doi.org/10.1016/j.conbuildmat.2016.04.138>.
- [30] A.E. Morandau, C.E. White, In situ X-ray pair distribution function analysis of accelerated carbonation of a synthetic calcium–silicate–hydrate gel, *J. Mater. Chem. A.* 3 (2015) 8597–8605. <https://doi.org/10.1039/C5TA00348B>.
- [31] T. Gu, X. Guo, Z. Li, X. Cheng, X. Fan, A. Korayem, W.H. Duan, Coupled effect of CO₂ attack and tensile stress on well cement under CO₂ storage conditions, *Constr.*

- Build. Mater. 130 (2017) 92–102.
<https://doi.org/10.1016/j.conbuildmat.2016.10.117>.
- [32] C.A. García-González, N. el Grouh, A. Hidalgo, J. Fraile, A.M. López-Periago, C. Andrade, C. Domingo, New insights on the use of supercritical carbon dioxide for the accelerated carbonation of cement pastes, *J. Supercrit. Fluids.* 43 (2008) 500–509. <https://doi.org/10.1016/j.supflu.2007.07.018>.
- [33] L. Urbonas, V. Leno, D. Heinz, Effect of carbonation in supercritical CO₂ on the properties of hardened cement paste of different alkalinity, *Constr. Build. Mater.* 123 (2016) 704–711. <https://doi.org/10.1016/j.conbuildmat.2016.07.040>.
- [34] M. Balonis, B. Lothenbach, G. Le Saout, F.P. Glasser, Impact of chloride on the mineralogy of hydrated Portland cement systems, *Cem. Concr. Res.* 40 (2010) 1009–1022. <https://doi.org/10.1016/j.cemconres.2010.03.002>.
- [35] T. Matschei, B. Lothenbach, F.P. Glasser, The AFm phase in Portland cement, *Cem. Concr. Res.* 37 (2007) 118–130. <https://doi.org/10.1016/j.cemconres.2006.10.010>.
- [36] D.M. Roy, W. Jiang, Concrete chemical degradation: ancient analogues and modern evaluation, in: *Mech. Chem. Degrad. Cem.-Based Syst.*, CRC Press, 1997: pp. 14–21.
- [37] E.M. Winkler, *Stone: properties, durability in man's environment*, New York, 1973. <http://hdl.handle.net/2027/mdp.39015006813672>.
- [38] C. Villani, Y. Farnam, T. Washington, J. Jain, W.J. Weiss, Conventional Portland Cement and Carbonated Calcium Silicate-Based Cement Systems: Performance During Freezing and Thawing in Presence of Calcium Chloride Deicing Salts, *Transp. Res. Rec.* 2508 (2015) 48–54. <https://doi.org/10.3141/2508-06>.
- [39] W. Zhang, W. Sun, Y. Zhang, H. Chen, Degradation of pore structure and microstructures in hardened cement paste subjected to flexural loading and wet-dry cycles in sea water, *J. Wuhan Univ. Technol.-Mater Sci Ed.* 24 (2009) 940. <https://doi.org/10.1007/s11595-006-6940-1>.
- [40] Y. Farnam, S. Dick, A. Wiese, J. Davis, D. Bentz, J. Weiss, The influence of calcium chloride deicing salt on phase changes and damage development in cementitious materials, *Cem. Concr. Compos.* 64 (2015) 1–15. <https://doi.org/10.1016/j.cemconcomp.2015.09.006>.
- [41] K. Wang, D.E. Nelsen, W.A. Nixon, Damaging effects of deicing chemicals on concrete materials, *Cem. Concr. Compos.* 28 (2006) 173–188. <https://doi.org/10.1016/j.cemconcomp.2005.07.006>.
- [42] Y. Farnam, A. Wiese, D. Bentz, J. Davis, J. Weiss, Damage development in cementitious materials exposed to magnesium chloride deicing salt, *Constr. Build. Mater.* 93 (2015) 384–392. <https://doi.org/10.1016/j.conbuildmat.2015.06.004>.
- [43] I. Segura, M. Molero, S. Aparicio, J.J. Anaya, A. Moragues, Decalcification of cement mortars: Characterisation and modelling, *Cem. Concr. Compos.* 35 (2013) 136–150. <https://doi.org/10.1016/j.cemconcomp.2012.08.015>.
- [44] W. Li, L. Guo, Meso-fracture simulation of cracking process in concrete incorporating three-phase characteristics by peridynamic method, *Constr. Build. Mater.* 161 (2018) 665–675. <https://doi.org/10.1016/j.conbuildmat.2017.12.002>.
- [45] J. Zhao, Z. Chen, J. Mehrmashhadi, F. Bobaru, A stochastic multiscale peridynamic model for corrosion-induced fracture in reinforced concrete, *Eng. Fract. Mech.* 229 (2020) 106969. <https://doi.org/10.1016/j.engfracmech.2020.106969>.

- [46] D. Krajcinovic, Continuum Damage Mechanics, *Appl. Mech. Rev.* 37 (1984) 1–6.
- [47] K. Kurumisawa, K. Haga, D. Hayashi, H. Owada, Effects of calcium leaching on diffusion properties of hardened and altered cement pastes, *Phys. Chem. Earth Parts ABC.* 99 (2017) 175–183. <https://doi.org/10.1016/j.pce.2017.03.007>.
- [48] W. Ponloa, S. Sajjavanich, Effects of calcium leaching from high volume fly ash cement paste and mortar, *Mater. Today Proc.* 5 (2018) 9453–9460. <https://doi.org/10.1016/j.matpr.2017.10.124>.
- [49] L. Liu, X. Wang, J. Zhou, H. Chu, D. Shen, H. Chen, S. Qin, Investigation of pore structure and mechanical property of cement paste subjected to the coupled action of freezing/thawing and calcium leaching, *Cem. Concr. Res.* 109 (2018) 133–146. <https://doi.org/10.1016/j.cemconres.2018.04.015>.
- [50] C. Liu, J. Gao, F. Chen, Y. Zhao, X. Chen, Z. He, Coupled effect of relative humidity and temperature on the degradation of cement mortars partially exposed to sulfate attack, *Constr. Build. Mater.* 216 (2019) 93–100. <https://doi.org/10.1016/j.conbuildmat.2019.05.001>.
- [51] C. Carde, R. François, Modelling the loss of strength and porosity increase due to the leaching of cement pastes, *Cem. Concr. Compos.* 21 (1999) 181–188. [https://doi.org/10.1016/S0958-9465\(98\)00046-8](https://doi.org/10.1016/S0958-9465(98)00046-8).
- [52] Y.S. Choi, E.I. Yang, Effect of calcium leaching on the pore structure, strength, and chloride penetration resistance in concrete specimens, *Nucl. Eng. Des.* 259 (2013) 126–136. <https://doi.org/10.1016/j.nucengdes.2013.02.049>.
- [53] C. Carde, R. François, J.-P. Ollivier, Microstructural changes and mechanical effects due to the leaching of calcium hydroxide from cement paste, in: *Mech. Chem. Degrad. Cem.-Based Syst.*, CRC Press, 1997: pp. 30–37.
- [54] H. Saito, A. Deguchi, Leaching tests on different mortars using accelerated electrochemical method, *Cem. Concr. Res.* 30 (2000) 1815–1825. [https://doi.org/10.1016/S0008-8846\(00\)00377-X](https://doi.org/10.1016/S0008-8846(00)00377-X).
- [55] J.G. Wang, Sulfate attack on hardened cement paste, *Cem. Concr. Res.* 24 (1994) 735–742. [https://doi.org/10.1016/0008-8846\(94\)90199-6](https://doi.org/10.1016/0008-8846(94)90199-6).
- [56] A. Duguid, G.W. Scherer, Degradation of oilwell cement due to exposure to carbonated brine, *Int. J. Greenh. Gas Control.* 4 (2010) 546–560. <https://doi.org/10.1016/j.ijggc.2009.11.001>.
- [57] C. Ouyang, A Damage Model for Sulfate Attack of Cement Mortars, *Cem. Concr. Aggreg.* 11 (1989) 92–99. <https://doi.org/10.1520/CCA10109J>.
- [58] H. Ma, Mercury intrusion porosimetry in concrete technology: tips in measurement, pore structure parameter acquisition and application, *J. Porous Mater.* 21 (2014) 207–215. <https://doi.org/10.1007/s10934-013-9765-4>.
- [59] S. Catinaud, J.J. Beaudoin, J. Marchand, Influence of limestone addition on calcium leaching mechanisms in cement-based materials, *Cem. Concr. Res.* 30 (2000) 1961–1968. [https://doi.org/10.1016/S0008-8846\(00\)00385-9](https://doi.org/10.1016/S0008-8846(00)00385-9).
- [60] Mercury Intrusion Porosimetry, Part. *Technol. Labs.* (n.d.). <https://www.particletechlabs.com/analytical-testing/gas-adsorption-and-porosimetry/mercury-intrusion-porosimetry> (accessed July 10, 2020).
- [61] D18 Committee, Standard Test Method for Determination of Pore Volume and Pore Volume Distribution of Soil and Rock by Mercury Intrusion Porosimetry, ASTM International, West Conshohocken, PA, 2010.

- [62] E.J. Garboczi, Permeability, diffusivity, and microstructural parameters: A critical review, *Cem. Concr. Res.* 20 (1990) 591–601. [https://doi.org/10.1016/0008-8846\(90\)90101-3](https://doi.org/10.1016/0008-8846(90)90101-3).
- [63] K. Kurumisawa, T. Nawa, H. Owada, Prediction of the diffusivity of cement-based materials using a three-dimensional spatial distribution model, *Cem. Concr. Compos.* 34 (2012) 408–418. <https://doi.org/10.1016/j.cemconcomp.2011.11.011>.
- [64] E.J. Garboczi, Finite element and finite difference programs for computing the linear electric and elastic properties of digital images of random materials, Building and Fire Research Laboratory, National Institute of Standards and Technology, 1998.
- [65] C09 Committee, Test Method for Electrical Indication of Concretes Ability to Resist Chloride Ion Penetration, ASTM International, n.d. <https://doi.org/10.1520/C1202-19>.
- [66] I. Hohberg, G.J. de Groot, A.M.H. van der Veen, W. Wassing, Development of a leaching protocol for concrete, *Waste Manag.* 20 (2000) 177–184. [https://doi.org/10.1016/S0956-053X\(99\)00324-4](https://doi.org/10.1016/S0956-053X(99)00324-4).
- [67] F. Adenot, M. Buil, Modelling of the corrosion of the cement paste by deionized water, *Cem. Concr. Res.* 22 (1992) 489–496. [https://doi.org/10.1016/0008-8846\(92\)90092-A](https://doi.org/10.1016/0008-8846(92)90092-A).
- [68] A. Delagrave, B. Gerard, J. Marchand, Modelling calcium leaching mechanisms in hydrated cement pastes, in: *Mech. Chem. Degrad. Cem.-Based Syst.*, CRC Press, 1997: pp. 38–49.
- [69] A. Duguid, An estimate of the time to degrade the cement sheath in a well exposed to carbonated brine, *Energy Procedia.* 1 (2009) 3181–3188. <https://doi.org/10.1016/j.egypro.2009.02.101>.
- [70] V.G. Papadakis, C.G. Vayenas, M.N. Fardis, Experimental investigation and mathematical modeling of the concrete carbonation problem, *Chem. Eng. Sci.* 46 (1991) 1333–1338. [https://doi.org/10.1016/0009-2509\(91\)85060-B](https://doi.org/10.1016/0009-2509(91)85060-B).
- [71] Y. Lo, H.M. Lee, Curing effects on carbonation of concrete using a phenolphthalein indicator and Fourier-transform infrared spectroscopy, *Build. Environ.* 37 (2002) 507–514. [https://doi.org/10.1016/S0360-1323\(01\)00052-X](https://doi.org/10.1016/S0360-1323(01)00052-X).
- [72] A.W. Coats, J.P. Redfern, Thermogravimetric analysis. A review, *Analyst.* 88 (1963) 906–924. <https://doi.org/10.1039/AN9638800906>.
- [73] G. Rytwo, R. Zakai, B. Wicklein, The Use of ATR-FTIR Spectroscopy for Quantification of Adsorbed Compounds, *J. Spectrosc.* 2015 (2015) 8 pp. <https://doi.org/10.1155/2015/727595>.
- [74] L. Alarcon-Ruiz, G. Platret, E. Massieu, A. Ehrlacher, The use of thermal analysis in assessing the effect of temperature on a cement paste, *Cem. Concr. Res.* 35 (2005) 609–613. <https://doi.org/10.1016/j.cemconres.2004.06.015>.
- [75] Q.T. Phung, N. Maes, S. Seetharam, Pitfalls in the use and interpretation of TGA and MIP techniques for Ca-leached cementitious materials, *Mater. Des.* 182 (2019) 108041. <https://doi.org/10.1016/j.matdes.2019.108041>.
- [76] B.Z. Dilnesa, Application of Thermogravimetric Method in Cement Science, in: 2010: p. 1.

- [77] H. Yu, J. Yang, H. Rong, Research on decalcification degradation process of cement stone, *J. Wuhan Univ. Technol.-Mater Sci Ed.* 30 (2015) 369–374. <https://doi.org/10.1007/s11595-015-1154-1>.
- [78] M. Mbessa, J. Péra, Durability of high-strength concrete in ammonium sulfate solution, *Cem. Concr. Res.* 31 (2001) 1227–1231. [https://doi.org/10.1016/S0008-8846\(01\)00553-1](https://doi.org/10.1016/S0008-8846(01)00553-1).
- [79] R.F. Feldman, V.S. Ramachandran, Microstructure of calcium hydroxide depleted portland cement paste I: Density and helium flow measurements, *Cem. Concr. Res.* 12 (1982) 179–189. [https://doi.org/10.1016/0008-8846\(82\)90005-9](https://doi.org/10.1016/0008-8846(82)90005-9).
- [80] C.E. Inglis, Stresses in A Plate Due To The Presence of Cracks and Sharp Corners, *Tran Inst Nav. Archit.* (1913) 219–241.
- [81] A.A. Griffith, G.I. Taylor, VI. The phenomena of rupture and flow in solids, *Philos. Trans. R. Soc. Lond. Ser. Contain. Pap. Math. Phys. Character.* 221 (1921) 163–198. <https://doi.org/10.1098/rsta.1921.0006>.
- [82] M.M. Reda Taha, X. Xiao, J. Yi, N.G. Shrive, Evaluation of flexural fracture toughness for quasi-brittle structural materials using a simple test method, *Can. J. Civ. Eng.* (2002) 567–575. <https://doi.org/10.1139/L02-044>.
- [83] S.P. Shah, S.E. Swartz, C. Ouyang, *Fracture Mechanics of Concrete: Applications of Fracture Mechanics to Concrete, Rock and Other Quasi-Brittle Materials*, Wiley, 1995. <https://www.wiley.com/en-us/Fracture+Mechanics+of+Concrete%3A+Applications+of+Fracture+Mechanics+to+Concrete%2C+Rock+and+Other+Quasi+Brittle+Materials-p-9780471303114> (accessed June 20, 2021).
- [84] ACI Committee 446, *Fracture Toughness Testing of Concrete*, American Concrete Institute, 2010.
- [85] Y. Jenq, S.P. Shah, Two Parameter Fracture Model for Concrete, *J. Eng. Mech.* 111 (1985) 1227–1241. [https://doi.org/10.1061/\(ASCE\)0733-9399\(1985\)111:10\(1227\)](https://doi.org/10.1061/(ASCE)0733-9399(1985)111:10(1227)).
- [86] A. Douba, *Mechanical Characterization of Polymer Concrete with Nanomaterials*, Masters, University of New Mexico, 2017. https://digitalrepository.unm.edu/ce_etds/173.
- [87] Y. Fu, J. Ding, J.J. Beaudoin, Expansion of portland cement mortar due to internal sulfate attack, *Cem. Concr. Res.* 27 (1997) 1299–1306. [https://doi.org/10.1016/S0008-8846\(97\)00133-6](https://doi.org/10.1016/S0008-8846(97)00133-6).

7. APPENDICES

Appendix A: Matlab Code

```
function DataAnalysis

%Function to process fracture and flexure data for 150x25x25mm
(LxWxD) specimens
%The "Bionix" files contain load and CMOD data
%The "LVDT" files contain the vertical displacement data from the
two LVDTs
%"notes" communicates whether there are any issues to address
with the
%LVDTs
%Make sure to load data in correctly and save workspace in this
folder

clc
clear
close all

%Make sure to use the ' quotes and put exact file name! ex:
'Trial_Data.mat'
filename = input('Name of .mat file with data: ');
load(filename)

notes

%Prep notched data
%Zero data
N1_Bionix(:,2) = abs(N1_Bionix(:,2)-N1_Bionix(1,2));
N1_Bionix(:,4) = abs(N1_Bionix(:,4)-N1_Bionix(1,4));
N2_Bionix(:,2) = abs(N2_Bionix(:,2)-N2_Bionix(1,2));
N2_Bionix(:,4) = abs(N2_Bionix(:,4)-N2_Bionix(1,4));
N3_Bionix(:,2) = abs(N3_Bionix(:,2)-N3_Bionix(1,2));
N3_Bionix(:,4) = abs(N3_Bionix(:,4)-N3_Bionix(1,4));
N4_Bionix(:,2) = abs(N4_Bionix(:,2)-N4_Bionix(1,2));
N4_Bionix(:,4) = abs(N4_Bionix(:,4)-N4_Bionix(1,4));
N5_Bionix(:,2) = abs(N5_Bionix(:,2)-N5_Bionix(1,2));
N5_Bionix(:,4) = abs(N5_Bionix(:,4)-N5_Bionix(1,4));
N6_Bionix(:,2) = abs(N6_Bionix(:,2)-N6_Bionix(1,2));
N6_Bionix(:,4) = abs(N6_Bionix(:,4)-N6_Bionix(1,4));

N1_LVDT(:,1) = abs(N1_LVDT(:,1)-N1_LVDT(1,1));
N1_LVDT(:,2) = abs(N1_LVDT(:,2)-N1_LVDT(1,2));
N2_LVDT(:,1) = abs(N2_LVDT(:,1)-N2_LVDT(1,1));
N2_LVDT(:,2) = abs(N2_LVDT(:,2)-N2_LVDT(1,2));
N3_LVDT(:,1) = abs(N3_LVDT(:,1)-N3_LVDT(1,1));
N3_LVDT(:,2) = abs(N3_LVDT(:,2)-N3_LVDT(1,2));
N4_LVDT(:,1) = abs(N4_LVDT(:,1)-N4_LVDT(1,1));
N4_LVDT(:,2) = abs(N4_LVDT(:,2)-N4_LVDT(1,2));
N5_LVDT(:,1) = abs(N5_LVDT(:,1)-N5_LVDT(1,1));
```

```

N5_LVDT(:,2) = abs(N5_LVDT(:,2)-N5_LVDT(1,2));
N6_LVDT(:,1) = abs(N6_LVDT(:,1)-N6_LVDT(1,1));
N6_LVDT(:,2) = abs(N6_LVDT(:,2)-N6_LVDT(1,2));

%Matrix of max loads
%First column is x coord. (CMOD), second column is y coord. of
peak (Load)
NPeak(1,2) = max(N1_Bionix(:,2));
NPeak(2,2) = max(N2_Bionix(:,2));
NPeak(3,2) = max(N3_Bionix(:,2));
NPeak(4,2) = max(N4_Bionix(:,2));
NPeak(5,2) = max(N5_Bionix(:,2));
NPeak(6,2) = max(N6_Bionix(:,2));

NPeak(1,1) = N1_Bionix(find(N1_Bionix(:,2)==NPeak(1,2)),4);
NPeak(2,1) = N2_Bionix(find(N2_Bionix(:,2)==NPeak(2,2)),4);
NPeak(3,1) = N3_Bionix(find(N3_Bionix(:,2)==NPeak(3,2)),4);
NPeak(4,1) = N4_Bionix(find(N4_Bionix(:,2)==NPeak(4,2)),4);
NPeak(5,1) = N5_Bionix(find(N5_Bionix(:,2)==NPeak(5,2)),4);
NPeak(6,1) = N6_Bionix(find(N6_Bionix(:,2)==NPeak(6,2)),4);

%Prep unnotched data
%Zero data
U1_Bionix(:,2) = abs(U1_Bionix(:,2)-U1_Bionix(1,2));
U1_Bionix(:,3) = abs(U1_Bionix(:,3)-U1_Bionix(1,3));
U2_Bionix(:,2) = abs(U2_Bionix(:,2)-U2_Bionix(1,2));
U2_Bionix(:,3) = abs(U2_Bionix(:,3)-U2_Bionix(1,3));
U3_Bionix(:,2) = abs(U3_Bionix(:,2)-U3_Bionix(1,2));
U3_Bionix(:,3) = abs(U3_Bionix(:,3)-U3_Bionix(1,3));
U4_Bionix(:,2) = abs(U4_Bionix(:,2)-U4_Bionix(1,2));
U4_Bionix(:,3) = abs(U4_Bionix(:,3)-U4_Bionix(1,3));
U5_Bionix(:,2) = abs(U5_Bionix(:,2)-U5_Bionix(1,2));
U5_Bionix(:,3) = abs(U5_Bionix(:,3)-U5_Bionix(1,3));
U6_Bionix(:,2) = abs(U6_Bionix(:,2)-U6_Bionix(1,2));
U6_Bionix(:,3) = abs(U6_Bionix(:,3)-U6_Bionix(1,3));

U1_LVDT(:,1) = abs(U1_LVDT(:,1)-U1_LVDT(1,1));
U1_LVDT(:,2) = abs(U1_LVDT(:,2)-U1_LVDT(1,2));
U2_LVDT(:,1) = abs(U2_LVDT(:,1)-U2_LVDT(1,1));
U2_LVDT(:,2) = abs(U2_LVDT(:,2)-U2_LVDT(1,2));
U3_LVDT(:,1) = abs(U3_LVDT(:,1)-U3_LVDT(1,1));
U3_LVDT(:,2) = abs(U3_LVDT(:,2)-U3_LVDT(1,2));
U4_LVDT(:,1) = abs(U4_LVDT(:,1)-U4_LVDT(1,1));
U4_LVDT(:,2) = abs(U4_LVDT(:,2)-U4_LVDT(1,2));
U5_LVDT(:,1) = abs(U5_LVDT(:,1)-U5_LVDT(1,1));
U5_LVDT(:,2) = abs(U5_LVDT(:,2)-U5_LVDT(1,2));
U6_LVDT(:,1) = abs(U6_LVDT(:,1)-U6_LVDT(1,1));
U6_LVDT(:,2) = abs(U6_LVDT(:,2)-U6_LVDT(1,2));

%find ratio of size of Bionix file to LVDT file, this is always
slightly larger than 1

```

```

b1 = size(U1_Bionix)/size(U1_LVDT);
b2 = size(U2_Bionix)/size(U2_LVDT);
b3 = size(U3_Bionix)/size(U3_LVDT);
b4 = size(U4_Bionix)/size(U4_LVDT);
b5 = size(U5_Bionix)/size(U5_LVDT);
b6 = size(U6_Bionix)/size(U6_LVDT);

%Matrix with peak loads
UPeak(1,2) = max(U1_Bionix(:,2));
UPeak(2,2) = max(U2_Bionix(:,2));
UPeak(3,2) = max(U3_Bionix(:,2));
UPeak(4,2) = max(U4_Bionix(:,2));
UPeak(5,2) = max(U5_Bionix(:,2));
UPeak(6,2) = max(U6_Bionix(:,2));

%Locating peak to trim the data to that point - we do not need
any post-peak behavior from flexure tests
x1 = find(U1_Bionix(:,2) == UPeak(1,2));
x2 = find(U2_Bionix(:,2) == UPeak(2,2));
x3 = find(U3_Bionix(:,2) == UPeak(3,2));
x4 = find(U4_Bionix(:,2) == UPeak(4,2));
x5 = find(U5_Bionix(:,2) == UPeak(5,2));
x6 = find(U6_Bionix(:,2) == UPeak(6,2));

%Trim data and making last load point = 0N
U1_Bionix = U1_Bionix(1:x1,:);
U1_Bionix(x1+1,:) = 0;
U2_Bionix = U2_Bionix(1:x2,:);
U2_Bionix(x2+1,:) = 0;
U3_Bionix = U3_Bionix(1:x3,:);
U3_Bionix(x3+1,:) = 0;
U4_Bionix = U4_Bionix(1:x4,:);
U4_Bionix(x4+1,:) = 0;
U5_Bionix = U5_Bionix(1:x5,:);
U5_Bionix(x5+1,:) = 0;
U6_Bionix = U6_Bionix(1:x6,:);
U6_Bionix(x6+1,:) = 0;

%Find ratio to proportionally trim the LVDT files
xx1 = (x1+1)/b1;
xx2 = (x2+1)/b2;
xx3 = (x3+1)/b3;
xx4 = (x4+1)/b4;
xx5 = (x5+1)/b5;
xx6 = (x6+1)/b6;

%Trim LVDT file to end at same time as the new Bionix file
U1_LVDT = U1_LVDT(1:xx1,:);
U2_LVDT = U2_LVDT(1:xx2,:);
U3_LVDT = U3_LVDT(1:xx3,:);
U4_LVDT = U4_LVDT(1:xx4,:);
U5_LVDT = U5_LVDT(1:xx5,:);

```

```
U6_LVDT = U6_LVDT(1:xx6,:);
```

```
%% Notched data analysis - Load-CMOD
```

```
%Plot raw Load-CMOD
```

```
figure
```

```
plot(N1_Bionix(:,4),N1_Bionix(:,2),N2_Bionix(:,4),N2_Bionix(:,2),  
N3_Bionix(:,4),N3_Bionix(:,2),N4_Bionix(:,4),N4_Bionix(:,2),N5_Bi  
onix(:,4),N5_Bionix(:,2),N6_Bionix(:,4),N6_Bionix(:,2))
```

```
grid on
```

```
hold on
```

```
%This calls out the values at the peak points
```

```
plot(NPeak(:,1),NPeak(:,2),'k*')
```

```
for i = 1:size(NPeak)
```

```
    thisX = NPeak(i,1);
```

```
    thisY = NPeak(i,2);
```

```
    labelstr = sprintf(' %.5fmm, %.1fN',thisX,thisY);
```

```
    text(thisX,thisY,labelstr,'FontSize',16);
```

```
end
```

```
legend('N1','N2','N3','N4','N5','N6','FontSize',16)
```

```
title('1NEAT99','FontSize',16)
```

```
xlim([0 0.1])
```

```
xlabel('CMOD (mm)','FontSize',16)
```

```
ylim([0 200])
```

```
ylabel('Load (N)','FontSize',16)
```

```
%Smoothing load and CMOD data
```

```
smooth_CMOD1 = smooth(N1_Bionix(:,4),1000);
```

```
smooth_Load1 = smooth(N1_Bionix(:,2),1000);
```

```
smooth_CMOD2 = smooth(N2_Bionix(:,4),1000);
```

```
smooth_Load2 = smooth(N2_Bionix(:,2),1000);
```

```
smooth_CMOD3 = smooth(N3_Bionix(:,4),1000);
```

```
smooth_Load3 = smooth(N3_Bionix(:,2),1000);
```

```
smooth_CMOD4 = smooth(N4_Bionix(:,4),1000);
```

```
smooth_Load4 = smooth(N4_Bionix(:,2),1000);
```

```
smooth_CMOD5 = smooth(N5_Bionix(:,4),1000);
```

```
smooth_Load5 = smooth(N5_Bionix(:,2),1000);
```

```
smooth_CMOD6 = smooth(N6_Bionix(:,4),1000);
```

```
smooth_Load6 = smooth(N6_Bionix(:,2),1000);
```

```
%Fracture energy calculation
```

```
Gf(1,1) = trapz(smooth_CMOD1,smooth_Load1)/(25*(25-8))*1000;
```

```
Gf(2,1) = trapz(smooth_CMOD2,smooth_Load2)/(25*(25-8))*1000;
```

```
Gf(3,1) = trapz(smooth_CMOD3,smooth_Load3)/(25*(25-8))*1000;
```

```
Gf(4,1) = trapz(smooth_CMOD4,smooth_Load4)/(25*(25-8))*1000;
```

```
Gf(5,1) = trapz(smooth_CMOD5,smooth_Load5)/(25*(25-8))*1000;
```

```
Gf(6,1) = trapz(smooth_CMOD6,smooth_Load6)/(25*(25-8))*1000;
```

```
Gf_mean = mean(nonzeros(Gf));
```

```
Gf_std = std(nonzeros(Gf));
```

```

%% Notched data analysis - Load-Disp.

%Avg. LVDTs - assuming both LVDT1 & LVDT2 are usable, unless told
otherwise in "notes"
LVDTN1= mean(N1_LVDT,2); %N1_LVDT(:,1);
LVDTN2= mean(N2_LVDT,2); %N2_LVDT(:,2);
LVDTN3= mean(N3_LVDT,2); %N3_LVDT(:,2);
LVDTN4= mean(N4_LVDT,2); %N4_LVDT(:,2);
LVDTN5= mean(N5_LVDT,2); %N5_LVDT(:,2);
LVDTN6= mean(N6_LVDT,2); %N6_LVDT(:,2);

%Smoothing LVDT data
smooth_N1_LVDT = smooth(LVDTN1,1000);
smooth_N2_LVDT = smooth(LVDTN2,1000);
smooth_N3_LVDT = smooth(LVDTN3,1000);
smooth_N4_LVDT = smooth(LVDTN4,1000);
smooth_N5_LVDT = smooth(LVDTN5,1000);
smooth_N6_LVDT = smooth(LVDTN6,1000);

%Ratio of size of Bionix file to size of LVDT file
a1 = size(N1_Bionix)/size(N1_LVDT);
a2 = size(N2_Bionix)/size(N2_LVDT);
a3 = size(N3_Bionix)/size(N3_LVDT);
a4 = size(N4_Bionix)/size(N4_LVDT);
a5 = size(N5_Bionix)/size(N5_LVDT);
a6 = size(N6_Bionix)/size(N6_LVDT);

%Pre-set space to save some time
N1_Load = zeros(size(smooth_N1_LVDT));
N2_Load = zeros(size(smooth_N2_LVDT));
N3_Load = zeros(size(smooth_N3_LVDT));
N4_Load = zeros(size(smooth_N4_LVDT));
N5_Load = zeros(size(smooth_N5_LVDT));
N6_Load = zeros(size(smooth_N6_LVDT));

%Manually interpolate data to align LVDT data with Bionix data
for i = 1:size(smooth_N1_LVDT)
    N1_Load(i,1) = N1_Bionix(floor((i-1)*a1+1),2);
end

for i = 1:size(smooth_N2_LVDT)
    N2_Load(i,1) = N2_Bionix(floor((i-1)*a2+1),2);
end

for i = 1:size(smooth_N3_LVDT)
    N3_Load(i,1) = N3_Bionix(floor((i-1)*a3+1),2);
end

for i = 1:size(smooth_N4_LVDT)
    N4_Load(i,1) = N4_Bionix(floor((i-1)*a4+1),2);
end

```

```

for i = 1:size(smooth_N5_LVDT)
    N5_Load(i,1) = N5_Bionix(floor((i-1)*a5+1),2);
end

for i = 1:size(smooth_N6_LVDT)
    N6_Load(i,1) = N6_Bionix(floor((i-1)*a6+1),2);
end

%Plot smoothed LVDT vs. fitted load
figure('name','Notched Load-Disp.')
plot(smooth_N1_LVDT,N1_Load,smooth_N2_LVDT,N2_Load,smooth_N3_LVDT
,N3_Load,smooth_N4_LVDT,N4_Load,smooth_N5_LVDT,N5_Load,smooth_N6_
LVDT,N6_Load)
legend('N1','N2','N3','N4','N5','N6')
grid on
title('1NEAT99')
xlim([0 0.1])
xlabel('Displacement (mm)')
ylim([0 90])
ylabel('Load (N)')



---


%% Unnotched Data Analysis - Load-Disp.

%Avg. LVDTs - assuming both LVDT1 & LVDT2 are usable, unless told
otherwise in "notes"
LVDTU1 = mean(U1_LVDT,2); %U1_LVDT(:,2);
LVDTU2 = mean(U2_LVDT,2); %U2_LVDT(:,1);
LVDTU3 = mean(U3_LVDT,2); %U3_LVDT(:,2);
LVDTU4 = mean(U4_LVDT,2); %U4_LVDT(:,1);
LVDTU5 = mean(U5_LVDT,2); %U5_LVDT(:,2);
LVDTU6 = mean(U6_LVDT,2); %U6_LVDT(:,2);

%Smoothing LVDT data
smooth_U1_LVDT = smooth(LVDTU1,5000);
smooth_U2_LVDT = smooth(LVDTU2,5000);
smooth_U3_LVDT = smooth(LVDTU3,5000);
smooth_U4_LVDT = smooth(LVDTU4,5000);
smooth_U5_LVDT = smooth(LVDTU5,5000);
smooth_U6_LVDT = smooth(LVDTU6,5000);

%Pre-set space to save some time
U1_Load = zeros(size(smooth_U1_LVDT));
U2_Load = zeros(size(smooth_U2_LVDT));
U3_Load = zeros(size(smooth_U3_LVDT));
U4_Load = zeros(size(smooth_U4_LVDT));
U5_Load = zeros(size(smooth_U5_LVDT));
U6_Load = zeros(size(smooth_U6_LVDT));

%Manually interpolate data to align LVDT data with Bionix data
for i = 1:size(smooth_U1_LVDT)

```

```

    U1_Load(i,1) = U1_Bionix(floor((i-1)*b1+1),2);
end

for i = 1:size(smooth_U2_LVDT)
    U2_Load(i,1) = U2_Bionix(floor((i-1)*b2+1),2);
end

for i = 1:size(smooth_U3_LVDT)
    U3_Load(i,1) = U3_Bionix(floor((i-1)*b3+1),2);
end

for i = 1:size(smooth_U4_LVDT)
    U4_Load(i,1) = U4_Bionix(floor((i-1)*b4+1),2);
end

for i = 1:size(smooth_U5_LVDT)
    U5_Load(i,1) = U5_Bionix(floor((i-1)*b5+1),2);
end

for i = 1:size(smooth_U6_LVDT)
    U6_Load(i,1) = U6_Bionix(floor((i-1)*b6+1),2);
end

%Plot smoothed LVDT vs. fitted load
figure('name','Unnotched Load-Disp.')
plot(smooth_U1_LVDT,U1_Load,smooth_U2_LVDT,U2_Load,smooth_U3_LVDT
,U3_Load,smooth_U4_LVDT,U4_Load,smooth_U5_LVDT,U5_Load,smooth_U6_
LVDT,U6_Load)
legend('U1','U2','U3','U4','U5','U6')
grid on
title('1NEAT99')
xlim([0 0.03])
xlabel('Displacement (mm)')
ylim([0 35])
ylabel('Load (N)')



---


%% Unnotched Data Analysis - E & MoR

nu = 0.26; %poisson's ratio for cement
s = 100; %mm, span

%Locating where 45% of peak load is
c1 = find(U1_Load >= UPeak(1,2)*0.45-0.1 & U1_Load <=
UPeak(1,2)*0.45+0.1);
c2 = find(U2_Load >= UPeak(2,2)*0.45-0.1 & U2_Load <=
UPeak(2,2)*0.45+0.1);
c3 = find(U3_Load >= UPeak(3,2)*0.45-0.1 & U3_Load <=
UPeak(3,2)*0.45+0.1);
c4 = find(U4_Load >= UPeak(4,2)*0.45-0.1 & U4_Load <=
UPeak(4,2)*0.45+0.1);

```

```

c5 = find(U5_Load >= UPeak(5,2)*0.45-0.1 & U5_Load <=
UPeak(5,2)*0.45+0.1);
c6 = find(U6_Load >= UPeak(6,2)*0.45-0.1 & U6_Load <=
UPeak(6,2)*0.45+0.1);

%Matrix of 45% of peak loads and the corresponding displacement
U45(1,2) = U1_Load(c1(1));
U45(2,2) = U2_Load(c2(1));
U45(3,2) = U3_Load(c3(1));
U45(4,2) = U4_Load(c4(1));
U45(5,2) = U5_Load(c5(1));
U45(6,2) = U6_Load(c6(1));

U45(1,1) = smooth_U1_LVDT(c1(1));
U45(2,1) = smooth_U2_LVDT(c2(1));
U45(3,1) = smooth_U3_LVDT(c3(1));
U45(4,1) = smooth_U4_LVDT(c4(1));
U45(5,1) = smooth_U5_LVDT(c5(1));
U45(6,1) = smooth_U6_LVDT(c6(1));

clear dlm
dlm = fitlm(U45(1,1),U45(1,2), 'Intercept', false);
U45(1,1) = U45(1,2)/table2array(dlm.Coefficients(1,1));

clear dlm
dlm = fitlm(U45(2,1),U45(2,2), 'Intercept', false);
U45(2,1) = U45(2,2)/table2array(dlm.Coefficients(1,1));

clear dlm
dlm = fitlm(U45(3,1),U45(3,2), 'Intercept', false);
U45(3,1) = U45(3,2)/table2array(dlm.Coefficients(1,1));

clear dlm
dlm = fitlm(U45(4,1),U45(4,2), 'Intercept', false);
U45(4,1) = U45(4,2)/table2array(dlm.Coefficients(1,1));

clear dlm
dlm = fitlm(U45(5,1),U45(5,2), 'Intercept', false);
U45(5,1) = U45(5,2)/table2array(dlm.Coefficients(1,1));

clear dlm
dlm = fitlm(U45(6,1),U45(6,2), 'Intercept', false);
U45(6,1) = U45(6,2)/table2array(dlm.Coefficients(1,1));

%Calculating E (GPa) and MoR (MPa)
for i=1:size(U45)
    E(i,1) =
    (U45(i,2)*s^3*(0.9745/48)/(U45(i,1)*25^4/12)+(6.5/7.5)*3*(1+nu)*U
45(i,2)*s/(4*25*25*U45(i,1)))/1000;
    MoR(i,1) = UPeak(i,2)*s/(4*25^3/6);
end

```

```
E_mean = mean(E); %GPa
E_std = std(E);
```

```
MoR_mean = mean(MoR); %MPa
MoR_std = std(MoR);
```

```
%% more Notched Data Analysis - E_n, G1C, K1C
```

```
%Locating 45% of peak load
```

```
d1 = find(N1_Load >= NPeak(1,2)*0.45-0.1 & N1_Load <=
NPeak(1,2)*0.45+0.1);
d2 = find(N2_Load >= NPeak(2,2)*0.45-0.1 & N2_Load <=
NPeak(2,2)*0.45+0.1);
d3 = find(N3_Load >= NPeak(3,2)*0.45-0.1 & N3_Load <=
NPeak(3,2)*0.45+0.1);
d4 = find(N4_Load >= NPeak(4,2)*0.45-0.1 & N4_Load <=
NPeak(4,2)*0.45+0.1);
d5 = find(N5_Load >= NPeak(5,2)*0.45-0.1 & N5_Load <=
NPeak(5,2)*0.45+0.1);
d6 = find(N6_Load >= NPeak(6,2)*0.45-0.1 & N6_Load <=
NPeak(6,2)*0.45+0.1);
```

```
%Matrix of 45% peak loads and the corresponding displacement
```

```
N45(1,2) = N1_Load(d1(1));
N45(2,2) = N2_Load(d2(1));
N45(3,2) = N3_Load(d3(1));
N45(4,2) = N4_Load(d4(1));
N45(5,2) = N5_Load(d5(1));
N45(6,2) = N6_Load(d6(1));
```

```
N45(1,1) = smooth_N1_LVDT(d1(1));
N45(2,1) = smooth_N2_LVDT(d2(1));
N45(3,1) = smooth_N3_LVDT(d3(1));
N45(4,1) = smooth_N4_LVDT(d4(1));
N45(5,1) = smooth_N5_LVDT(d5(1));
N45(6,1) = smooth_N6_LVDT(d6(1));
```

```
clear dlm
dlm = fitlm(N45(1,1),N45(1,2), 'Intercept', false);
N45(1,1) = N45(1,2)/table2array(dlm.Coefficients(1,1));
```

```
clear dlm
dlm = fitlm(N45(2,1),N45(2,2), 'Intercept', false);
N45(2,1) = N45(2,2)/table2array(dlm.Coefficients(1,1));
```

```
clear dlm
dlm = fitlm(N45(3,1),N45(3,2), 'Intercept', false);
N45(3,1) = N45(3,2)/table2array(dlm.Coefficients(1,1));
```

```
clear dlm
dlm = fitlm(N45(4,1),N45(4,2), 'Intercept', false);
```

```

N45(4,1) = N45(4,2)/table2array(dlm.Coefficients(1,1));

clear dlm
dlm = fitlm(N45(5,1),N45(5,2),'Intercept',false);
N45(5,1) = N45(5,2)/table2array(dlm.Coefficients(1,1));

clear dlm
dlm = fitlm(N45(6,1),N45(6,2),'Intercept',false);
N45(6,1) = N45(6,2)/table2array(dlm.Coefficients(1,1));

%Calculating other fracture properties
for i=1:size(N45)
    E_n(i,1) =
(N45(i,2)*s^3*(0.9745/48)/(N45(i,1)*25^4/12)+(6.5/7.5)*3*(1+nu)*N
45(i,2)*s/(4*25*25*N45(i,1))+(6.5/7.5)*4.5*N45(i,2)*s^2*(0.1864)/
(2*25*25*25*N45(i,1)))/1000;
    Fcon(i,1) = ((E_n(i,1)*1000)*25*25*NPeak(i,1)-
(NPeak(i,2)*s^3*(0.9745/4)/25^2)-
(3*NPeak(i,2)*(1+nu)*s*(6.5/7.5)/4))/((6.5/7.5)*4.5*NPeak(i,2)*s^
2*0.5/25);
    alphasol(1:10,i) = roots([98*pi/5, -3052*pi/75,
58801*pi/1250, -288691*pi/8750, 1217689*pi/60000, -
155861*pi/15625, + 460213*pi/100000, -1309*pi/1250,
314721*pi/500000,0,-Fcon(i,1)]);
    ac(i,1) = max(real(alphasol(5,i))*25,8);
    sigmac(i,1) = NPeak(i,2)*s/(4*25*(25-8)^2/6);
    K1C(i,1) = (1.122-1.4*(ac(i,1)/25)+7.33*(ac(i,1)/25)^2-
13.08*(ac(i,1)/25)^3+14*(ac(i,1)/25)^4)*sigmac(i,1)*sqrt(pi*ac(i,
1));
    G1C(i,1) = K1C(i,1)^2*(1-nu^2)/(E_mean); %N/m
end

```

```

%% more Notched Data Analysis - J1c

```

```

acave = (ac(1,1)+ac(2,1)+ac(3,1)+ac(4,1)+ac(5,1)+ac(6,1))/6;

```

```

%Calculate An

```

```

f1 = find(N1_Load(:,1)==NPeak(1,2));
f2 = find(N2_Load(:,1)==NPeak(2,2));
f3 = find(N3_Load(:,1)==NPeak(3,2));
f4 = find(N4_Load(:,1)==NPeak(4,2));
f5 = find(N5_Load(:,1)==NPeak(5,2));
f6 = find(N6_Load(:,1)==NPeak(6,2));
AN(1,1) = trapz(smooth_N1_LVDT(2:f1,1),N1_Load(2:f1,1));
AN(2,1) = trapz(smooth_N2_LVDT(2:f2,1),N2_Load(2:f2,1));
AN(3,1) = trapz(smooth_N3_LVDT(2:f3,1),N3_Load(2:f3,1));
AN(4,1) = trapz(smooth_N4_LVDT(2:f4,1),N4_Load(2:f4,1));
AN(5,1) = trapz(smooth_N5_LVDT(2:f5,1),N5_Load(2:f5,1));
AN(6,1) = trapz(smooth_N6_LVDT(2:f6,1),N6_Load(2:f6,1));

```

```

[m n] = size(AN);

```

```

[o p] = size(UPeak);

%Calculate all combinations of An and Aun to find JIc values
for i = 1:m
    j = find(U1_Load(:,1) >= NPeak(i,2) - 1 & U1_Load(:,1) <=
NPeak(i,2) + 1);
    AUN = trapz(U1_LVDT(2:j(1,1),1),U1_Load(2:j(1,1),1));
    k = (o*i)-(o-1);
    JIc(k,1) = 2*(AN(i,1)-AUN)/(25*(25-acave))*1000; %N/m

    j = find(U2_Load(:,1) >= NPeak(i,2) - 1 & U2_Load(:,1) <=
NPeak(i,2) + 1);
    AUN = trapz(U2_LVDT(2:j(1,1),1),U2_Load(2:j(1,1),1));
    k = k+1;
    JIc(k,1) = 2*(AN(i,1)-AUN)/(25*(25-acave))*1000; %N/m

    j = find(U3_Load(:,1) >= NPeak(i,2) - 1 & U3_Load(:,1) <=
NPeak(i,2) + 1);
    AUN = trapz(U3_LVDT(2:j(1,1),1),U3_Load(2:j(1,1),1));
    k = k+1;
    JIc(k,1) = 2*(AN(i,1)-AUN)/(25*(25-acave))*1000; %N/m

    j = find(U4_Load(:,1) >= NPeak(i,2) - 1 & U4_Load(:,1) <=
NPeak(i,2) + 1);
    AUN = trapz(U4_LVDT(2:j(1,1),1),U4_Load(2:j(1,1),1));
    k = k+1;
    JIc(k,1) = 2*(AN(i,1)-AUN)/(25*(25-acave))*1000; %N/m

    j = find(U5_Load(:,1) >= NPeak(i,2) - 1 & U5_Load(:,1) <=
NPeak(i,2) + 1);
    AUN = trapz(U5_LVDT(2:j(1,1),1),U5_Load(2:j(1,1),1));
    k = k+1;
    JIc(k,1) = 2*(AN(i,1)-AUN)/(25*(25-acave))*1000; %N/m

    j = find(U6_Load(:,1) >= NPeak(i,2) - 1 & U6_Load(:,1) <=
NPeak(i,2) + 1);
    AUN = trapz(U6_LVDT(2:j(1,1),1),U6_Load(2:j(1,1),1));
    k = k+1;
    JIc(k,1) = 2*(AN(i,1)-AUN)/(25*(25-acave))*1000; %N/m
end

JIcAv = mean(JIc);
JIcStd = std(JIc);

%Remove outliers
for i = 1:size(JIc)
    if JIc(i,1) > JIcAv+JIcStd
        JIc(i,1) = 0;
    elseif JIc(i,1) < JIcAv-JIcStd
        JIc(i,1) = 0;
    end
end
end

```

```
JIcAv_final = mean(nonzeros(JIc));  
JIcStd_final = std(nonzeros(JIc));
```

```
end
```


For unnotched specimen:

$$\Sigma M_s := 0 = W_s \cdot z_1 + W_d \cdot z_2 + W_1 \cdot (Q/2) - W_2 \cdot (S/4) + M - W_s \cdot z_3$$

$$z_{2_low} := \frac{\left(W_2 \cdot \frac{S}{4} - M_{lower} - W_s \cdot z_1 - W_1 \cdot \frac{Q}{2} + W_s \cdot z_3 \right)}{W_d} = 51.8 \text{ mm}$$

$$z_{2_low} = 51.8 \text{ mm}$$

lower bound for steel disc placement

$$z_{2_up} := \frac{\left(W_2 \cdot \frac{S}{4} - M_{upper} - W_s \cdot (z_1) - W_1 \cdot \frac{Q}{2} + W_s \cdot z_3 \right)}{W_d} = 78.2 \text{ mm}$$

$$z_{2_up} = 78.2 \text{ mm}$$

upper bound for steel disc placement

For notched specimen:

(accounting for weight of CMOD gage)

$$\Sigma M_s := 0 = W_s \cdot z_1 + W_d \cdot z_2 + W_1 \cdot (Q/2) - W_2 \cdot (S/4) + M - W_s \cdot z_3 - W_{cmod} \cdot z_{cmod}$$

$$z_{2_low} := \frac{\left(W_2 \cdot \frac{S}{4} - M_{lower} - W_s \cdot z_1 - W_1 \cdot \frac{Q}{2} + W_s \cdot z_3 + W_{CMOD} \cdot z_{CMOD} \right)}{W_d} = 75.4 \text{ mm}$$

$$z_{2_low} = 75.4 \text{ mm}$$

lower bound for steel disc placement

$$z_{2_up} := \frac{\left(W_2 \cdot \frac{S}{4} - M_{upper} - W_s \cdot (z_1) - W_1 \cdot \frac{Q}{2} + W_s \cdot z_3 + W_{CMOD} \cdot z_{CMOD} \right)}{W_d} = 101.8 \text{ mm}$$

$$z_{2_up} = 101.8 \text{ mm}$$

upper bound for steel disc placement

Appendix C: Cement Degradation Reference Information

Table C.1. Comparison of degradation methods.

Degradation Mode	Source	Type of Specimen	W/cm ratio	Curing Process	Degradation Method	Max. Exposure Time (days)	Quantification Technique
Calcium Leaching	[47]	Cement paste	0.60	91 days, calcium hydroxide solution	Ammonium nitrate	7	<ul style="list-style-type: none"> • Nanoindentation - micro-elastic modulus • Diffusivity • Porosity – SEM & MIP
	[51]	Cement paste	0.45, 0.50	28/75 days, saturated lime solution	Ammonium nitrate	3	<ul style="list-style-type: none"> • Strength, compression test • Porosity • Leached depth – optical microscopy
	[49]	Cement paste	0.50	56 days, sealed condition	Ammonium nitrate	6	<ul style="list-style-type: none"> • Porosity – MIP • Nanoindentation – Vickers hardness
	[67]	Cement paste	-	90 days in saturated calcium hydroxide solution	Deionized water	90	<ul style="list-style-type: none"> • Weight • Microstructure – optical microscopy, SEM & XRD • Leached depth – SEM & XRD
	[79]	Cement paste	0.40, 0.50	14 years	Distilled water	180	<ul style="list-style-type: none"> • Density – helium inflow test • Microstructure – TGA • Porosity – helium inflow test
	[68]	Cement paste	0.25	60 days, saturated lime solution	Deionized water	180	<ul style="list-style-type: none"> • Leached depth – SEM & TGA • Diffusivity – tritiated water
	[53]	Cement paste	0.45, 0.50	28/75 days, saturated lime solution	Ammonium nitrate	-	<ul style="list-style-type: none"> • Leached depth – XRD • Strength – compression test • Porosity
	[24]	Cement paste	0.40	28 days, 20°C, 100%RH	Deionized water & sodium sulfate	200	<ul style="list-style-type: none"> • Microstructure – XRD, SEM & EDS
	[48]	Cement paste & mortar	0.60	91 days, saturated lime solution	Ammonium nitrate	28	<ul style="list-style-type: none"> • Leached depth – fluorescence • Nanoindentation - Vickers hardness • Porosity - MIP • Microstructure – SEM

	[11]	Cement mortar	0.40	4 months, curing chamber	Ammonium nitrate	98	<ul style="list-style-type: none"> • Leached depth – fluorescence • Strength - 3-point bending flexural test
	[43]	Cement mortar	0.40, 0.50, 0.60	28 days, saturated lime solution	Ammonium nitrate	32	<ul style="list-style-type: none"> • Porosity – MIP • Microstructure – TGA, XRD • Ultrasonic measurements
	[54]	Cement mortar	0.41	28/56 days, 20°C, water	Electrochemical method	168	<ul style="list-style-type: none"> • Porosity – MIP • Strength – Compression • Microstructure – XRD, TGA
	[66]	Concrete	0.55, 0.75	50 days, humidity chamber	Seawater & distilled water	7	<ul style="list-style-type: none"> • Diffusivity
	[52]	Concrete	0.40, 0.50	28 days, saturated lime solution	Ammonium nitrate	365	<ul style="list-style-type: none"> • Leached depth – fluorescence • Porosity – MIP • Strength – compression test • Microstructure – atomic absorption spectroscopy • Diffusivity – Rapid Chloride Permeability Test
	[59]	Cement compound	0.50	180 days, saturated lime solution	Distilled water	90	<ul style="list-style-type: none"> • Length • Porosity, SEM • Microstructure – TGA & XRD
Sulfate Attack	[20]	Cement paste	0.40	90 days, saturated lime solution	Sodium sulfate	420	<ul style="list-style-type: none"> • Porosity – MIP • Leached depth – SEM • Tomography – CT scan • Length/expansion – strain
	[55]	Cement paste	0.40, 0.50, 0.60	7/28 days, humidity chamber	Sodium sulfate	60	<ul style="list-style-type: none"> • Leached depth (XRD)
	[50]	Cement mortar	0.53	60 days, humidity chamber	Sodium sulfate & magnesium sulfate	365	<ul style="list-style-type: none"> • Weight • Elastic modulus • Sulfate ion migration – ICP • Microstructure – SEM, XRD & X-CT

	[57]	Cement mortar	0.45, 0.60, 0.80	7 days, fresh water	Sodium sulfate & magnesium sulfate	365	<ul style="list-style-type: none"> • Length/expansion • Strength – compression test
	[87]	Cement mortar	0.48	1-250 days, 80-90°C, saturated lime solution	Sulfate in cement composition	-	<ul style="list-style-type: none"> • Expansion
	[19]	Concrete	0.33, 0.50	28 days, 20°C, 95%RH	Sodium sulfate & sodium chloride	54	<ul style="list-style-type: none"> • Expansion
Carbonation	[27]	Cement paste	0.38	28 days, brine solution at varying temp./pressure	CO ₂ solution	9	<ul style="list-style-type: none"> • Leached depth – SEM • Microstructure – SEM • Porosity – SEM • Nanoindentation – Vickers hardness • Microstructure – TGA & XRD
	[28]	Cement paste	0.38	28 days, high pressure brine	CO ₂ solution	365	<ul style="list-style-type: none"> • Leached depth – SEM • Microstructure – SEM & XRD
	[31]	Cement paste	0.44	28 days, high pressure/temperature	CO ₂ solution	60	<ul style="list-style-type: none"> • Leached depth – fluorescence • Strength – Brazilian tension test • Microstructure – optical microscopy, SEM & XRD
	[56]	Cement paste	0.38	365 days, brine solution at varying temp.	CO ₂ solution	31	<ul style="list-style-type: none"> • Leached depth – fluorescence & optical microscopy • Microstructure – XRD & SEM • Porosity • Permeability
	[32]	Cement paste	0.4	7 days, sealed condition	Ambient air & supercritical CO ₂	200 & 0.29	<ul style="list-style-type: none"> • Microstructure – XRD, TGA/DTA, pH • Porosity – MIP • Permeability
	[33]	Cement paste & mortar	0.50, 0.60	16 days, 20°C, 35%RH / 50%RH / 65%RH	Supercritical CO ₂	0.17	<ul style="list-style-type: none"> • Leached depth – fluorescence • Strength – compressive & flexural strength • Porosity – MIP

							<ul style="list-style-type: none"> • Microstructure – SEM & EDS
	[69]	Cement mortar	0.38	210 days, brine solution	CO ₂ solution	365	<ul style="list-style-type: none"> • Leached depth – fluorescence & optical microscopy
	[71]	Concrete	0.38, 0.46, 0.54	28 days, submerged in water	Air with 2% CO ₂ conc.	90	<ul style="list-style-type: none"> • Leached depth – fluorescence & FTIR
	[30]	CSH gel	-	30 days, sealed container	CO ₂ solution	0.25	<ul style="list-style-type: none"> • Microstructure – X-ray PDF
Chloride Penetration	[39]	Cement paste	0.33	90 days, humidity chamber	Chlorides/ deicing salts & Wet-dry	28	<ul style="list-style-type: none"> • Porosity – MIP • Microstructure – SEM & EDS
	[41]	Cement paste & concrete	0.40, 0.48	7 days, humidity chamber	Chlorides/ deicing salts & Freeze-thaw & wet-dry	60	<ul style="list-style-type: none"> • Weight • Scaling • Strength – compression test • Leached depth – ion penetration • Microstructure – XRD & SEM
	[42]	Cement paste, CH & cement mortar	0.42	Paste – 365 days in sealed condition Concrete – 28 days in sealed condition	Chlorides/ deicing salts & Freeze-thaw	7	<ul style="list-style-type: none"> • Cracks – acoustic emission • Leached depth – fluorescence • Microstructure – low temp. differential scanning calorimetry & isothermal micro-calorimetry
	[40]	Cement paste, CH & cement mortar	0.42	28 days in sealed condition	Chlorides/ deicing salts & Freeze-thaw	7	<ul style="list-style-type: none"> • Cracks – acoustic emission • Leached depth – fluorescence • Microstructure – low temp. differential scanning calorimetry & isothermal micro-calorimetry
	[38]	Cement paste & mortar, calcium silicate-based cement paste and mortar	0.42, 0.42, 0.24, 0.35	Ordinary cement – 28 days in sealed condition CS cement – 40 hrs. in CO ₂ -rich environment at 60°C	Chlorides/ deicing salts & Freeze-thaw	7	<ul style="list-style-type: none"> • Cracks – acoustic emission • Porosity – dynamic vapor sorption (DVS) • Microstructure – low temp. differential scanning calorimetry & isothermal micro-calorimetry